UNIVERSITY OF SOUTHAMPTON

Faculty of Engineering, Science and Mathematics
School of Engineering Sciences
Aerodynamics and Flight Mechanics Research Group

# Turbulent Wakes in Turbulent Streams

**by**

**Elad Rind**

Thesis for the degree of Doctor of Philosophy

January 2011

UNIVERSITY OF SOUTHAMPTON

# ABSTRACT

FACULTY OF ENGINEERING, SCIENCE AND MATHEMATICS
SCHOOL OF ENGINEERING SCIENCES
AERODYNAMICS AND FLIGHT MECHANICS RESEARCH GROUP

TURBULENT WAKES IN TURBULENT STREAMS

by Elad Rind

Direct numerical simulation and wind tunnel experiments have been used to study the effects of free-stream turbulence on axisymmetric wakes. In both cases the wake was introduced to various turbulent streams having various levels of turbulence intensity and length scales. It was found that the presence of the free-stream turbulence changes the wake's decay rate and does not allow self-similarity to occur (unless maybe very far downstream and way beyond the current measurements reached). Also, the free-stream turbulence was found to be causing a significant transformation in the turbulence structure inside the wake, where the latter was found to be gradually evolving towards the former. Last, the fact that the two approaches were modelling two different problems led to some differences in their results emphasising the importance of the flow structure around the wake generating body in shaping the far wake region.

# Dedication

*This work is dedicated to my late grandfather Yehoshua Rind who survived the horrors of the holocaust and was in his life and will always be a role model to me, and to the millions of Jews who died in the Holocaust; may God bless their souls.*

# Contents

**Abstract** i

**Dedication** iii

**List of Figures** ix

**List of Tables** xiii

**Declaration of Authorship** xv

**Acknowledgements** xvii

**Nomenclature** xix

**1 Introduction** 1

**2 Literature review** 3

2.1 Axisymmetric Far Wakes in Uniform Streams . . . . . 3

2.1.1 Theoretical Considerations . . . . . 3

2.1.2 Literature Review . . . . . 10

2.2 Homogeneous Isotropic Turbulence . . . . . 15

2.2.1 Theoretical Considerations . . . . . 15

2.2.2 Grid Turbulence . . . . . 19

2.2.3 Direct Numerical Simulation of Homogeneous Isotropic Turbulence . . 23

2.3 Axisymmetric Wakes in Turbulent Surroundings . . . . . 25

2.4 Boundary Layers in Turbulent Surroundings . . . . . 27

2.4.1 Expectations . . . . . 31

**3 Direct Numerical Simulation** **33**

3.1 Methodology . . . . . 33

3.1.1 The DNS Solver . . . . . 33

3.1.2 The Computational Domain . . . . . 35

3.1.3 Initial Conditions . . . . . 38

3.1.4 Combining The Wake and The Free-Stream Turbulence . . . . . 42

3.2 Results and Discussion . . . . . 43

3.2.1 The pure axisymmetric wake . . . . . 43

3.2.2 Free-stream Turbulence . . . . . 48

3.2.3 Wake Embedded in External Turbulence . . . . . 51

**4 Wind Tunnel Experiments** **59**

4.1 Methodology . . . . . 59

4.1.1 Measurement Techniques and Uncertainty . . . . . 60

4.2 Results and Discussion . . . . . 64

4.2.1 The Pure Axisymmetric Wake . . . . . 64

4.2.2 The Turbulent Streams . . . . . 70

4.2.3 Wakes in Turbulent Streams . . . . . 72

4.2.4 The Near-Wake Flow Field . . . . . 84

**5 Final Discussion** **89**

**6 Conclusions** **93**

6.1 Future Work Proposal . . . . . 93

**A Relationship Between the Mean Velocity and the Turbulent Shear Stress Profiles** **95**

**B Convection Term in Equation 4.9** **97**

**References** **99**

# List of Figures


3.1 (a) Example of comparison between a DNS one-dimensional energy spectrum, $E_{33}$, and its universal form in the inertial subrange, at $r/l_h = 0.25, 0.5$ and 0.75. (b) Results from the domain width test case. (c) Example of the (axial velocity) spatial correlation function, $R_z(l_h)$, at the wake's half width point; $Re \approx 4000$. . . . . 36

3.2 Illustration of the analogue between the specially developing wake (a) to the time developing one (b). . . . . 38

3.3 An illustration of the wake's initial mean flow field. . . . . 39

3.4 An illustration of the artificial combination of the wake with HIT. . . . . 42

3.5 An example of the non-dimensional vorticity magnitude contours, $\widetilde{\omega} = \omega l_h/U_d$, after the wake was artificially combined with the external turbulence. . . . . 43

3.6 (a) Variations of $Re$ and $Re_t$ with time (b) rms velocities at $r/l_h$. . . . . 44

3.7 (a) Variation of wake half-width and maximum deficit velocity with time. (b) the computed mean velocity profile compared with a cosinusoidal variation. . 45

3.8 Profiles of the various dimensionless turbulent stresses in the self-similar wake (a) Present DNS (b) Uberoi & Freymuth (1970). . . . . 46

3.9 (a) Profiles of the various dimensionless components of the TKE balance in the self-similar wake. (b) An example to the scatter noticed in the triple velocity product term. . . . . 48

3.10 (a) Taylor microscale Reynolds number vs. $t/T$. (b) Saffman and Batchelor's turbulence constrains. . . . . 49

3.11 (a) Variations of $A$ with time. (b) Decay of TKE ($k_e \sim t^{-n}$) in the external turbulence. . . . . 50

3.12 Axial velocity one-dimensional compensated energy spectrum of the (a) weak, (b) medium and (c) strong external turbulence cases at different times. . . . . 50

3.13 Decay of the deficit velocity (a) and the growth of wake half-width (b). . . . 52

3.14 Variations of $AU_d^{-1/2n}$ (a) and $U_d l_h^2$ (b). . . . . 52

3.15 (a) Illustration of dimensionless deficit velocity profile with time in the case where $u'_{ze_1}/U_{d_1} = 0.09$. (b) $u'_{z_{l_h}}/U_d$ vs. time. . . . . 53

3.16 Profiles of (a) $\overline{u_z^2}/U_d^2$, (b) $\overline{u_r^2}/U_d^2$, (c) $\overline{u_\theta^2}/U_d^2$ and (d) $\overline{u_z u_r}/U_d^2$ at different times in the case where $u'_{ze_1}/U_{d_1} = 0.17$. . . . . 54

3.17 Dimensionless Profiles of the TKE balance at different times for the case where $u'_{ze_1}/U_{d_1} = 0.17$. . . . . 55

3.18 (a) The change in $u'_{ze}/U_d$ vs. time for the different wake-background combinations. (b) Variation with time of the ratio of axial intensity at $l_h$ to free-stream intensity. . . . . 56

3.19 The Lumely triangle (black lines) on the plane of the invariants $\xi$ and $\eta$ of the Reynolds-stress anisotropy tensor; (a) The anisotropy invariant map. (b) Development of the turbulence at the wake half-width with time for the wake embedded in free-stream turbulence with initial $u'_{ze_1}/U_{d_1} = 0.36$. . . . . 58

4.1 Illustration of the experimental setup. . . . . 60

4.2 Example of comparison between the hot-wire one-dimensional energy spectrum, $E_{11}$, measured at about the wake half width and its universal form in the inertial subrange. . . . . 65

4.3 (a) Variations of the maximum rms velocities with $z/D$. (b) Variations of $Re$ and $Re_t$ with $z/D$. (c) Variation of wake half-width, maximum deficit velocity and $U_d l_h^2$ with time. . . . . 66

4.4 (a) Dependence of the normalised velocity deficit profiles, $(U_0 - U)/u'_{z_{max}}$, on z/D. (b) Profiles of the dimensionless turbulent velocity fluctuations in the self-similar wake . . . . . 67

4.5 (a) Comparison between the measured turbulent shear stress profile and the one extrapolated from the mean velocity profile. (b) The non-dimensional turbulent kinetic energy budget of the self similar wake. . . . . 68

4.6 Comparison between the various dimensionless Reynolds stress (a) and TKE balance (b) profiles of the self-similar wakes measured in the wind tunnel and in the DNS. . . . . 69

4.7 (a) Energy spectrum of each of the grid turbulence cases at $z/D = 0$. (b) Grid turbulence decay. . . . . 71

4.8 (a) Saffman and Batchelor's turbulence constrains. (b) Variations of $A$ with time.. . . . . 71

4.9 Profiles of the dimensionless normal turbulent velocity fluctuations across the wake for case one. . . . . 73

4.10 Profiles of the dimensionless normal turbulent velocity fluctuations across the wake for case three. . . . . 74

4.11 Profiles of the dimensionless normal turbulent velocity fluctuations across the wake for case five. . . . . 75

4.12 (a) The ratio between the various turbulence stresses at $z/D = 65$. (b), (c) and (d) are profiles of the dimensionless normal turbulent velocity fluctuations across the wake for cases one, three and five, respectively. . . . . 77

4.13 (a) and (b) Variations of $u'_{z_{max}}$ and $U_d$ with $z/D$, respectively. (c) and (d) Variations of $u'_{ze}$ with $z/D$ in grid A and B, respectively. (e) The defining parameters of the different turbulent streams at $z/D = 0$ and 85. . . . . 78

4.14 (a), (c) and (d) are examples of the scaling of the mean deficit velocity profile with $u'_{z_{max}}$ for cases one, three and five respectively and all compared to the pure wake case and (b) is an example of the scaling of the mean deficit velocity profile with $u'_{ze}$ for case one. . . . . 79

4.15 (a) Comparison of the deficit velocity profiles at $z/D = 65$ for the various cases. (b) Variations of the recirculation length with $u'_{ze}/U_0$. . . . . 80

4.16 (a) and (b) are examples of $E_{11}$ and $E_{33}$ vs. $f$, respectively, at $z/D = 65$ for the pure wake and cases one three and five. (c) and (d) are examples of the independency of dimensionless vortex shedding frequency in the Reynolds number for cases five and one, respectively. . . . . 81

4.17 (a) Variations of the dimensionless vortex shedding frequency with $u'_{ze}/U_0$ compared with the pure wake case, $St_0$. (b) Variations of the relative energy the shedding process contributes to the spectrum with $u'_{ze}/U_0$ compared with the pure wake case, $\Upsilon_0$. (c) is an example clarifying the definitions of $E_{with}$ and $E_{without}$. . . . . 82

4.18 Mean streamlines; (a) pure wake (b) case one. . . . . 85

4.19 (a) Growth of the vorticity thickness. (b) Reynolds stress profiles at $z/R_l = 1$. 86

4.20 Axial development of the maximum Reynolds stresses. . . . . 87

4.21 Development of the turbulence structure functions – $\overline{u_z u_v}/q^2$, (a), and $\overline{u_v u_v}/\overline{u_z u_z}$, (b). . . . . 88

# List of Tables

3.1 Defining parameters of the different free-stream turbulence flow fields at $t_1$. . 49

4.1 The defining parameters of the different turbulent streams at $z/D = 0$. . . . . 70

# Declaration of Authorship

I, Elad Rind, declare that the thesis entitled Turbulent Wakes in Turbulent Streams and the work presented in the thesis are both my own, and have been generated by me as the result of my own original research. I confirm that:

- this work was done wholly or mainly while in candidature for a research degree at this University;
- where any part of this thesis has previously been submitted for a degree or any other qualification at this University or any other institution, this has been clearly stated;
- where I have consulted the published work of others, this is always clearly attributed;
- where I have quoted from the work of others, the source is always given. With the exception of such quotations, this thesis is entirely my own work;
- I have acknowledged all main sources of help;
- where the thesis is based on work done by myself jointly with others, I have made clear exactly what was done by others and what I have contributed myself;
- parts of this work have been published as:
  - RIND, E. & CASTRO, I. P. Effects of free-stream turbulence on axisymmetric wakes, In preparation
  - RIND, E. & CASTRO, I. P. Direct numerical simulation of axisymmetric wakes in turbulent flows, In preparation
  - RIND, E. & CASTRO, I. P. 2009 The effect of freestream turbulence on far axisymmetric wakes. Proceedings of the Twelfth EUROMECH European Turbulence Conference, Marburg, Germany.

– RIND, E., REDFORD, J. A. & CASTRO, I. P. 2009 Far axisymmetric wakes in turbulence streams. Proceedings of the Sixth International Symposium on Turbulence and Shear Flow Phenomena, Seoul, Korea.

Signed: _____

Date: _____

# Acknowledgements

Doing a PhD is like climbing a mountain. First, you make sure you know what you are up against. Second, you plan how to reach the top. Last, you climb. From my own personal mountain climbing experience, the actual climbing part is the hardest, and not only because in that part there is only one thing (or more like one question) which keeps running in your head – why did I have to do that? But because no matter how well you planned, there would always be some "great" surprises. And every time you encounter one, the people surrounding you would be the ones to help you to get through.

In the past three years there had been so many moments where I needed help and so many people were there to help me. First, I would like to acknowledge my supervisor Professor Ian P. Castro who believed in me from the beginning and helped me to fulfil my desire to do a PhD. I would also like to thank him for sharing his amazing knowledge and experience with me and for his great help and guidance throughout the entire project.

Next, I would like to acknowledge Dr. John Redford and Dr. Roderick Johnstone for their great help with the flow solver code. In addition, I would like to thank Dr. Gary Coleman, leader of the UK's Turbulence Consortium, UKTC, for his great input to the project and for supporting my application for and providing me the computer time on the UK EPSRC HPCx IBM supercomputer (under EPSRC grant number EP/D044073/1). Also, I would like to acknowledge Dr. Victoria Suponitsky for many hours of discussions.

In addition, I would like to show great gratitude to Mr. Mike Street and all the technicians from the University of Southampton's Engineering Development and Manufacturing Centre, EDMC, for their great help with the design and manufacturing of the wind tunnel model and for helping me throughout the many crises I went through during my wind tunnel experiments.

Also, I would like thank some great people from the University of Surrey, UK, who helped me along the way. Dr. Paul Hayden for his great help with the Enflo software and Dr. Phil E. Hancock and Mr. Paul Nathan for repairing one of my hot-wires at a moment of crises. In addition, I would like to acknowledge the great help of Mr. Zachary Taylor from the University of Western Ontario, Canada, for advising me (over large number of emails) throughout the planning process of my PIV experiments.

Last, and definitely not least, I would like to thank my family and friends who stood beside me throughout the entire period and for helping me to stop thinking about that question and reach the top.

Elad Rind

University of Southampton, UK

September 2010

# Nomenclature

## Glossary

| | |
|---|---|
| DNS | Direct Numerical Simulation |
| EDMC | Engineering Development and Manufacturing Centre |
| FFT | Fast Fourier Transform |
| HIT | Homogeneous Isotropic Turbulence |
| LES | Large-Eddy Simulation |
| POD | Proper Orthogonal Decomposition |
| TKE | Turbulence Kinetic Energy |
| UKTC | UK Turbulence Consortium |

## Latin Letters

| | | |
|---|---|---|
| $A, B$ | Constants | $[-]$ |
| $A_s$ | Scaling tensor | $[m/s]$ |
| $b$ | Triple velocity correlation coefficient | $[-]$ |
| $b_i, b_j, b_k$ | Filter coefficient in the $x_i, x_j, x_k$ directions respectively | $[-]$ |
| $b_{ijk}$ | Three-dimensional filter coefficient | $[-]$ |
| $i, j, k$ | Counters | $[-]$ |
| $\tilde{b}$ | Self-similar form of the triple velocity correlation coefficient | $[-]$ |

| | | |
|---|---|---|
| $D$ | Diameter | $[m]$ |
| $d$ | Bar diameter | $[m]$ |
| $E$ | Spectrum | $[m^3/s^2]$ |
| $E_{33}$ | Spectrum in the axial direction | $[m^3/s^2]$ |
| $f$ | Function of the deficit velocity | $[-]$ |
| $fstp$ | Free-stream turbulence parameter | $[-]$ |
| $fstp_c$ | Castro's (1984) modified Free-stream turbulence parameter | $[-]$ |
| $g$ | Function of the Reynolds stress | $[-]$ |
| $h$ | Double velocity correlation coefficient | $[-]$ |
| $H_i$ | Includes the convective terms and the mean pressure gradient in the $x_i$ direction | $[m/s^2]$ |
| $\tilde{h}$ | Self-similar form of the double velocity correlation coefficient | $[-]$ |
| $K$ | Turbulent kinetic energy | $[m^2/s^2]$ |
| $k$ | Magnitude of the wave vector | $[-]$ |
| $k_j$ | Wavenumber component in the $x_j$ direction | $[m]$ |
| $L$ | Length scale in the axial direction | $[m]$ |
| $l$ | Length scale in the radial direction | $[m]$ |
| $L_1$ | Length scale | $[m]$ |
| $l_c$ | Experimental length scale | $[m]$ |
| $l_h$ | The wake half width | $[m]$ |
| $L_{ref}$ | Reference length | $[m]$ |
| $L_w$ | Domain width | $[m]$ |
| $L_z$ | Free-stream's integral length scale in the axial direction | $[m]$ |
| $M$ | Grid spacing | $[m]$ |
| $M_f$ | Momentum flux | $[N]$ |
| $N$ | Number of mesh points | $[-]$ |
| $n$ | Exponent constant | $[-]$ |
| $N_i, N_j, N_k$ | Number of mesh points in the $x_i, x_j, x_k$ directions respectively | $[-]$ |

| | | |
|---|---|---|
| $n_i, n_j, n_k$ | Number of mesh points which represent the length scale of the problem in $x_i, x_j, x_k$ directions respectively | $[-]$ |
| $P$ | Pressure | $[Pa]$ |
| $p$ | Fluctuating pressure | $[Pa]$ |
| $q$ | Turbulent velocity | $[m/s]$ |
| $r$ | Radial coordinate | $[m]$ |
| $r_1$ | Separation distance | $[m]$ |
| $\overline{R}$ | Three component random field | $[-]$ |
| $Re$ | Reynolds number | $[-]$ |
| $Re_l$ | Reynolds number based on the fluctuating velocity and radial length scales | $[-]$ |
| $Re_\lambda$ | Turbulent Reynolds number | $[-]$ |
| $Re_{\lambda_{fs}}$ | Turbulent Reynolds number in the free-stream | $[-]$ |
| $\hat{R}$ | Reynolds stress tensor | $[m^2/s^2]$ |
| $R_l$ | Recirculation length | $[-]$ |
| $Re_\theta$ | Momentum thickness Reynolds number | $[-]$ |
| $S$ | Spreading parameter | $[-]$ |
| $T$ | Energy transfer spectrum | $[m^3/s^2]$ |
| $t$ | Non-dimensional time | $[-]$ |
| $t_0$ | The non-dimensional time of false origin | $[-]$ |
| $t_1$ | The non-dimensional moment when the wake and the turbulent free-stream were combined | $[-]$ |
| $u'$ | rms of the fluctuating velocity in the axial direction | $[m]$ |
| $u'_{ze}$ | rms of the fluctuating velocity in the free-stream | $[m]$ |
| $u'_{z_{lh}}$ | rms of the fluctuating velocity in the wake half width | $[m/s]$ |
| $U_0$ | Mean free-stream Velocity | $[m/s]$ |
| $U_c$ | Experimental velocity scale | $[m/s]$ |
| $U_d$ | Mean centre deficit velocity | $[m/s]$ |
| $\hat{u}_i$ | Velocity in fourier space | $[m]$ |
| $u_i, u_j, u_k$ | Fluctuating velocity in tensor notation | $[m/s]$ |

| | | |
|---|---|---|
| $U_{ref}$ | Reference velocity | $[m/s]$ |
| $U_r, U_\theta, U_z$ | Mean velocity in the radial and axial coordinates respectively | $[m/s]$ |
| $u_r, u_\theta, u_z$ | Fluctuating velocity in the radial, angular and axial coordinates respectively | $[m/s]$ |
| $\tilde{u}$ | Velocity scale of turbulence | $[m/s]$ |
| $U, V, W$ | Mean velocity in cartesian coordinates | $[m/s]$ |
| $u, v, w$ | Fluctuating velocity in cartesian coordinates | $[m/s]$ |
| $\widehat{u}$ | Velocity Vector | $[m/s]$ |
| $u_{z_{cl}}$ | Axial fluctuating velocity in the wake's centreline | $[m/s]$ |
| $V_{HWA}$ | Voltage applied to the hot-wire | $[V]$ |
| $x_i, x_j, x_k$ | Cartesian coordinates in tensor notation | $[m]$ |
| $x, y, z$ | Cartesian coordinates | $[m]$ |
| $z$ | Axial coordinate | $[m]$ |
| $z_0$ | Axial location of the false origin | $[m]$ |

Greek Letters

| | | |
|---|---|---|
| $\beta$ | Decay Law Exponent Constant | $[-]$ |
| $\Gamma_{ref}$ | Hot-wire's effective angle | $[rad]$ |
| $\delta$ | Boundary layer thickness | $[m]$ |
| $\epsilon$ | Dissipation Rate | $[m^2/s^3]$ |
| $\Upsilon$ | The relative energy the shedding process contributes to the spectrum | $[-]$ |
| $\eta$ | Kolmogorov length scale | $[m]$ |
| $\theta$ | Angular Coordinate | $[rad]$ |
| $\theta$ | Momentum thickness | $[m]$ |
| $\kappa$ | Wave Number | $[1/m]$ |
| $\lambda$ | Taylor Microscale | $[m]$ |
| $\lambda_0$ | Taylor Microscale in the free-stream | $[m]$ |
| $\mu$ | Dynamic Viscosity | $[kg\, m^2/s]$ |
| $\nu$ | Kinematic Viscosity | $[m^2/s]$ |

| | | |
|---|---|---|
| $\xi$ | Non Dimensional Radial Coordinate | $[-]$ |
| $\rho$ | Density | $[kg/m^3]$ |
| $\varphi$ | Free-stream turbulence parameter correction function | $[-]$ |

Chapter 1

# Introduction

Axisymmetric turbulent wakes have been studied for over half a century, especially because in the far field (when the maximum wake deficit velocity is small in comparison to the free-stream velocity) they are one of the classical free shear flows for which the equations of motion suggest the possibility of self-similar behaviour. In practice many axisymmetric wakes develop in the presence of free-stream turbulence, which for long time has been known to affect the development of fully-turbulent shear layers. However, in almost all of the published work those wakes were studied in quiescent streams (as is later discussed in chapter 2), and so a thorough investigation of the effects of stream turbulence in needed.

The current work was partially motivated by the thought that if the free-stream turbulence decays at about the same rate as the wake (in the absence of free-stream turbulence), then the wake in the presence of free-stream turbulence may not initially be strongly effected by the latter. Given that in at least some wind tunnel realisations of Homogeneous Isotropic Turbulence (HIT), i.e. grid turbulence, $u'_{ze}/U_0$ (where $u'_{ze}$ is the rms of the axial velocity fluctuations of the free-stream and $U_0$ is the mean free-stream velocity) have been reported to decay like $z^{-p/2}$, where $z$ is the axial coordinate and $p \approx 1.3$, whereas the (high Reynolds number) axisymmetric wake's maximum velocity deficit $U_d/U_0$ (where $U_d$ is the maximum mean deficit velocity) decays like $z^{-2n} = z^{-0.67}$, the parameter $u'_{ze}/U_d$ may remain roughly constant. Likewise, with these decay power laws, it can be shown that the ratio of the free-stream turbulence integral scale to the wake half width $L_{ze}/l_h$ would also be approximately constant. Thus the lowest-order governing parameters for a wake immersed in free-stream turbulence might perhaps not change much along the wake, which might therefore initially have the same decay behaviour as in the absence of external turbulence. In addition to wind tunnel grid turbulence, Direct Numerical Simulations (DNS) of isotropic turbulence typically show decay rates similar to those found in wind tunnels, so one might anticipate analogous

behaviour for the time-dependent spatially homogeneous case.

In the current research two approaches were taken in order to investigate how the free-stream turbulence affects the development of the far axisymmetric wake. First, a time developing axisymmetric wake, without the generating body, was studied in quiescent and several turbulent streams using DNS. Second, the wake behind a disc in similar surroundings was studied experimentally in the University of Southampton's 3'x2' wind tunnel.

In the following chapters a discussion about some of the previous work (and background studies) that has been done is presented, followed by the results of the two approaches. The results reveal that the free-stream turbulence does change the wake's structure and decay rate and that the classical self-similarity behaviour ceases to exist.

Chapter 2

# Literature review

Before presenting and discussing the current observations it would be best to present first some background material. For simplicity, the summary will first start with axisymmetric far wakes in a quiescent free-stream followed by a discussion of homogeneous isotropic turbulence and grid turbulence and only afterwards a summary of the previous work that has been done about axisymmetric wakes in turbulent surroundings. As will be noted in section 2.3, very little work has been done on far axisymmetric wakes in turbulent surroundings; for that reason the effects of free-stream turbulence on boundary layers, which is a well studied problem, is also discussed, to obtain general understanding of the effects of free-stream turbulence on turbulent shear flows.

## 2.1 Axisymmetric Far Wakes in Uniform Streams

In order to better understand the mean flow field and the similarity behaviour of far axisymmetric wakes, a theoretical discussion is given first followed by a review of some relevant published work.

### 2.1.1 Theoretical Considerations

In this section a summary of the equations describing the development of shear flows for incompressible axisymmetric far wakes is presented. In addition, a complete similarity analysis is presented with a summary of all the assumptions that are made (the analysis follows the general description given by Tennekes & Lumley, 1972).

The following similarity analysis is based on the governing equations of the problem, the

Navier-Stokes equations - conservation of mass (2.1) and conservation of momentum (2.2):

$$\nabla \cdot \widehat{u} = 0, \tag{2.1}$$

$$\frac{\partial \widehat{u}}{\partial t} + \widehat{u} \cdot \nabla \widehat{u} = -\frac{1}{\rho}\nabla p + \nu \nabla^2 \widehat{u}, \tag{2.2}$$

where $\rho$ is the density, $\nu$ kinematic viscosity, $p$ is the pressure and $\widehat{u} = \widehat{u}\,(r, \theta, z, t)$ is the velocity field vector.

Since axisymmetric wakes are being studied it is convenient to use a cylindrical coordinate system $(r, \theta, z)$, where the wake develops in its axial direction, $z$.

Since there is no known general analytical solution to the Navier-Stokes equations some simplifications are made in order to reduce their complexity. The first simplification is that the mean flow is axisymmetric and there is no mean swirl. The second simplification is Townsend's (1976) thin shear layer approximation that the wake develops much slower in its axial direction than in its radial direction. I.e.

$$U_\theta = \frac{\partial\,()}{\partial \theta} = 0, \tag{2.3}$$

$$\frac{\partial\,()}{\partial z} \ll \frac{\partial\,()}{\partial r}. \tag{2.4}$$

**Scaling Analysis**

The Scaling analysis starts by examining the continuity equation, (2.1), in its axisymmetric Reynolds-averaged form. Under assumption (2.3) the continuity equation has the following form:

$$\frac{1}{r}\frac{\partial}{\partial r}(rU_r) + \frac{\partial}{\partial z}(U_z) = 0. \tag{2.5}$$

Next we define the deficit velocity, $U_d$, as the maximum value of $(U_0 - U_z)$, where $U_0$ is the uniform mean free-stream velocity and $U_z$ is the local axial mean velocity. Since $U_d \ll U_0$ in far wakes the axial velocity is scaled in the following way:

$$U_z = U_0 + (U_z - U_0) = O\,(U_0 - U_d) = O\,(U_0)\,, \tag{2.6}$$

where $O\,()$ represents the order of what is inside the brackets.

By taking $l_h$ to be the cross-stream length scale, which is defined as the wake half-width – the radial distance between the two points where $(U_0 - U_z) = 0.5U_d$, and by defining $L$ to be the length scale of appreciable change in the axial direction, the second gradient in equation (2.5) can be estimated using scaling analysis such that

$$\frac{\partial U_z}{\partial z} = O\left(\frac{U_d}{L}\right). \tag{2.7}$$

Now, using the simplified continuity equation (2.5) and (2.7), the radial mean velocity scales as:

$$O\left(\frac{l_h}{l_h^2}\right) \times O\left(U_r\right) = O\left(\frac{U_d}{L}\right) \quad \Rightarrow \quad U_r \sim O\left(\frac{l_h\, U_d}{L}\right). \tag{2.8}$$

Finally we define the velocity scale of turbulence, $\tilde{u}$, which is also being used to scale the Reynolds stress,

$$-\overline{u_i u_j} = O\left(\tilde{u}^2\right), \quad \overline{u_i^2} = O\left(\tilde{u}^2\right), \tag{2.9}$$

where the overbar represents the mean operator.

Next, we evaluate the momentum equation (2.2) in the radial direction which in its axisymmetric Reynolds averaged form and under assumption (2.3) has the following form:

$$\begin{aligned} U_r\frac{\partial U_r}{\partial r} + \frac{\overline{u_r^2}}{r} + \frac{\partial \overline{u_r^2}}{\partial r} + U_z\frac{\partial U_r}{\partial z} + \frac{\partial\left(\overline{u_r u_z}\right)}{\partial z} - \frac{\overline{u_\theta^2}}{r} = \\ -\frac{1}{\rho}\frac{\partial P}{\partial r} + \nu\left[\frac{1}{r}\frac{\partial}{\partial r}\left(r\frac{\partial U_r}{\partial r}\right) + \frac{\partial^2 U_r}{\partial z} - \frac{U_r}{r^2}\right], \end{aligned} \tag{2.10}$$

where $P$ is the mean pressure.

By expressing each term of equation (2.10) using the previously defined scales of motion

we identify their order of magnitude as demonstrated below:

$$
\begin{aligned}
U_r\frac{\partial U_r}{\partial r} &: \quad \frac{l_h\,U_d}{L}\times\frac{l_h\,U_d}{L\,l_h}=\left[\left(\frac{U_d}{\tilde{u}}\right)^2\left(\frac{l_h}{L}\right)^2\right]\times\frac{\tilde{u}^2}{l_h},\\
\frac{\overline{u_r^2}}{r} &: \quad 1\times\frac{\tilde{u}^2}{l_h},\\
\frac{\partial\overline{u_r^2}}{\partial r} &: \quad 1\times\frac{\tilde{u}^2}{l_h},\\
U_z\frac{\partial U_r}{\partial z} &: \quad U_0\frac{l_h\,U_d}{L^2}=\left[\left(\frac{U_d\,U_0}{\tilde{u}^2}\right)\left(\frac{l_h}{L}\right)^2\right]\times\frac{\tilde{u}^2}{l_h},\\
\frac{\partial\left(\overline{u_r u_z}\right)}{\partial z} &: \quad \frac{\tilde{u}^2}{L}=\frac{l_h}{L}\times\frac{\tilde{u}^2}{l_h},\\
\frac{\overline{u_\theta^2}}{r} &: \quad 1\times\frac{\tilde{u}^2}{l_h},\\
\frac{1}{\rho}\frac{\partial P}{\partial r} &: \quad ?,\\
\nu\left[\frac{1}{r}\frac{\partial}{\partial r}\left(r\frac{\partial U_r}{\partial r}\right)\right] &: \quad \frac{\nu\,U_d}{l_h\,L}=\left[\left(\frac{1}{Re_{l_h}}\right)\left(\frac{U_d}{\tilde{u}}\right)\left(\frac{l_h}{L}\right)\right]\times\frac{\tilde{u}^2}{l_h},\\
\nu\frac{\partial^2 U_r}{\partial z^2} &: \quad \frac{\nu\,l_h\,U_d}{L^3}=\left[\left(\frac{1}{Re_{l_h}}\right)\left(\frac{U_d}{\tilde{u}}\right)\left(\frac{l_h}{L}\right)^3\right]\times\frac{\tilde{u}^2}{l_h},\\
\nu\frac{U_r}{r^2} &: \quad \frac{\nu\,l_h\,U_d}{L\,l_h^2}=\left[\left(\frac{1}{Re_{l_h}}\right)\left(\frac{U_d}{\tilde{u}}\right)\left(\frac{l_h}{L}\right)\right]\times\frac{\tilde{u}^2}{l_h},
\end{aligned}
\tag{2.11}
$$

where $Re_{l_h}=\tilde{u}l_h/\nu$.

Since $(l_h/L)^2\to 0$ and does so faster than $\tilde{u}^2/(U_0\,U_d)\to 0$, assuming large enough $Re_{l_h}$, equation (2.10), based on the scaling analysis equation (2.11), is reduced to:

$$
\frac{\partial\overline{u_r^2}}{\partial r}+\frac{\overline{u_r^2}}{r}-\frac{\overline{u_\theta^2}}{r}=-\frac{1}{\rho}\frac{\partial P}{\partial r}. \tag{2.12}
$$

It should be stated that equation (2.12) is an approximation which is only valid in the limit $l_h/L\to 0$, such that

$$
\left[\left(\frac{U_d\,U_0}{\tilde{u}^2}\right)\left(\frac{l_h}{L}\right)^2\right]\to 0 \quad\text{and}\quad \left[\left(\frac{1}{Re_{l_h}}\right)\left(\frac{U_d}{\tilde{u}}\right)\left(\frac{l_h}{L}\right)\right]\to 0. \tag{2.13}
$$

Finally we evaluate the momentum equation (2.2) in the axial direction, which in its

axisymmetric Reynolds averaged form and under assumption (2.3), has the following form:

$$U_r\frac{\partial U_z}{\partial r}+\frac{\partial\overline{u_z^2}}{\partial z}+\frac{\partial\overline{u_r\,u_z}}{\partial r}+\frac{\overline{u_r\,u_z}}{r}+U_z\frac{\partial U_z}{\partial z}= \nu\left[\frac{\partial^2 U_z}{\partial z^2}+\frac{1}{r}\frac{\partial}{\partial r}\left(r\frac{\partial U_z}{\partial r}\right)\right]-\frac{1}{\rho}\frac{\partial P}{\partial z}. \tag{2.14}$$

Again, by expressing each term of equation (2.14) using the previously defined scales of motion we identify their order of magnitude as demonstrated below:

$$\begin{aligned}
U_r\frac{\partial U_z}{\partial r} &: \quad \frac{l_h\,U_d}{L}\frac{U_d}{l_h}=\left[\left(\frac{U_d}{\tilde{u}}\right)^2\left(\frac{l_h}{L}\right)\right]\times\frac{\tilde{u}^2}{l_h},\\
\frac{\partial\overline{u_z^2}}{\partial z} &: \quad \frac{\tilde{u}^2}{L}=\left[\frac{l_h}{L}\right]\times\frac{\tilde{u}^2}{L},\\
\frac{\partial\overline{u_r\,u_z}}{\partial r} &: \quad \frac{\tilde{u}^2}{l_h},\\
\frac{\overline{u_r\,u_z}}{r} &: \quad \frac{\tilde{u}^2}{l_h},\\
U_z\frac{\partial U_z}{\partial z} &: \quad \frac{U_d\,U_d}{L}=\left[\left(\frac{U_0\,U_d}{\tilde{u}^2}\right)\left(\frac{l_h}{L}\right)\right]\times\frac{\tilde{u}^2}{l_h},\\
\nu\frac{\partial^2 U_z}{\partial z^2} &: \quad \nu\frac{U_0}{L^2}=\left[\left(\frac{1}{Re_{l_h}}\right)\left(\frac{U_d}{\tilde{u}}\right)\left(\frac{l_h}{L}\right)^2\right]\times\frac{\tilde{u}^2}{l_h},\\
\nu\frac{1}{r}\frac{\partial}{\partial r}\left(r\frac{\partial U_z}{\partial r}\right) &: \quad \frac{\nu\,U_0}{l_h^2}=\left[\left(\frac{1}{Re_{l_h}}\right)\left(\frac{U_d}{\tilde{u}}\right)\right]\times\frac{\tilde{u}^2}{l_h},\\
\frac{1}{\rho}\frac{\partial P}{\partial z} &: \quad ?\ .
\end{aligned} \tag{2.15}$$

In order to estimate the order of magnitude of the pressure gradient, the simplified momentum equation in the radial direction (2.12) can be used, with

$$-\frac{1}{\rho}\frac{\partial P}{\partial z}=\frac{\partial}{\partial z}\left[\overline{u_r^2}+\int_0^r\left(\frac{\overline{u_r^2}}{r}-\frac{\overline{u_\theta^2}}{r}\right)\mathrm{d}r\right]. \tag{2.16}$$

Thus, the magnitude of the pressure gradient term is:

$$\frac{1}{\rho}\frac{\partial P}{\partial z}: \quad \frac{\tilde{u}^2}{L}=\left[\frac{l_h}{L}\right]\times\frac{\tilde{u}^2}{l_h}. \tag{2.17}$$

Assuming that $Re_{l_h}$ is large, the limit $l_h/L\to 0$ is valid and since $U_0\gg U_d$ the following

must be true:

$$\left(\frac{U_0\, U_d}{\tilde{u}^2}\right)\left(\frac{l_h}{L}\right) = O\left(1\right). \tag{2.18}$$

Using (2.18), the pressure gradient can be neglected compared to the other terms and finally equation (2.14) is simplified to

$$U_z\frac{\partial U_z}{\partial z} + \frac{\partial \overline{u_r\, u_z}}{\partial r} + \frac{\overline{u_r\, u_z}}{r} = 0. \tag{2.19}$$

(Note that the wake is assumed to be developing in the absence of any free-stream pressure gradient.)

Based on many observations, for wakes $U_z$ scales as $U_0$ and $\tilde{u}$ is of the same order as $U_d$ so the following may be written using (2.18)

$$\frac{U_0 - U_z}{U_0} = O\left(\frac{U_d}{U_0}\right) = O\left(\frac{l_h}{L}\right). \tag{2.20}$$

Since $l_h/L \to 0$, $U_d/U_0 \to 0$, which implies that the undifferentiated $U_z$ in equation (2.19) may be replaced by $U_0$. Thus, equation (2.19) may be approximated by:

$$U_0\frac{\partial U_z}{\partial z} + \frac{\partial \overline{u_r\, u_z}}{\partial r} + \frac{\overline{u_r\, u_z}}{r} = 0. \tag{2.21}$$

**Self-Preservation**

In the self-preservation analysis we assume that the evolution of the far axisymmetric wake is determined solely by the local scales of length and velocity. In general, it is expected that in far axisymmetric wakes mean velocity profiles behave as:

$$\frac{U_0 - U_z}{U_d} = f\left(\frac{r}{l_h}, \frac{l_h}{L}, Re_{l_h}, \frac{U_d}{U_0}\right). \tag{2.22}$$

Since previously it was assumed that $l_h/L \to 0$, $Re_{l_h} \to \infty$ and $U_d/U_0 \to 0$, equation (2.22) is reduced to

$$\frac{U_0 - U_z}{U_d} = f\left(\frac{r}{l_h}\right) \quad ; \quad l_h = l_h\left(z\right) \text{ and } U_d = U_d\left(z\right). \tag{2.23}$$

As mentioned above, in many published observations it was noticed that the scale of the turbulent intensity, $\tilde{u}$, is of the same order of magnitude as the scale of the deficit velocity, $U_d$. Knowing that, we could assume that the Reynolds stress may be described as:

$$-\overline{u_r\, u_z} = U_d^2 \times g\left(\frac{r}{l_h}\right) \tag{2.24}$$

(but see later).

Equations (2.23) and (2.24) are the basis of the self-preservation hypothesis: the velocity deficit and the Reynolds stress are invariant with respect to $z$ when they are expressed in terms of the local velocity and length scales. Substituting those terms into the momentum equation in the axial direction (2.21) and writing $\xi = r/l_h$, leads to

$$-\frac{U_0\, l_h}{U_d^2}\frac{\mathrm{d}U_d}{\mathrm{d}z}\, f + \frac{U_0}{U_d}\frac{\mathrm{d}l_h}{\mathrm{d}z}\,\xi\, f' = \frac{1}{\xi}\, g + g', \tag{2.25}$$

where a prime denotes differentiation with respect to $\xi$.

Since $f$ and $g$ are assumed to have universal shapes, such that the normalised profiles of the velocity deficit and the Reynolds stress are the same at all $z$, the coefficients of $f$ and $\xi\, f'$ in (2.25) must be constants, thus:

$$\frac{U_0\, l_h}{U_d^2}\frac{\mathrm{d}U_d}{\mathrm{d}z} = \text{constant}\ , \quad \frac{U_0}{U_d}\frac{\mathrm{d}l_h}{\mathrm{d}z} = \text{constant}. \tag{2.26}$$

Given that $U_0$ is constant, these imply that $l_h \sim z^n$ and $U_d \sim z^{n-1}$. Now, in order to evaluate the value of the power law constraint, $n$, the integral momentum flux in its axisymmetric form will be considered,

$$\rho \int_0^{2\pi} \int_0^{\infty} r\, U_0\, (U_0 - U_z)\, \mathrm{d}r\, \mathrm{d}\theta = M_f, \tag{2.27}$$

where $M_f$ is the momentum flux.

Using equation (2.23) the momentum flux (2.27) is now written as:

$$2\pi\rho\, l_h^2\, U_0\, U_d \int_0^{\infty} \xi f\, \mathrm{d}\xi = -M_f. \tag{2.28}$$

Since the momentum flux is independent of the location along the axial direction, $z$, the

product $U_d \times l_h^2$ must be also independent of the axial location. Using the solution of equation (2.26) the power law constraint therefore yields:

$$U_d \times l_h^2 \propto z^{n-1} \times z^{2n} \propto \text{constant} \quad \Rightarrow \quad (n-1) + 2n = 0 \quad \Rightarrow \quad n = \frac{1}{3}. \tag{2.29}$$

Thus, the wake's half width and its velocity deficit have the following self-similar form:

$$\begin{aligned} l_h &= A \times z^{\frac{1}{3}}, \\ U_d &= B \times z^{-\frac{2}{3}}. \end{aligned} \tag{2.30}$$

It should be noted that (2.30) implies that the wake's local Reynolds number (defined as $U_d l_h/\nu$) falls as $z^{-1/3}$. Thus, the viscous terms far enough downstream will eventually be significant. In that case, equation (2.21) would need to include the viscous term. Johansson, George & Gourlay (2003) who studied those two cases, generalised the above self-preservation study by not assuming that the shear stress scales like $U_d^2$ but as an unknown scale $S_{uv}$, as did Townsend (1976). Then, by using the constant momentum flux, the simplified momentum equation and assuming that $U_d \sim z^{-2n}$, $l_h \sim z^n$ and $S_{uv} \sim z^k$ it is only possible to show the relationship between all the power law constants. In order to define the actual values they showed that the individual Reynolds stress equations had to be investigated as well. These, together with the constraint of continuity on the pressure-rate-strain terms, were used to finally validate the classical result that for the infinite Reynolds number case the shear stress does indeed scale like $U_d^2$ with $n = 1/3$. On the other hand, for the finite Reynolds number case, where these viscous terms were included in the analysis, they showed that that assumption was not valid anymore. Thus, including the viscous terms yields $n = 1/2$ (which is similar to a laminar wake, Batchelor, 1967) but the shear stress in the finite Reynolds number case had in order for the Reynolds stress equations to be consistent with that result to follow $z^k$ with $k = -3/2$ and so does not scale with $U_d^2$. (Note that this solution is only true for the case where the production term in the turbulent shear stress transport equation is much smaller than all the other terms in that equation).

### 2.1.2 Literature Review

A large amount of work has been published about axisymmetric far wakes. Among the first was Carmody (1964), who measured mean velocity profiles downstream of a disc at a Reynolds

number of approximately $7 \times 10^4$, based on the free-stream velocity and the disc diameter. On the basis of the measured data the wake is axisymmetric and fully established, similarity profiles of the flow characteristics are formed within 15 diameters downstream of the disc and approximately 95% of the transfer of energy from the mean motion to the turbulence motion takes place within the first 3 diameters downstream of the disc in the region of the mean standing eddy. Later, far downstream measurements of an axisymmetric wake of a disc, up to 900 disc diameters downstream, were published by Hwang & Baldwin (1966). They reported on three discernible regions in the wake:

- $z/D < 50$: the formation region of the wake where the turbulence is highly anisotropic (the radial and angular turbulence intensities are 2.5 times as large as the axial turbulence intensity),
- $50 < z/D < 400$: where an approximate similarity region exists and "isotropic" turbulence relations are adequate for estimating decay,
- $z/D > 400$: the far downstream wake region which is highly intermittent and the turbulent kinetic energy decay rate is lower. This could be called the final period of decay.

Later on Gibson, Chen & Lin (1968) studied a turbulent wake of a sphere. Their measurements of temperature and velocity fluctuations in the wake led to the conclusion that the dissipation rates of turbulent kinetic energy and temperature variance both decrease approximately as $z^{-2.4}$ for the first 60 diameters downstream from the sphere. Recall that from self-similarity it is expected to follow $z^{-7/3}$ (since $\epsilon$, the dissipation rate, in the self-similar region scales like $U_d^3/l_h$). They also observed that small-scale velocity and temperature fluctuations are approximately homogeneous for the wake cross section. Their observations led them to the conclusion that the wake is divided into two sections along its radial axis - a continuous turbulence region in the centre and an intermittent one in the wake's borders. Chevray (1968) studied the wake behind a six-to-one spheroid. He reported that the wake is axisymmetric in shape and that the mean flow behind the spheroid is established at $3 < z/D < 6$, unlike Carmody's (1964) result ($z/D = 15$) for a disc, indicating a strong dependency on initial conditions in the near-wake region. Uberoi & Freymuth (1970) also studied the axisymmetric wake behind a sphere but at different low Reynolds numbers, $0.4 \times 10^4 < Re < 1.5 \times 10^4$, and at various downstream positions, $50 < z/D < 300$. In agreement with Hwang & Baldwin (1966) they also noticed that the wake becomes fully self-similar in the region $z/D > 50$

and that the turbulence is "isotropic" in that region as well. Later, Riddhagni, Bevilaqua & Lykoudis (1971) studied the wake of a sphere at much higher Reynolds number, $Re = 78000$, and in the region $z/D \leq 200$. They reported, in agreement with Chevray's (1968) results, that the mean velocity becomes self-similar at $z/D = 5$. Bevilaqua & Lykoudis (1978) also studied the wake of a sphere but in addition compared it to the wake of a porous disc sharing the same drag. They reported that self preservation in length and velocity scales was noticed $10D$ downstream of the sphere and $20D$ downstream of the disc. One of their most important conclusions was that self preservation is a process which develops gradually with downstream distance. First to 'self preserve' is the mean velocity profile, next are the Reynolds stresses and only later higher-order turbulence moments (based on downstream location), leading eventually to full self preservation of the wake. Even more importantly they also reported that the two wakes reached different states of similarity in velocity and Reynolds-stress profiles, which contradicts Townsend's hypothesis, Townsend (1970, 1976), that the structure of the turbulence in all self-preserving axisymmetric wakes is the same - that the turbulence forgets how it was created. Cannon (1991) continued Bevilaqua & Lykoudis' (1978) study by comparing the wakes behind a variety of axisymmetric bodies (disc, sphere and three porous discs with varying porosity) all sharing the same drag and Reynolds number of 3500, based on the free-stream velocity and the momentum thickness. Unlike Bevilaqua & Lykoudis (1978), Cannon (1991) could not reach any conclusion about the self-similarity of the wakes even though the wakes were mapped quite far downstream. In addition, by examining his results it is not clear if the turbulence intensities ever reach a self-similar state. Ostowari & Page (1989), who also noticed the self-similarity of the mean velocity in the near axisymmetric wake, proposed a cosine function as a representation of its profile and found it to be in good agreement with their and some other experimental results.

The initial evolution of a turbulent axisymmetric wake at Reynolds number 1500 was numerically simulated by Basu, Narasimha & Sinha (1992) using DNS. The simulation, which didn't resolve the generating body, showed a complete sequence of events from formation of vortex rings through generation of azimuthal instability and appearance of streamwise structures to eventual breakdown into turbulent flow, and revealed explicitly the features of the development of streamwise vorticity. Sadly in their simulation the wake did not reach a self-similar state, but they did notice that the simulation was approaching such a state, albeit slowly.

Later on, Birch (1996) reported that axisymmetric wakes appear to show no tendency to approach a unique self-similar state. Even very far downstream measurements of mixing rates and even the shapes of the mean velocity profiles showed a strong dependency on details of the wake's generating body (initial conditions), as was previously noticed by Bevilaqua & Lykoudis (1978). He didn't find any explanation as to why axisymmetric wakes are so sensitive to initial conditions in comparison to other free shear flows, but that result led to the conclusion that turbulence models in computational simulations cannot properly predict axisymmetric dependency on initial conditions.

With the advancement in computers DNS became more affordable. Gourlay, Arendt, Fritts & Werne (2001) reported DNS studies of an axisymmetric far wake at $Re = 10000$ - much higher than Basu *et al.* (1992), 1500. The simulation did not resolve a wake generator, like Basu *et al.* (1992), but was initiated using a super-position of an initially axisymmetric mean streamwise velocity profile and a spectrally specified fluctuation velocity field with initially incoherent phases to model the initial turbulence. Comparison of their results with laboratory flow experiments showed good agreement both with statistical quantities and vortex structures and evolutions. In addition, since their simulation ran for sufficient enough time, unlike Basu *et al.* (1992), they noticed the self-similarity of the wake in agreement with previously reported experimental data and with theory (see section 2.1.1).

Johansson, George & Woodward (2002) preformed a Proper Orthogonal Decomposition (POD) study of the axisymmetric wake behind a disc at a Reynolds number of 28000. Their measurements were done using multi-point hot wires (15 hot wires along the wake radius) located in the near downstream region, $10 < z/D < 50$, behind the disc. For all downstream positions in that region two distinct peaks were found in the first eigenspectrum: one at azimuthal mode 2 at near zero frequency and another at azimuthal mode 1 at a fixed Strouhal number of 0.126 which decreases more rapidly than the one at the near zero frequency leaving the latter to eventually dominate. They explained those results in the following way: at $z/D = 10$ the second mode is the dominant one and at $z/D = 50$ the first mode is the dominant one, with the first peak associated with a structure of frozen turbulence that is convected downstream, while the second peak was not observed to convect downstream. Later on, Johansson *et al.* (2003) studied axisymmetric far wakes using equilibrium similarity considerations, without the arbitrary assumptions of earlier theoretical studies – that the self-similar velocity and turbulence profiles are unique – using Gourlay *et al.*'s (2001) DNS results and previously published experimental data. Two similarity solutions were noticed

for the turbulent axisymmetric far wake: one for large local Reynolds number where the wake grows spatially as $z^{1/3}$ and another for small local Reynolds number where the wake grows as $z^{1/2}$. They confirmed Bevilaqua & Lykoudis' (1978) conclusion that both similarity solutions depend on the upstream conditions. Moreover, they showed that the effect of the initial conditions does not appear in the normalised velocity profiles, but in the growth rate and the higher velocity moments. Also, for both solutions the local Reynolds number of the flow diminishes with increasing time, and as a consequence even when the initial Reynolds number is large the flow evolves towards a low Reynolds number state, meaning that viscous effects continuously become more important, until eventually they may dominate. Note that in that case the shear stress decays slower than the mean wake (as $z^{-3/2}$ unlike $U_d^2 \sim z^{-2}$) which suggests that the turbulent shear stress will never be sufficiently small compared to the mean velocity scales to allow a genuine laminar wake to emerge. And so, if the wake starts as being fully turbulent it will remain so forever. Also, it should be mentioned here that the low Reynolds number similarity form has not been noticed in any wind tunnel experiment, but only in Gourlay *et al.*'s (2001) DNS results.

Later, Johansson & George (2006*a*,*b*) studied an axisymmetric far wake. Mean velocity profiles were found to be in excellent agreement with the high Reynolds number equilibrium similarity theoretical solution. In addition, the turbulence intensity, $u'/U_0$, reached a constant value far downstream; using POD they also found that the energetic structure of the axisymmetric wake could be described efficiently in terms of a few POD modes, with the first radial POD mode containing approximately 56% of the energy in the near wake, while farther downstream just before the self-similar region the second radial POD mode becomes the dominant one as the first one dies out quicker. More recently Tutkun, Johansson & George (2008) reported that first, second and third component POD of the far axisymmetric wake behind a disc give similar results in terms of the azimuthal modal distribution of the eigenvalues of Turbulence Kinetic Energy (TKE). The second azimuthal mode was found to be the dominant one, as was found by Johansson & George (2006*a*,*b*), when the streamwise fluctuations are included in the analysis. They concluded that the similarity between the eigenvalue distribution of the one, two and three component POD for the far axisymmetric wake is attributed to the production of turbulence in the wake, such that as long as the streamwise fluctuations are included in the analysis no significant differences are expected between the different approaches (due to the fact that there is only one production term in the TKE balance, which involves the normal stress term; Johansson *et al.*, 2003).

In summary, the axisymmetric wake develops during its first $50D$ to its self-similar state, where that development is progressive from the lower moments to the higher. In addition, while all wakes share the same decay rate, the self-similar profiles of the various velocity and length parameters are fully controlled by initial conditions.

## 2.2 Homogeneous Isotropic Turbulence

### 2.2.1 Theoretical Considerations

During the last century a number of analyses, based on various assumptions, have been developed to theoretically treat the decay of Homogeneous Isotropic Turbulence (HIT). In the following summary, a short review of some of the key studies is given.

The problem of energy decay of incompressible turbulent flow is governed by the Navier-Stokes equations, (2.1) and (2.2). Due to homogeneity, isotropy and incompressibility, the two-point second-order moment tensors of the velocity can be expressed in terms of a single scalar function, $h(r_1, t)$, representing the longitudinal velocity correlation coefficient, which is defined as

$$h(r_1, t) = \frac{\overline{u(x,t)\, u(x+r_1,t)}}{q(t)^2}, \tag{2.31}$$

where $r_1$ is the separation of the two points, $t$ is time, $u$ is the velocity fluctuation in the separation direction and $\frac{3}{2}q^2$ (where $q = \sqrt{\overline{u^2}}$) is the turbulence kinetic energy $K$.

In a similar way the triple-velocity correlation coefficient, $b(r_1, t)$, is defined as

$$b(r_1, t) = \frac{\overline{u(x,t)^2\, u(x+r_1,t)}}{q(t)^3}. \tag{2.32}$$

Karman & Howarth (1938) derived from (2.1) and (2.2) the following dynamical equation, which connects those two scalar quantities:

$$\frac{\partial\left(q^2 h\right)}{\partial t} = q^3\left(\frac{\partial b}{\partial r_1} + \frac{4}{r_1} b\right) + 2\nu q^2\left(\frac{\partial^2 h}{\partial r_1^2} + \frac{4}{r_1}\frac{\partial h}{\partial r_1}\right). \tag{2.33}$$

In addition, they showed that if any self-similar solution of the above equation exists, it

must be of the form:

$$\begin{aligned} h\left(r_1,t\right) &= \tilde{h}\left(r_1/\lambda\left(t\right)\right), \\ b\left(r_1,t\right) &= \tilde{b}\left(r_1/\lambda\left(t\right)\right), \end{aligned} \tag{2.34}$$

and they also gave two constraints:

$$\begin{aligned} q \times \lambda &= \text{constant}, \\ \lambda\frac{\partial\lambda}{\partial t} &= \text{constant}, \end{aligned} \tag{2.35}$$

where $\lambda$ is the Taylor microscale (i.e. Taylor, 1935). Note that those constrains arise from equation (2.33) by assuming large enough Reynolds number, i.e. neglecting the viscous term in that equation, and noting that the equation can only be satisfied if the coefficients, which are function of $t$ without being function of $r_1/\lambda\left(t\right)$, are proportional.

The power-law decay of the turbulence kinetic energy is then consequently obtained as

$$K = \frac{3}{2}q^2 \sim t^{-1}. \tag{2.36}$$

Although some early experiments, for example Batchelor & Townsend (1948*a*), seemed to be consistent with Karman & Howarth's (1938) power law decay, many later studies (see section 2.2.2) showed that the exponent is approximately in the range from 1.1 to 1.4.

Another way to examine the decay of HIT is by considering the relationship between the two-point velocity correlation to the energy spectrum, $E(\kappa)$, where $\kappa$ is the wavenumber. Assuming high enough turbulence Reynolds number and self-similarity of the large and the small scales, the following can be written,

$$E(\kappa) = \frac{1}{\pi}\int_0^\infty q(t)^2 h(r,t)\kappa r \sin(\kappa r)\mathrm{d}r. \tag{2.37}$$

Expanding equation (2.37) for small wavenumbers yields

$$E(\kappa \to 0) = \frac{L\kappa^2}{4\pi} + \frac{I\kappa^4}{24\pi^2} + \cdots \tag{2.38}$$

provided that $q(t)^2 h(r,t)$ decays sufficiently rapidly ($q(t)^2 h(r,t) \sim O(r^{-6})$ or smaller) for the

expansion to be valid, where $L$ and $I$ are the integrals

$$L = \int_0^\infty q(t)^2 h(r,t) \mathrm{d}r \tag{2.39}$$

and

$$I = -\int_0^\infty r^2 q(t)^2 h(r,t) \mathrm{d}r, \tag{2.40}$$

which are known as the Saffman and Loitsyansky integrals respectively.

This suggests that there are two important cases: when $L \neq 0$ we have $E(\kappa \to 0) \sim L\kappa^2$, which is called the Saffman (1967) spectrum (or turbulence), and when $L = 0$ we obtain $E(\kappa \to 0) \sim I\kappa^4$, which is known as the Batchelor (1953) spectrum (or turbulence).

Kolmogorov (1941c) predicted that isotropic turbulence should decay as $\overline{u^2} \sim t^{-10/7}$ using three assumptions: (i) the energy decays as $\mathrm{d}\overline{u^2}/\mathrm{d}t = -A\overline{u^3}/l$, where $l$ is the integral scale and $A$ is independent of time, (ii) the large scales (but not the whole spectrum) evolve in a self-similar manner when $r$ is normalised by the integral scale and (iii) Loitsyansky's integral is constant with time. Combining (ii) and (iii) gives $I \sim \overline{u^2} l^5 =$ constant which, when substituted into the energy equation (i), yields $K \sim t^{-10/7}$ and $l \sim t^{2/7}$.

While assumptions (i) and (ii) have been verified experimentally, the third has been heavily criticised. Especially since the Karman-Howarth equation integrates to give

$$\frac{\partial I}{\partial t} = 8\pi \left[ q^3 r^4 b(r,t) \right]_\infty , \tag{2.41}$$

where the subscript $\infty$ indicates $r \to \infty$, and it is expected that the long-range pressure forces will establish long-range triple correlations of the form $b(r,t)_\infty \sim cr^{-4}$, where $c$ is some pre-factor, which implies that $I$ is time dependent and casts doubt on the 10/7 decay law. Nevertheless, recent simulations by Ishida, Davidson & Kaneda (2006) have shown that $I$ could be constant in HIT depending on initial conditions.

On the other hand, Saffman (1967) showed that $L$ could be a non-zero constant in the case where the turbulence contains a sufficiently large amount of linear momentum, $P = \int_V u \mathrm{d}V$, where $V$ is some large control volume. In particular it is required that $\overline{P^2}$ grows with $V$ as $\overline{P^2} \sim V$, such that $L$ remains finite and non-zero as $V \to \infty$. (Note that if $\overline{P^2}$ grows slower than $V$ Batchelor turbulence is obtained). Thus, combining the conservation of $L$

with assumptions (i) and (ii) leads $K \sim t^{-6/5}$ and $l \sim t^{2/5}$

Some years later George (1992) proposed a new theory for the decay of HIT in which truly self-preserving solutions to the spectral energy equation were found to be valid at all scales of motion. Unlike Karman & Howarth (1938), who assumed self-similarity of correlation coefficients, George's method assumes self-similarity of the spectrum, $E(k,t)$, and the energy transfer spectrum, $T(k,t)$, in the following way:

$$\begin{aligned} E(k,t) &= E_s(t,*)\,\tilde{E}(\phi,*)\,, \\ T(k,t) &= T_s(t,*)\,\tilde{T}(\phi,*)\,, \end{aligned} \tag{2.42}$$

where $k$ is the magnitude of the wave vector, $\phi = kL_1$, $L_1 = L_1(t,*)$ and the argument $*$ was included to indicate a possible dependency on initial conditions.

By substituting these into the spectral energy equation for isotropic turbulence and enforcing consistency he found that

$$\begin{aligned} L_1 &= \lambda, \\ \frac{E(k,t)}{q^2\lambda} &= \tilde{E}(k\lambda)\,, \\ \frac{T(k,t)}{q^3} &= Re_\lambda^{-1}\tilde{T}(k\lambda)\,, \\ K &= \frac{3}{2}q^2 \sim t^n, \end{aligned} \tag{2.43}$$

where $n$ is a constant and $Re_\lambda = q\lambda/\nu$ is the Reynolds number based on the turbulence velocity, $q$, and the Taylor microscale, $\lambda$.

With the $Re_\lambda^{-1}$ modification any decay law exponent is now possible, which implies a dependency on initial conditions such that the decay rate constants cannot be universal, except possibly in the limit of an infinite Reynolds number. Another consequence of his theory is that the velocity-derivative skewness increases during decay at least until a limiting value is reached, after which possibly another self-similar state, which includes the proper decay of the nonlinear terms, is entered.

Later on, Huang & Leonard (1994) proposed a new self-similar solution to the Karman-

Howarth equation of the form:

$$\begin{aligned} h\left(r_1,t\right) &= h_1\left(r_1/\lambda\right) + Re_\lambda^{\beta} h_2\left(r_1/\lambda\right), \\ b\left(r_1,t\right) &= Re_\lambda^{\beta-1} b_2\left(r_1/\lambda\right). \end{aligned} \tag{2.44}$$

Their solution, unlike the previous one, can predict decreasing nonlinear interaction during the decay with $\beta > 1$, and thus might be applied to the final period of decay. They tested their solution using DNS at low $Re_\lambda$. Those DNS results were found to be consistent with their solution and the power-law decay was found to be about 1.5 for $10 < Re_\lambda < 20$ and 1.25 for $30 < Re_\lambda < 40$. Although their proposed similarity is valid for the final period of decay they have reported that such decay was not observed in their simulations.

### 2.2.2 Grid Turbulence

Grid turbulence has been the subject of much research in the last century. The reason is that the generated turbulence behind a grid is very close to HIT and therefore is often used for comparison with theoretical studies.

Early in the last century, Taylor (1935) examined different properties and flow characteristics of isotropic turbulence theoretically and compared his findings with previously reported measurements of grid and honeycomb turbulence. Among the examined properties are the average size of an eddy, the similarity rule of the turbulent velocity fluctuation decay, rate of energy dissipation and smallest size of an eddy. His theory predicts a linear similarity rule which varies with different grid configurations and honeycombs, characterised by $M$, $d/M$ and the shape of the bars / slats, where $M$ is the mesh spacing and $d$ is each bar's width. Also, using the correlation function the length scale of the average eddy was defined and found to be related to $M$. Due to the simplicity and usefulness in the understanding of the fundamental properties of turbulent flows his work was the foundation for all later studies of HIT.

As noted earlier, Karman & Howarth (1938) developed a general theory of isotropic turbulence. They proposed a solution for large Reynolds numbers which was applied to Taylor's (1935) problem of the decay of turbulence behind a grid. In addition, they confirmed his fundamental relation between the width of the correlation function and the size of the small eddies. They derived a general form for the fluctuating velocity, $\overline{u^2} = a_1\left(t - t_0\right)^{-n}$,

with a power law decay $n = 1$. Later, Kolmogorov (1941c) conducted a similar theoretical study, but even though he found the same form of power-law decay, his predicted value for the decay exponent was found to be different, $n = 10/7$.

Batchelor & Townsend (1948*a*,*b*) conducted an experimental validation of Karman & Howarth's (1938) theoretical study of isotropic turbulence using experimental measurements of turbulence behind different grids with $M/d = 5.33$. Their measurements of $\overline{u^2}$ and $\lambda$ indicate, as predicted by the theory, that they are both proportional to time (or distance from the grid) with a decay exponent similar to that found by Karman & Howarth (1938), $n = 1$, in the initial period of decay, and as a result the turbulence Reynolds number ($Re_\lambda = \sqrt{\overline{u^2}}\lambda/\nu$) is approximately constant. In addition, they noticed that the correlation functions maintain their form in the initial period of decay, implying self-preserving behaviour. In addition to the initial period of decay they studied the final period of isotropic turbulence decay, where the effects of inertia forces are negligible and the instantaneous velocity distribution may be solved as an initial value problem. Their measurements validated the existence of a final period of decay of isotropic turbulence for $z/M > 400$ at a mesh Reynolds number of 650 and the theoretical prediction of decay, $n = -5/2$, in that regime. Based on their findings, an empirical condition for the beginning of the final period is given as $R_\lambda \approx 5$. They concluded their study by stating that homogeneous turbulence tends to an asymptotic statistical state which is independent of initial conditions.

Batchelor & Stewart (1950), using a theoretical study, showed that the large-scale components of turbulence behind a grid in a uniform stream are anisotropic, even though the total turbulence energy may be distributed with approximate spherical symmetry. They confirmed their result using previously reported experimental data in the initial period of decay as well as in the final period of decay. Later on, Stewart & Townsend (1951) reported that grid turbulence is not isotropic in the very close region behind a grid ($z/M < 1$), and only later does it tend towards an isotropic state. In addition, they showed that at any mesh Reynolds number the self-preservation of the spectrum shape is valid for all but the smallest wave numbers and that the appropriate length scale is the Taylor dissipation length scale, $\lambda$. Afterwards, Grant & Nisbet (1957), who studied the turbulence intensity behind square mesh grids of bars, reported, as found by Batchelor & Stewart (1950), that the turbulence downstream of a grid is not only anisotropic but also inhomogeneous. They found that the anisotropy and inhomogeneity diminish very slowly with distance downstream from the grid. They could not give any physical reason for this but suggested that it has to do with the grid's geometry or

surface roughness. This was later confirmed by Corrsin (1963), who showed that the shape of the grid elements and its solidity ratio have a great effect on homogeneity, intensity level and the stability of the wake system generated by the grid.

Later, Uberoi (1963), who studied the energy transfer from large to small eddies in turbulence behind a square mesh, reported that the large eddies for which viscous dissipation is negligible satisfy a similarity relation which agrees with the fact that the total energy decays as some negative power of time. On the other hand, the small eddies which are in approximate spectral equilibrium satisfy a local similarity in agreement with Kolmogorov's (1941c) hypothesis.

With the ambition to generate isotropic turbulence behind grids, in which turbulence intensity ratio were equal in all directions, Comte-Bellot & Corrsin (1966) used a contraction downstream of the grid. This technique was chosen because contraction amplifies the transverse-velocity fluctuations - consistant with Taylor's (1935) observation that the turbulent motion is subjected to gross strain by passage through an area change and will undergo selective changes in its axial and transverse turbulent energy levels due to the directionally selective vortex-line distortions. They tested a few different grids and concluded that each grid needs its own specially designed contraction. Later, with the same idea in mind, generating more precise isotropic turbulence, Uberoi & Wallis (1967) measured the longitudinal and lateral turbulence intensities behind homogeneous grids of various geometries looking for the optimal geometry for that purpose. For all grids the ratio $\overline{u^2}/\overline{v^2}$ was found to be constant during the decay and was between 1.2 and 1.35 depending on the grid geometry. The turbulence intensity decay was found to follow a power law with the power exponent constant during the decay but it was found that it depended on the grid geometry and varied between 1.22 to 1.48, unlike in previously reported data (see above). That result led to their conclusion that the rate of decay depends on the initial energy spectrum and the large energy-containing eddies maintain a similarity form during the decay. Later on, Uberoi & Wallis (1969) reported, based on their measurements of spectra in different directions, that the energy-dissipating eddies are closer to isotropy and less dependent on the grid geometry, in contrast to the energy containing-eddies in grid generated turbulence. These findings are consistent with their previous finding (Uberoi & Wallis, 1967) that the deviation from isotropy of the energy-containing eddies and their spectra depend on the grid geometry.

Portfors & Keffer (1969) were the pioneers in the sense of correcting the measured turbu-

lent intensities by taking into account the wind tunnel's boundary-layer effects on the wake of a grid made out of parallel rods. Their measurements showed that the ratio $\overline{u^2}/\overline{v^2}$ converges downstream to the approximate value 1.1, which is lower than Uberoi & Wallis' (1967) measurements, while their corrected results showed that the turbulence becomes isotropic by a distance of approximately 30 mesh lengths downstream from the grid, indicating that the wind tunnel boundary layer has a strong effect on the grid's wake.

Bennett & Corrsin (1978) reported on more low Reynolds number grid-generated turbulence measurements. Their decay results agree with the predictions of the final period isotropic turbulence decay by the linear approximation of Karman & Howarth (1938) and Batchelor & Townsend (1948*b*). Also, in that region, they noticed that the previously nearly isotropic turbulence becomes less isotropic. In their investigation the effect of the wind tunnel walls was taken into account in the analysis of their measurements, as was done by Bennett & Corrsin (1978), and was noticed to affect the free-stream velocity fluctuation in addition to the centerline mean velocity. A decade later Maxey (1987) explained the anisotropy in the turbulence far downstream of a grid using the the slow decay of the turbulence kinetic energy in that region, which he found contributed to the skewness of the velocity fluctuations.

Mohamed & Larue (1990) studied the effect of initial conditions on the power-law decay of the variance of the turbulence velocity fluctuations downstream of bi-planar grids. In their investigation new measurements, in addition to previously published ones, were compared. They showed that the choice of the virtual origin and the use of data in the non-homogeneous portion of the flow can have a significant influence on the value of the parameters deduced for the power-law decay. They defined a specific criterion to identify the nearly homogeneous and isotropic portion of the flow for that purpose. Their results, based on that criteria, showed that the decay exponent and the virtual origin are 1.3 and 0 respectively, independently of the initial conditions (Reynolds number, mesh size, solidity, rod shape, rod surface roughness etc). On the other hand, they found that the decay coefficient (in other words the $\alpha$ in $u' = \alpha x^{-1.3}$, where $u'$ is the rms of the fluctuating velocity) is a function of the initial conditions due to the variation in the drag coefficient of the grids.

Recently Lavoie, Djenidi & Antonia (2007) reported that initial conditions set by the shape of the grid have a persistent impact on the large-scale organisation of the flow over the entire length of the wind tunnel, and that that effect does not disappear with downstream distance. In addition, they also noticed that the use of a contraction, which was previously

proposed by Comte-Bellot & Corrsin (1966), leads to more isotropy of the larger scales of motion. Later, in order to answer whether the large scales in grid turbulence should be classified as Batchelor (1953) or Saffman (1967) type, Krogstad & Davidson (2010) conducted high-resolution measurements of grid turbulence in a relatively large wind tunnel. The particularly large test section allowed them to measure energy decay exponents with high accuracy (recall the wind tunnel boundary-layer effect reported by Bennett & Corrsin, 1978). They found that the turbulence behind a grid is almost certainly of the Saffman type, with the integral scales satisfying $\overline{u^2}L^3 = \text{constant}$. Their measured energy decay exponent, however, was found to lie slightly below the theoretical prediction of $\overline{u^2} \sim t^n$, with $n = -1.2$. Rather they found the power law constant to be $n = -1.13$. They showed that that divergence arises from a weak temporal decay of the dimensionless energy dissipation coefficient, $\epsilon L/\overline{u^3}$, where $\epsilon$ is the dissipation rate, which is normally taken to be constant in strictly homogeneous turbulence, but in their grid turbulence experiments varied very slowly.

### 2.2.3 Direct Numerical Simulation of Homogeneous Isotropic Turbulence

In the past three decades the increase in computational resources have made DNS of HIT feasible. The real advantage behind such simulations is that all special and temporal scales are resolved and the physical understanding of even the smallest scales of motion is therefore possible.

Yeung & Brasseur (1991) used DNS of stationary HIT in order to explore the nature of the direct triadic couplings between the large and small scales in homogenous turbulence. The idea behind their study was the well-established concept in turbulence dynamics that in the high-Reynolds-number limit, the smallest, more dissipative, scales are structurally independent of the larger, more energetic, scales which ultimately determine the rate of viscous dissipation. They found that isotropically forced turbulence remains isotropic at all wave numbers and is most receptive to a forcing term with spectral content concentrated in the energy-containing range. In addition, they applied anisotropic forcing by adding vorticity at constant rate through an array of counter rotating rectilinear vortices which by a suitable choice of parameter produced a single spike in the radial forcing spectrum. The most striking consequence was the fact that the anisotropy was not only noticeable at the large scales but was also present at the small scales. They thought this might be evidence for a departure from the classical hypothesis of statistical independence between the large and small scales

and local isotropy *in the high Reynolds number limit*. Jimenez, Wray, Saffman & Rogallo (1993) have also studied stationary HIT. They reported that the intense vorticity region is organised in coherent, cylindrical or ribbon-like vortices (worm like). They showed that these vortices are natural features of the flow and that they are independent of the particular forcing scheme used. In addition, they reported that the vortices' Reynolds number, based on their circulation, increased monotonically with $Re_\lambda$ (raising the question - what happens at the limit of $Re_\lambda \to \infty$), while on the other hand their average rate of stretching increased only slowly with their peak vorticity, suggesting that self-stretching is not important in the evolution.

In many reported studies of stationary HIT there seem to be inconsistency between the simulated three-dimensional turbulence kinetic energy spectra and the experimentally determined Kolmogorov coefficient. That inconsistency tends to vary with choice of forcing scheme (even though the flow structure seems independent of the latter, Jimenez *et al.*, 1993). That inconsistency was later minimised by Sullivan, Mahalingam & Kerr (1994) who proposed that the forcing scheme should only maintain the energy at the low-wave-numbers (by "insertion", which is a relatively simple process), thereby taking advantage of the energy cascade in order to keep the flow stationary.

More recently, Keneda, Ishihara, Yokokawa, Itakura & Uno (2003) performed DNS of stationary HIT at $Re_\lambda = 167, 257, 471$ and 965. Their database suggest that the normalised mean energy dissipation rate per unit mass tends to a constant, independent of the fluid kinematic viscosity, $\nu$, as $\nu \to 0$. In addition, their results suggest that the energy spectrum in the inertial sub-range almost follows the Kolmogorov's $\kappa^{-5/3}$ scaling law, where $\kappa$ is the wave number, although the exponent is slightly steeper than $-5/3$ by about 6%.

While the great advantage of stationary flows is that they are homogeneous in time, understanding the decaying process of HIT is also needed. Huang & Leonard (1994) examined the decay rates of HIT. They found that the turbulent energy decays with a power law exponent approximately equal to 1.5 and 1.25, apparently depending on the turbulence Reynolds number, $Re_\lambda = u'\lambda/\nu$, which in their simulations was relatively low. More recently, Ishida *et al.* (2006) investigated the decay rate of HIT at higher Reynolds numbers. They found that the turbulence evolves to a state in which the Loitsyansky's integral $I$ (section 2.2.1) is approximately constant, and that Kolmogorov's classical decay law, $u^2 \sim t^{-10/7}$, holds true.

In summary, HIT has been studied for many years. Both DNS and wind tunnel ex-

periments have been proven to be effective for generating such flows. Nevertheless, while grid-generated turbulence seems to be Saffman-like, it is possible to use DNS and different initial conditions to create both Bachelor and Saffman turbulence fields. Consequently, the decay rate of HIT is not universal and it varies with initial conditions.

## 2.3 Axisymmetric Wakes in Turbulent Surroundings

Raithby & Echert (1968) were perhaps the first researchers to investigate the influence of free-stream turbulence on the wake of a sphere behind different grids. They were mainly interested in the influence of the turbulence intensity, the scale of turbulence, and the position of the support of the sphere, on the average heat transfer from spheres to an air stream. They reported that the average Nusselt number increases with the turbulence intensity and with the ratio of the sphere diameter to the scale of turbulence for values up to at least five. In addition, Nusselt numbers which were obtained using a cross-flow support were found to be about 10 per cent higher than those obtained using a rear support. Later on, Mujumdar & Douglas (1970) reviewed Raithby & Echert's (1968) results, particulary regarding the effect of the free-stream turbulence on the vortex shedding from the sphere. They noticed that when the free-stream was made turbulent by introducing turbulence-generating grids the auto-correlation for the sphere decayed without oscillation, thus indicating suppression of vortex shedding. They, in addition, conducted similar experiments for circular and square cylinders which led to the different result that the vortex shedding is not suppressed and that the Strouhal number stays the same even for highly turbulent free-streams.

Wu & Faeth (1994), more than two decades later, conducted measurements of sphere wakes in turbulent environments with an ambient turbulence intensity of 4% at low to moderate Reynolds numbers ($125 < Re < 1560$). Unlike Raithby & Echert (1968), who used grids to generate the surrounding turbulence, they used a turbulent pipe flow with the sphere mounted at the downstream end of the pipe. In comparison to non-turbulent environments they noticed a higher decay rate of the self-preserving region of the wake. While the wake was turbulent, its mean streamwise velocities scaled like a self-preserving laminar wakes (under uniform flow conditions the centerline velocity deficit in far laminar axisymmetric wakes is known to decrease as $z^{-1}$; Batchelor, 1967) but with enhanced eddy viscosity due to the turbulence. On the other hand in the light of the earlier discussion in section 2.1.1, the wake might have been similar to a finite Reynolds number turbulent wake. Later, Wu &

Feath (1995) widened the research and looked at the effect of different ambient turbulence intensities, from $2\% - 9.5\%$, on the sphere's wakes at similar Reynolds numbers. This time, each different ambient turbulence intensity was generated in a different way (which could have affected their results quantitatively, especially when different cases are compared). In addition to their previous findings, they noticed that the effective turbulent viscosities are relatively independent of position and ratios of ambient integral and Kolmogorov length scales to the sphere's diameter; however, they varied with both the Reynolds number and the ambient turbulene intensity in the low-Reynolds-number regime ($Re < 300$) and only with the Reynolds number in a higher regime ($Re > 600$). The transition regime between the two ($300 < Re < 600$) was found to be strongly affected by the vortex shedding from the sphere. Moreover, the laminar-like turbulent wake region (also previously reported by them; Wu & Faeth 1994) was followed by a final decay region, beginning when the wake's centre-line turbulence intensity was approximately equal to the ambient one. In that region faster decay rates were noticed but unfortunately no quantitative values were given.

Mittal (2000) used DNS to investigate the response of a sphere's wake to free-stream fluctuations. Since his research was directed towards particulate flows only low Reynolds numbers were simulated. He conducted several simulations with different amplitudes of free-stream fluctuations and different sphere Reynolds numbers ($100 < Re < 350$). He found that in the presence of free-stream fluctuations the wake behaves like an oscillator and returns a large amount of kinetic energy to the surrounding fluid at resonance. With the same idea in mind, Bagchi & Balachander (2004) also used DNS to investigate the wake of a particle. Unlike Mittal (2000) who used sinusoidally oscillated uniform flow for the inlet condition, they used a frozen isotropic turbulence field superimposed on a uniform flow. In their simulations the particle Reynolds number varied between 50 to 600 and the particle diameter varied between 1.5 to 10 times the Kolmogorov length scale. They found that the presence of the free-stream turbulence reduces the mean velocity profile and that the wake becomes flatter. In addition, they reported that the mean velocity profile in the particle wake with a turbulent free-stream behaves like a self-preserving laminar wake, as was previously reported by Wu & Faeth (1994; 1995). They also noticed that by increasing the free-stream turbulence intensity the process of vortex shedding is suppressed, as was previously reported by Mujumdar & Douglas (1970), and it only marginally increases the wake's oscillation.

Tyagi, Liu, Ting & Johnston (2005) measured the effect of free-stream turbulence generated by a perforated plate on the wake of a sphere at different Reynolds numbers. They

noticed that in the presence of the perforated plate a spectral peak could not be observed, indicating that the vortex shedding is attenuated by the free-stream turbulence, as was also noticed by Mujumdar & Douglas (1970) and Bagchi & Balachander (2004). Later, Tyagi, Liu, Ting & Johnston (2006) reported that the presence of free-stream turbulence reduces the size of the integral length scale, which was also reported by several authors in the context of free-stream turbulence on boundary layers (e.g. Section 2.4), as well as the intensity of the velocity fluctuations, which are associated with the destruction of horseshoe-like vortices in the wake by the free-stream turbulence.

More recently Legendre, Merle & Magnaudet (2006) used Large-Eddy Simulation (LES) to simulate a wake of a spherical bubble and of a solid sphere in a turbulent pipe flow. They reported that the centre-line velocity deficit decreased as $z^{-2}$ after a short regime where the centre-line velocity deficit decreased as $z^{-1}$; the latter is similar to what was reported by Wu & Faeth (1994; 1995). Moreover, they noticed that the $z^{-2}$ decay rate regime starts when the centre-line deficit velocity is of the same order as the free-stream rms velocity, unlike what was reported by Wu & Feath (1995) - the faster decay rate regime starts when the rms velocity fluctuations in the free-stream are of the same order as those on the wake's centre-line. Later, Redford & Coleman (2007) reported on a time-developing far axisymmetric wake in turbulent surroundings using DNS. In their simulation the generating body was not modelled and an initial wake was created using a series of ring vortices, which with time broke down and developed into a turbulent axisymmetric wake, which was later combined with the free-stream turbulence. They found that the stronger the background turbulence, the shorter was the time required for the wake to decay and merge with the surrounding turbulence.

Unfortunately, no additional work, as far as the author is aware of, is available for turbulent axisymmetric wakes in turbulent background flows. But before presenting and discussing the present results, a background summary of the effects free-stream turbulence have on boundary layers is given in the following section.

## 2.4 Boundary Layers in Turbulent Surroundings

Kline, Lisin & Waitman (1960) presented, in quite a lot of detail, experimental results of the effect of free-stream turbulence on a flat-plate boundary layer. They noticed that when the free-stream turbulence levels are equal to or greater than the ones in the self-generated

turbulence of the shear layer considerable alterations in the boundary layer characteristics occur. The high values of the free-stream turbulence intensity increase the boundary layer, momentum and displacement thicknesses, create more uniform velocity profiles and raise the value of the wall shear stress. In addition, the distributions of the intensity of the velocity fluctuations through the boundary layer are grossly altered and are no longer in line with the (nominally) universal profiles in both the inner and outer regions.

A decade later Charnay, Comte-Bellot & Mathieu (1971) also reported on the development of a turbulent boundary layer on a flat plate in the presence of a turbulent free-stream. They noticed similar physical phenomena as were reported by Kline *et al.* (1960) but added that the TKE production becomes larger in the boundary layer and that it is associated with the increase of the turbulence shear stress. Later, Huffman, Zimmerman & Bennett (1972) reported that the increase in the boundary-layer thickness with an increase in the turbulence intensity is due to the enhanced entrainment brought about by the highly excited state of the boundary between the shear layer and the free-stream. In addition, they noticed that the skin friction increases while the shape factor on the other hand decreases with an increase in the free-stream turbulence intensity. Tsuji & Iida (1972) reported that the turbulent background also increases the mixing length and the eddy viscosity. They proposed an analytical mean velocity distribution obtained by an eddy-viscosity hypothesis which shows good agreement when compared to experimental results. McDonald & Kreskovsky (1974) also gave a theoretical prediction of the effect of free-stream turbulence on a flat-plate boundary layer. By allowing for the entrainment of the free-stream turbulence into the boundary layer and performing a TKE balance, they were able to show satisfactory quantitative predictions in comparison to previously reported experimental data. Furthermore, their theoretical prediction indicated a 30% increase in heat transfer arising from a free-stream turbulence level of only 5% at high enough Reynolds numbers. But, due to lack of high Reynolds number experimental results, that prediction was not confirmed. Later Charnay, Mathieu & Comte-Bellot (1976) noticed that in the TKE balance the direction of the largest turbulent diffusion appears to coincide with that of the greatest principal stress. In addition, they noticed that the motion of the free edge of the boundary-layer is governed by structures of the overall flow with a characteristic length of the same order as of the boundary layer thickness.

Hancock (1980) was the first to really fully draw attention to the relationship between the free-stream's and the boundary layer's length scales. That relationship was found to have a large effect on the boundary-layer development, mostly when the ratio is of order one. He

also found that the turbulence background decreased the strength of Coles' wake component (Coles, 1956). Finally, using flow visualisation, he revealed that the free-stream turbulence causes the interface to be more irregular and to extend well beyond the edge of the mean velocity profile.

Pal (1981) reported on the effect of the wake behind a flat plate on another flat plate's boundary layer (which is a common issue in turbomachinery). He found that the total velocity defects in the axial, lateral and normal components of the mean velocity decrease towards the inner region of the boundary-layer. He also showed the existence of self-similarity, to some extent, of the axial mean velocity when normalised with respect to his proposed analytical turbulence interaction parameters. As for the turbulent quantities, he reported that they increase towards the inner region and decrease towards the outer edge of the boundary layer with increase in spacing between the two plates. Later on, Castro (1984) reported on the effect of free-stream turbulence on a turbulent boundary layer in zero pressure gradient. The momentum-thickness Reynolds number was less than 2000 and low Reynolds-number effects were thus expected to be significant. Nevertheless, it was found that those reduced as the level of the free-stream turbulence increased. Moreover, the range of length scales in the boundary layer were noticed to significantly decrease with decrease of the Reynolds number, thus the larger scales become increasingly emphasised. Finally, he proposed an empirical modification to Hancock's (1980) free-stream turbulence parameter, $fstp = (u'/U_0) \,/\, (\lambda_e/\delta + 2)$, where $\lambda_e$ is the external Taylor microscale and $\delta$ is the boundary layer thickness, at low Reynolds numbers, in the form of $fstp_c = 100\,(u'/U_0) \,/\, (0.5\lambda_e/\delta + 2.5)$.

Evans (1985) took Pal's (1981) turbomachinery work further by studying the effect of free-stream turbulence on a cascade compressor's blade. He found that even under adverse pressure gradient and turbulence free-stream, Coles' (1956) boundary-layer profile was valid. Later, Hancock & Bradshaw (1989) showed that free-stream turbulence increases the standard deviation of the interface between the boundary-layer and the free-stream turbulence as a proportion of the boundary-layer thickness, whilst the average position is mainly dependent upon the length-scale in the free-stream. The shear correlation coefficient of the boundary-layer fluid decreases, and the change in structure is directly related to the fluctuating strain rate. In addition, while the dissipation length-scale based on the turbulence shear stress was found to be little affected, the corresponding parameter based on the turbulence energy instead was noticed to be strongly affected.

Bandyopadhyay (1992) tested Hancock's (1980) free-stream turbulence parameter on low-Reynolds-numbers boundary layers under free-stream turbulence and proposed a modification to it (different to the one proposed by Castro, 1984). The modification is mainly associated with the parameter's Reynolds-number dependency at low Reynolds numbers and is in the form of $fstp_b = fstp \times \varphi$ for $fstp > 0.01$ and $fstp_b = fstp/\varphi$ for $fstp < 0.01$, where $\varphi = 1 + 3e^{-(Re_\theta/425)}$ is a correction function and $Re_\theta = U_0\theta/\nu$ is the momentum thickness Reynolds number. Later on Thole & Bogard (1996) confirmed another of Hancock's (1980) findings about the importance of the order of the integral length scale of the turbulent free-stream relative to the boundary-layer thickness, and in addition, they confirmed the validity of the log-law under such conditions. Finally, based on their observations, they concluded that the velocity defect in the outer region of the boundary layer is significantly decreased when the free-stream turbulence levels exceed those in the boundary layer.

Recently, Ustinov (2006) conducted DNS of a flat plate set suddenly in motion in turbulent surroundings. His data made it possible to estimate the effect of different factors such as the characteristics of the free-stream velocity fluctuation spectrum on laminar-turbulent transition in the boundary layers.

In summary, based on the many observations discussed above, an increase in the ratio $u'_{fs}/U_0$, where $u'_{fs}$ is the rms velocity fluctuations in the free-stream, affects the different boundary-layer properties in the following way:

- Boundary-layer thickness - increases
- Mean velocity profile - flattens
- Displacement thickness - increases
- Momentum thickness - increases
- Skin-friction coefficient - increases
- Shape factor - decreases
- Heat transfer - increases
- Production of turbulent kinetic energy - increases
- Reynolds shear stress - increases

- Mixing length - increases
- Eddy viscosity - increases

### 2.4.1 Expectations

Based on the studies presented above, the intensity levels (or the amount of energy) in the free-stream will most likely be the source of strongest influence on the wake. Note though that it is not expected that any particular level will be able to influence any axisymmetric wake in the same way since the turbulence levels inside different wakes or even for the same wake at different downstream positions might be different. Thus, the ratio between the intensity levels in the free-stream to the ones inside the wake or even the wake's centre deficit velocity will perhaps be a more likely control parameter for determining the free-stream turbulence impact on the far wake. In addition, since it was also noticed that the length scales in the free-stream play an important role in defining that influence, it is expected, in a similar way, that the ratio between the integral scale to the wake's half width will have an important role here as well.

In summary, since a boundary layer is one form of a shear layer it is expected that similar influences may be noticed for the axisymmetric wake. Note though that some differences are expected as well, mainly due to the presence of the wall in defining the flow structure close to it. Nevertheless, some of the similar influences where already reported by previous researchers presented in section 2.3. However two very interesting questions are still left open – at what rate the wake decays and whether it is in any sense self-similar in the presence of free-stream turbulence.

Chapter 3

# Direct Numerical Simulation

## 3.1 Methodology

### 3.1.1 The DNS Solver

The computational study in this research was done using the University of Southampton's in-house triply periodic pseudo-spectral DNS code (which was already used by Redford & Coleman, 2007; Redford, Castro & Coleman, in preparation) and is based on the method described by Kim, Moin & Moser (1987). The main advantage of using such a method to numerically solve the Navier-Stokes equations is in its accuracy. The flow field is transformed from real space into spectral space such that all the derivatives are calculated using their exact expressions. This means that the solution does not suffer from numerical dissipation, unlike other numerical methods. Yet, the method suffers from two major limitations: the boundary conditions can only be periodic and the code's current parallelization scheme reduces the maximum number of processors that may be used compared with the number of processors possible for the same grid arrangement but using a finite difference code.

#### The Mathematics Behind the Solver

Here a short mathematical description of the solver is given, based on the one given by Kim *et al.* (1987). The governing equations for an incompressible flow (Equations 2.1 and 2.2) can be written in the following non-dimensional cartesian form:

$$\begin{aligned} \frac{\partial u_i}{\partial t} &= -\frac{\partial p}{\partial x_i} + H_i + \frac{1}{Re}\nabla^2 u_i, \\ \frac{\partial u_i}{\partial x_i} &= 0, \end{aligned} \tag{3.1}$$

where $u_i$ is the velocity component in the $x_i$ direction, $H_i$ includes the convective terms and the mean pressure gradient in the $x_i$ direction and $Re$ denotes the Reynolds number defined as $Re = U_{ref}L_{ref}/\nu$, i.e. in terms of the reference velocity and length scales, $U_{ref}$ and $L_{ref}$ respectively.

Equation (3.1) is re-written as a fourth-order equation for $v$, and a second-order equation for the corresponding component of vorticity, $g$, as follows:

$$\frac{\partial}{\partial t}\nabla^2 v = h_v + \frac{1}{Re}\nabla^4 v, \tag{3.2}$$

$$\frac{\partial}{\partial t} g = h_g + \frac{1}{Re}\nabla^2 g, \tag{3.3}$$

$$f_1 + \frac{\partial v}{\partial y} = 0, \tag{3.4}$$

where the velocity components $(u, v, w)$ corresponds to the $(x, y, z)$ directions respectively, $f_1 = \partial u/\partial x + \partial w/\partial z$, $g = \partial u/\partial z - \partial w/\partial x$, $h_v = -\partial/\partial y\left(\partial H_1/\partial x + \partial H_3/\partial z\right) + \left(\partial^2/\partial x^2 + \partial^2/\partial z^2\right) H_2$ and $h_g = \partial H_1/\partial z - \partial H_3/\partial x$. The main advantage in this form is the fact that the pressure is no longer a variable so only three equations are left in the system.

The spatial derivatives are found using a Fast Fourier Transform (FFT) of the problem in each of the $(x, y, z)$ directions. Once the problem is transformed, the velocity derivatives are calculated using the following analytical, exact, relationship.

$$u_i\left(\widehat{x}\right) = \sum_{\widehat{\kappa}} \widetilde{u}_i\left(\widehat{\kappa}\right) e^{i\widehat{\kappa}\cdot\widehat{x}} \quad \Longrightarrow \quad \frac{\partial u_i}{\partial x_j} = \sum_{\widehat{\kappa}} i\kappa_j \widetilde{u}_i e^{i\widehat{\kappa}\cdot\widehat{x}} \tag{3.5}$$

where $\widetilde{u}_i$ is Fourier coefficient of the velocity component in the $x_i$ direction, $i = \sqrt{-1}$ and $\kappa_j$ is the wavenumber component in the $x_j$ direction.

From a computational point of view, evaluation of the non-linear term, $H_i$, is potentially extremely expensive. Considering a three-dimensional mesh (with $N^3$ mesh points), it would require of the order of $N^2$ operations in each direction to calculate the non-linear terms in spectral space, such that in total the order of $N^4$ would be required . The exorbitant cost of this fully spectral approach is clear, especially since a similar calculation for a finite-difference algorithm would require only $N^3$ operations in three dimensions. The solution to this problem, and the motivation for the pseudo-spectral method, is a combination of approaches. The linear terms are evaluated in Fourier space and the non-linear terms are evaluated in real space. To achieve this combined approach, velocity information is transformed from spec-

tral space to real space. Then the non-linear terms are evaluated, and finally, transformed back to spectral space, all of that using only only $N^3 \log_2 N$ operations in three-dimensions (Orszag, 1980). Evaluation of those non-linear terms can introduce errors known as aliasing errors, which come from the transformation between the spectral and the real spaces. These errors can be removed via the '3/2-rule', which involves using extra spatial resolution/modes for the projection from spectral to real space and back again, by interpolating the $N$ data points onto a grid of size $M \geq 3N/2 - 1$ in each direction, with the extra Fourier coefficients, between $|N/2|$ and $|M/2|$, set to zero (Canuto, Hussaini, Quarteroni & Zang, 1988).

Equations (3.2), (3.3) and (3.4) are integrated in time using a third-order Runge-Kutta method for the non-linear terms, $H_i$, as was successfully used by Spalart, Moser & Rogers (1991). The viscous terms are integrated in time using an integration factor, which was used by Rogallo (1981) in his DNS. That integration factor is the three-dimensional equivalent of the analytical methods used to solve the one-dimensional heat equation. That means that the solution in time is exact for the viscous terms (i.e. Kreyszig, 1988).

Data extraction for the post-processing was also done in the Fourier space. That way of calculating mean and fluctuating velocity components is more trivial and less computationally expensive. (For example, the first mode is the mean.) In addition, since the calculation of velocity derivatives is done using exact analytical expressions in Fourier space (as was demonstrated above) it is much more accurate.

### 3.1.2 The Computational Domain

The domain for the wake simulations (both with and without turbulent free-streams) was $4\pi l_{h_0} \times 4\pi l_{h_0} \times 16\pi l_{h_0}$, where $l_{h_0}$ is the wake's half width at $t = 0$, with $512 \times 512 \times 2048$ Fourier modes. Each time step typically took 50 seconds when using 512 processors of the UK's HPCx facility. Since up to 40000 time steps were required for the initial HIT simulations to achieve a stationary state (see section 3.2.2) a cheaper approach was required in order to reduce the computational cost. First the domain size was chosen to be $4\pi l_{h_0} \times 4\pi l_{h_0} \times 4\pi l_{h_0}$, i.e. only one quarter the axial length of the wake's domain. Moreover, for the first 95% of those initial simulations the domain had only $256 \times 256 \times 512$ Fourier modes (with each time step typically taking 5 seconds when using 256 processors) and for the final 5% it was increased to $512 \times 512 \times 512$ (with each time step typically requiring 21 seconds when using 256 processors). Note that further discussion about the method used to combine the wake

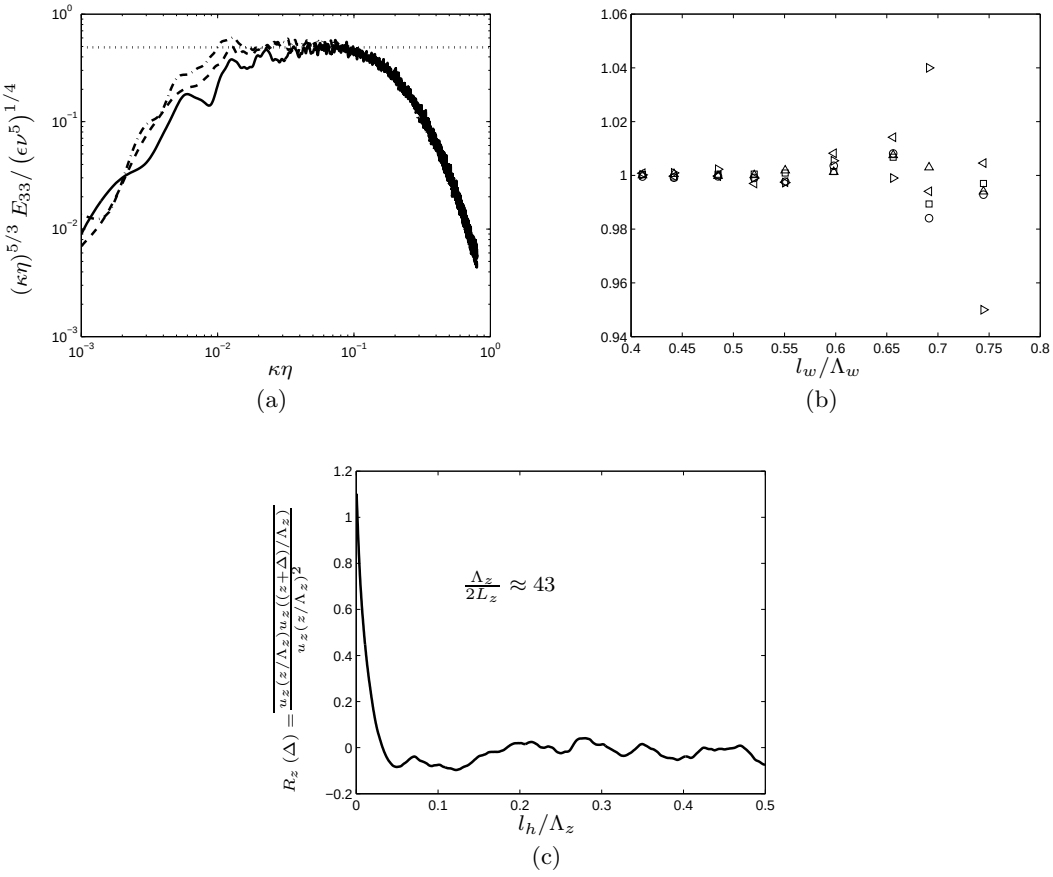


**Figure 3.1:** (a) Example of comparison between a DNS one-dimensional energy spectrum, $E_{11}$, and its universal form in the inertial subrange, dotted line. Solid, dashed and dashed-dot lines are self-similar profiles at $r/l_h = 0.25, 0.5$ and $0.75$, respectively. (b) Results from the domain width test case; ($\circ$), ($\square$), ($\triangle$), ($\triangleleft$) and ($\triangleright$) are the values of the centre deficit velocity, the turbulence axial, radial, angular and shear stresses (at the wake half width) of the wake in the small domain over those values in the wake in the larger domain, respectively.(c) Example of the (axial velocity) spatial correlation function, $R_z(l_h)$, at the wake's half width point; $Re \approx 4000$. $\Lambda_z$ is the axial length of the domain.

with the free-stream turbulence is given in section 3.1.4.

In all computations, local Kolmogorov length scales, $\eta = \left(\nu^3/\epsilon\right)^{1/4}$, where $\epsilon$ is the mean local TKE dissipation rate, varied between $20\% - 110\%$ of the computational grid resolution. As an example of the satisfactory nature of both resolution and statistical convergence in all the simulations, figure 3.1(a) shows an axial self-similar kinetic energy (compensated) spectrum in the pure wake averaged over times corresponding to $3000 < Re = U_d l_h/\nu < 4000$. The spectrum is compared with the universal result expected in the inertial subrange ($E_{33} = C\epsilon^{2/3}\kappa^{-5/3}$ where $\kappa$ is the wavenumber and $C$ is proportional to the the Kolmogorov constant and has the value of 27/55, e.g. Pope, 2000). The properties $E_{33}$ and $\epsilon$, where $E_{33}$ is the one-dimensional spectrum of the axial velocity, were directly calculated from the simulation data using the exact relationship, $\epsilon = 2\nu\overline{S_{ij}S_{ij}}$ where $S_{ij}$ is the usual fluctuating

strain rate tensor. The agreement is very satisfactory, and it may be noted that a significant inertial subrange is present, where the compensated spectrum is constant (although recall that Wang, Chen, Brasseur & Wyngaard (1996), among others, suggest that the Kolmogorov constant might be slightly larger than 27/55; small differences would not be apparent on such a plot).

As the wakes grow, there will eventually come a time when the cross-stream domain size, $\Lambda_w$, is too small. In order to evaluate what wake width would still be adequate, a test simulation was made. In that test simulation a wake (in quiescent surroundings) was initiated and allowed to develop until its diameter (measured at the point inside the wake where $U = 0.01U_d$) was about 40% of the domain width. At that point, the domain width was doubled by adding cells at its edges, where the velocity values entered to those added cells were copied from the ones at the edges of the original domain. Note that since periodic boundary conditions were used in the simulations, the "new" flow field was still satisfying the conservation equations. (Note as well that the wake width at that point was only 20% of the extended domain width.) Once the new domain was available, the wake in the original and larger domains were both allowed to continue developing and the values of mean velocities and Reynolds stresses were compared. It was found that up to about $l_w/\Lambda_w = 0.65$, where $l_w$ is the wake width and $\Lambda_w$ is the domain width, the differences between the two wakes were less than about 1.5% (for both the mean velocity and the Reynolds stress), as illustrated in figure 3.1(b). However, beyond that point those differences increased dramatically, as also illustrated in figure 3.1(b), where at $l_w/\Lambda_w \approx 0.68$ about 4% difference was noticed for the turbulence shear stress suggesting that the domain was no longer large enough to contain the wake without affecting it. And so, in the results presented here the wake was always smaller than that limit (i.e. $l_w/\Lambda_w \leq 0.65$). In addition, it was important to ensure a domain length sufficient to allow development of the largest axial structures. Figure 3.1(c) provides an example of the two-point spatial correlation function of the axial velocity component at the wake's half-width point ($r = l_h$), when the local Re was about 4000. It is clear that the domain is more than adequate in that respect; its half-length is some 43 times the axial integral scale, computed as the area under the spatial correlation up to the first zero-crossing point. It was chosen to be long in order to improve quality of statistics - recall the wake is axially homogeneous, so axial averaging could be employed to enhance statistical convergence.

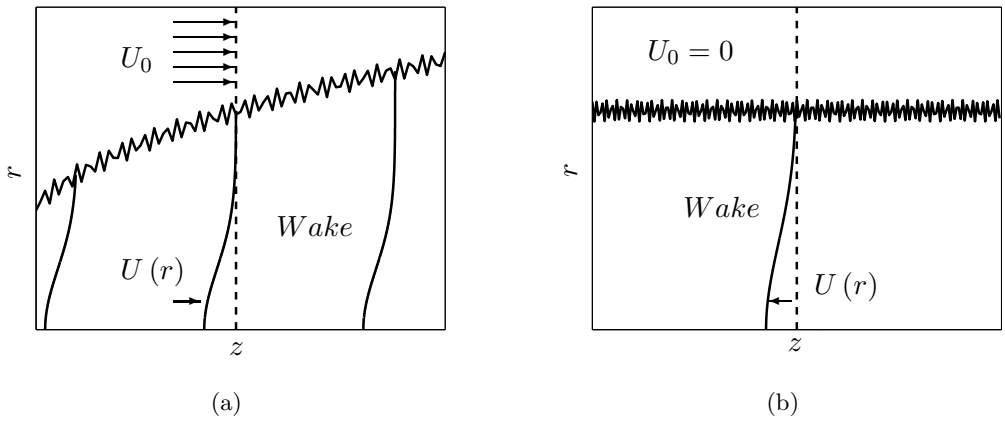


**Figure 3.2:** Illustration of the analogue between the specially developing wake (a) to the time developing one (b).

### 3.1.3 Initial Conditions

#### Far Axisymmetric Wake

Since this research concentrates on far axisymmetric wakes and resolving the flow around the generating body and the one in the far downstream regime using DNS would be very expensive, a different approach was taken.

As mentioned earlier, researchers in the past have used DNS with periodic boundary conditions to simulate time-developing (small-deficit) parallel wakes, as an analogue of the spatially developing wake. An exact Galilean transformation between the two cases is not possible so the two cases are not identical; not least, the transverse velocity implied by the periodic boundary conditions is zero, whereas in the spatial case it is the transverse gradient of this velocity which is zero. Also, formally, different integral constraints are satisfied in the two cases. But provided the deficit velocity in the spatial case is sufficiently small compared with the free-stream velocity, viewing the wake in a reference frame moving with that free-stream velocity provides a reasonable time-developing analogue. The mean radial velocity in a spatially developing wake is in fact very small and other authors have shown the similarity between time-developing (parallel) and spatially-developing wakes, so the present author believes that the fundamental differences between the two cases should not greatly influence the comparisons between them in a very significant manner. (For clarity an illustration of this analogue is given in figure 3.2.)

Gourlay *et al.* (2001) were the first to achieve, using DNS, a time developing far self-

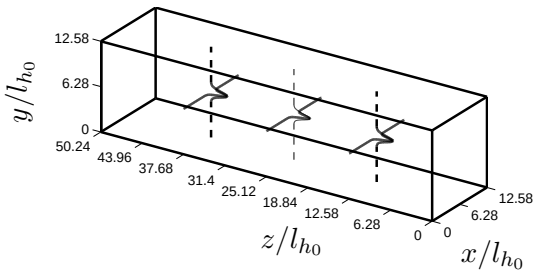


**Figure 3.3:** An illustration of the wake's initial mean flow field.

similar axisymmetric wake. Their initial condition field was based on previously reported experimental evidence. A cylindrical Gaussian mean streamwise velocity profile was imposed and, based on experimental evidence, scaled random numbers were added to it, simulating the velocity fluctuations. They mentioned that those initial conditions were known to be not physically correct so that the initial stage of the simulation is a so called correction stage which repairs the non-physicality in the flow field. Later, Redford & Coleman (2007) tried to reproduce their results using similar initial conditions but reported that the so-called correction stage was found to be very expensive and for that reason proposed a different approach using a series of ring vortices. A more thorough comparison between the two methods was later given by Redford *et al.* (in preparation), where no significant advantage in computational cost was noticed.

For that reason, it was decided to use a similar approach to the one used by Gourlay *et al.* (2001) but with some improvements in order to try to reduce the computational cost of the correction stage. The first change was to the chosen mean velocity profile. The profile used was extracted from Chevray's (1968) experimental prolate-spheroid data at $z/D = 1$, which was scaled such that the initial Reynolds number of the wake would be 10000. The second modification was to impose a digital filter on the generated random numbers in order to create a certain correlation between the fluctuations and, thereby introduce the desired length-scale information. The initial field is therefore more physically correct (but yet does not precisely satisfy the governing equations). The digital filter chosen is a modified version of the one developed by Xie & Castro (2008). The filter was modified, converted from a two-dimensional model to a three-dimensional one, to create appropriate structures in a three-dimensional initial turbulent flow field. For clarity, an illustration of the computational domain with the wake's mean profiles is presented in figure 3.3.

Even though the use of the filter was noticed to abbreviate the correction stage (for a test case it was found that the correction stage was 15% shorter using the digital filter), some disadvantages were still noticeable and are listed below.

1. For the correlation process a random number domain was used. It was found that generating a large number of normally distributed random numbers is computationally very expensive.

2. Once the random numbers were generated a large number of computational operations were still needed in order to deform the correlations (see below).

3. The digital filter, in total, was found to be very expensive computationally for the initialisation stage, but yet more efficient when the actual simulation time was taken into account (recall that 15% reduction in the duration of the correlation stage was noticed).

**Digital Filter Description**

Here a short description of the digital filter, including the current modifications, is given based on the detailed description of the filter given by Xie & Castro (2008).

First, a normally distributed three component random field, $\overline{R}$, is generated with standard deviation 1 and mean 0. Then, the one-dimensional filter's coefficients are calculated using the following relationship,

$$b_k = \frac{\tilde{b}_k}{\sqrt{\sum_{k=-N_k}^{N_k} e^{-\frac{\pi|k|}{n_k}}}}, \tag{3.6}$$

where $n_k$ is the number of grid points representing the length scale of the problem in the $\hat{k}$ direction (where in the current simulation it is defined equal in all three direction and is equal to the wake's half width), $N_k \geq 2n_k$ and $\tilde{b}_k = e^{-\frac{\pi|k|}{n_k}}$. Then the three-dimensional filter coefficients are calculated using the following relationship,

$$b_{ijk} = b_i \times b_j \times b_k, \tag{3.7}$$

where here the modification to the model takes place - the model is now three-dimensional,

unlike the original one reported by Xie & Castro (2008).

Once all the required information is generated the random field that was previously created, $\overline{R}$, is correlated using the three-dimensional filter, $b_{ijk}$, in the following way,

$$\bar{u}(x,y,z) = \sum_{k=-N_k}^{N_k} \sum_{j=-N_j}^{N_j} \sum_{i=-N_i}^{N_i} b_{ijk} \times \bar{R}\left(i+x, j+y, k+z\right). \tag{3.8}$$

When the random field is correlated, it requires appropriate scaling. This is done by multiplying it by the following transformation matrix,

$$A_s = \begin{pmatrix} \sqrt{\hat{R}_{11}} & 0 & 0 \\ \frac{\hat{R}_{21}}{A_{11}} & \sqrt{\hat{R}_{22} - (A_{21})^2} & 0 \\ \frac{\hat{R}_{31}}{A_{11}} & \frac{\hat{R}_{32} - A_{21}A_{31}}{A_{22}} & \sqrt{\hat{R}_{33} - (A_{31})^2 - (A_{32})^2} \end{pmatrix}, \tag{3.9}$$

where $\hat{R_{ij}}$ is the Reynolds stress tensor, which is a function of the location and in our case is based on Chevray's (1968) experimental data. Now that the field is correlated and scaled it is added to the mean velocity profile and the initial flow field is ready to run.

**Free-stream Turbulence**

In addition to the wake, three homogeneous isotropic turbulence (HIT) fields were generated separately. Recall that the major parameters affecting the wake's development in a turbulent field are expected to include $u'_{ze_1}/U_{d_1}$, the 'relative strength' of the external turbulence, and the length-scale ratio $L_{ze_1}/l_{h_1}$, where the subscripts $e$ and 1 denote the external turbulence and the time at which the wake was embedded within the external turbulence, respectively, and $u'_{ze_1}$ and $L_{ze_1}$ are the initial rms velocity fluctuations and integral length scale of the external turbulence, respectively. In order to achieve a specific strength a weaker field was first generated and prevented from decaying by using the forcing scheme of Sullivan *et al.* (1994) (which is described below). Then, knowing the initial value of $U_{d_1}$ from the preceding wake computation, the forcing constant (the turbulent kinetic energy) was increased gradually until the required $u'_{ze_1}/U_{d_1}$ was achieved. Note that the integral length scale is actually an output of the simulation and cannot be controlled *á priori*. Also note that the forcing was only used during the development process of the free-stream and was removed when the wake was embedded within the turbulent flow.

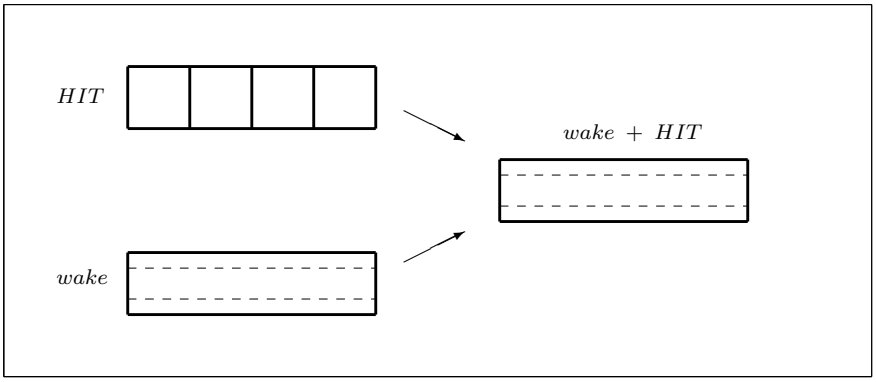


**Figure 3.4:** An illustration of the artificial combination of the wake with HIT.

**Forcing Scheme Description**

In order to generate the external turbulence Sullivan *et al.*'s (1994) forcing scheme was used. Its concept is to keep the turbulent flow field stationary by confining forcing to the lowest wavenumber shells $|\kappa| \leq \kappa_f$, where $\kappa_f$ is the maximum wavenumber subjected to forcing. Thus, the forcing scheme maintains the kinetic energy in a wavenumber band $\kappa \leq \kappa_f$ constant. This is accomplished by multiplying all the Fourier coefficients of all three velocity components for $\kappa \leq \kappa_f$ by a real number that may be readily evaluated by using the current value of $E(\kappa \leq \kappa_f)$, where $E$ is the energy spectra of the velocity, at time $t$ and its estimated value at $t + \Delta t$ (which is available at the end of the first Runga-Kutta step, section 3.1.1). Note that the physical picture that emerges is that energy is put back at the large scales of motion (in order to keep them stationary), without destroying either the homogeneity or isotropy of the flow field at both the large and small scales.

### 3.1.4 Combining The Wake and The Free-Stream Turbulence

Before presenting the basic data for both the self-similar wake (without stream turbulence) and the HIT fields, a description is first given of how the former was artificially combined with each of the latter. Each combination was implemented at a time when the pure wake had achieved its self-similar state. Two constraints were used: the free-stream turbulence was inserted into the domain at all locations outside the mean wake (defined by the region in which the velocity was below 1% of the centre-line value) and at all places inside the mean wake where the turbulence kinetic energy (TKE) was smaller than 5% of the maximum TKE

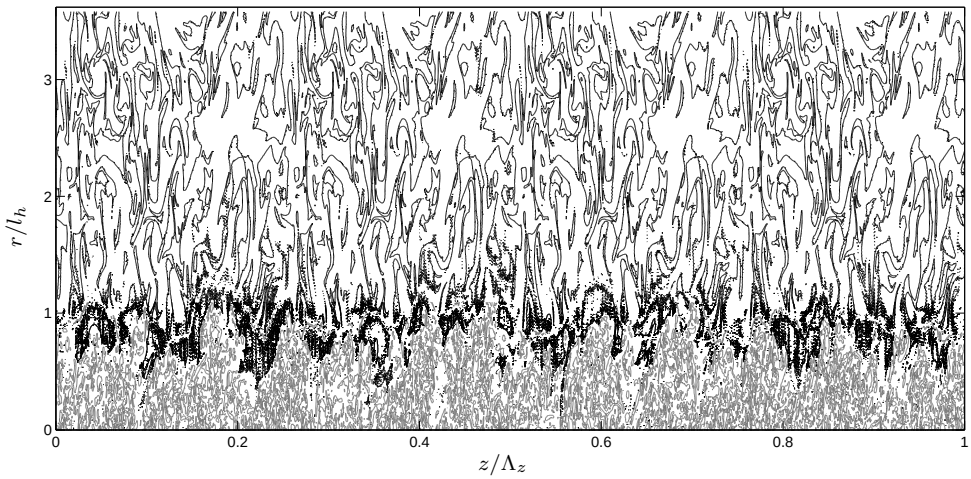


**Figure 3.5:** An example of the non-dimensional vorticity magnitude contours, $\widetilde{\omega} = \omega l_h/U_d$, after the wake was artificially combined with the external turbulence; grey: $\widetilde{\omega} = 12.8$ (the wake region) and black: $\widetilde{\omega} = 0.6$ (the free-stream turbulence region).

inside the wake. Since the external turbulence flow fields were one quarter the length of the wake's domain, and axially periodic, four identical turbulence fields were stacked axially, as illustrated in figure 3.4. The whole flow field (wake plus external turbulence, illustrated in figure 3.5) was then allowed to develop and decay with time and its features were analysed. Because the initial combined flow field did not satisfy the conservation equations, a relatively short correction stage took place, as discussed in section 3.2.3.

## 3.2 Results and Discussion

### 3.2.1 The pure axisymmetric wake

Johansson *et al.* (2003) suggested that the high Reynolds number similarity solution would not be expected to appear if the local Reynolds number ($Re = U_d l_h/\nu$) is below about 500. It will also require a clear inertial subrange in the energy spectrum. Figure 3.1(a) shows that the latter does occur in the present computations and figure 3.6(a) shows the variation of $Re$ with time $t$. Here $t$ has been non-dimensionalised using the initial values of wake half-width $l_{h_0}$ and maximum velocity deficit $U_{d_0}$. Each variable was obtained at every time step by circumferential and axial averaging. After an initial development period (prior to $t = 50$, where the numerical correction followed by the development and creation of genuine turbulence structure takes place) $Re$ remains above 2000 for the entire computation. Likewise, the turbulence Reynolds number, defined by $Re_t = k^2/\epsilon\nu$, where $k$ is the turbulent kinetic

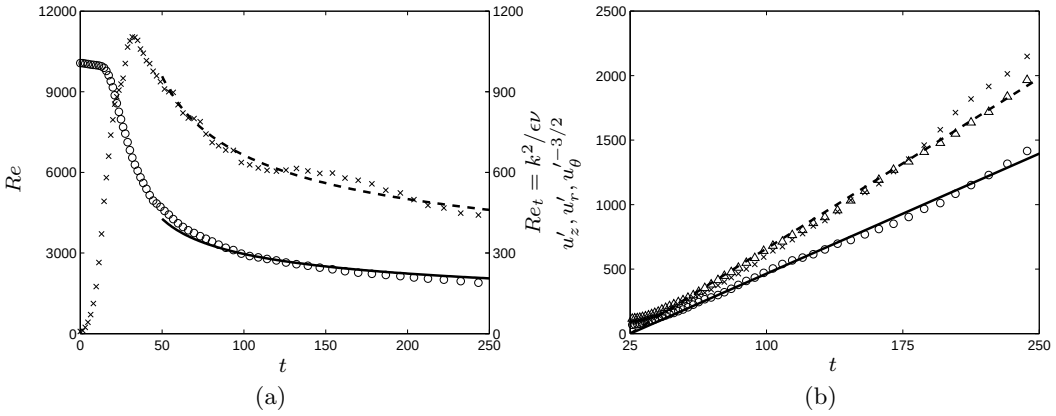


**Figure 3.6:** (a) Variations of $Re$ and $Re_t$ with time (b) rms velocities at $r/l_h$; ($\circ$) $u'_z$, ($\triangle$) $u'_r$, ($\times$) $u'_\theta$ and the lines are fits to the $u'_r$ and $u'_z$ data, with a virtual origin of $t_0 = 25$.

energy per unit mass, remains higher than 300. In view of these relatively high Reynolds numbers, the usual solution having $n = 1/3$ (see section 2.1.1) would be expected to appear. This would have turbulence stress values at fixed $r/l_h$ varying like $t^{-4/3}$. The three fluctuating (rms) velocities at the wake half-width ($r = l_h$) are appropriately plotted in figure 3.6(b) and it is clear that they demonstrate quite a good fit to the expected behaviour, suggesting a virtual origin of about $t_0 = 25$.

The $n = 1/3$ solution predicts that both $Re$ and $Re_t$ will fall like $t^{-1/3}$. Taking the virtual origin to be $t_0 = 25$ and choosing appropriate amplitudes yields the solid and dashed lines shown in figure 3.6(a). Both $Re$ and $Re_t$ behave largely as expected throughout the computation, although the $Re_t$ data show small divergences for $t > 125$. The expected similarity solution also has approximately constant $u'_z/U_d$ at fixed $r/l_h$, as illustrated in figure 3.15(b) (and similarly for the other normal and shear stresses) and the computed data agrees with that expectation only within the $50 < t < 125$ period, drifting somewhat at later times, as might be anticipated from figure 3.6(a).

The variations of the wake half-width and centreline velocity are shown in figure 3.7(a), where values have been normalised by the initial values at $t = 0$. It is evident that good fits to the expected slopes in these log-log plots are observed at least over the restricted period noted above ($25 < t - t_0 < 100$) and perhaps for somewhat longer. Note that the necessary constraint $l_h^2 U_d$ is also closely satisfied at least until $t - t_0 \approx 100$. The velocity profile shown in figure 3.7(b) was obtained by assuming similarity and averaging over the restricted time period. It is quite close to the cosinusoidal variation suggested to provide a reasonable fit by Ostowari & Page (1989), but there is no fundamental reason why one should expect a

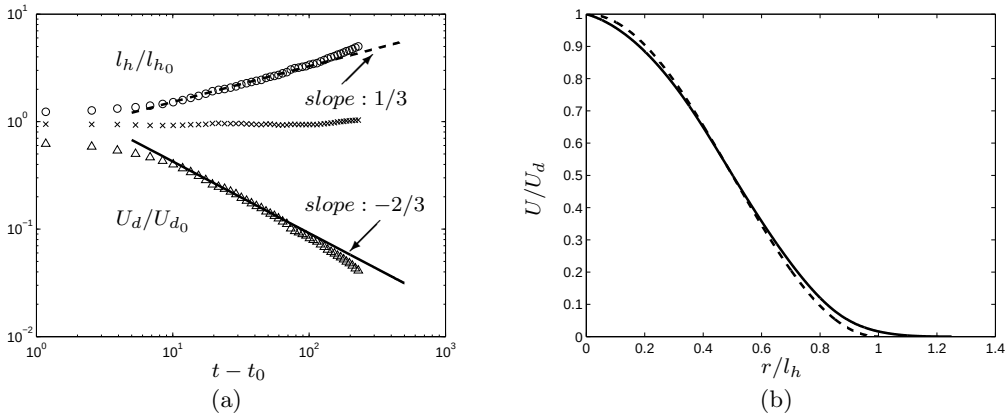


**Figure 3.7:** (a) Variation of wake half-width (○) and maximum deficit velocity (△) with time; (×): $l_h^2 U_d / l_{h_0}^2 U_{d_0}$. (b) the computed mean velocity profile (solid line) compared with a cosinusoidal variation (dashed line).

cosinusoidal velocity variation – this would, for example, require a rather special variation of eddy viscosity if it were to arise naturally from the similarity form of the equations.

As mentioned above, the self-similar behaviour of the higher moments deviates in some respects from its expected form once $t > 125$. Before discussing the reason for that the reader should be aware that some deviation was also evident, after some period, in Gourlay *et al.*'s (2001) and Redford *et al.*'s (in preparation) data, but unfortunately was never explained. In the author's opinion, the most probable reason for that deviation is associated with the ratio $\Lambda_z/2L_z$ which defines whether enough non-correlated data is available for the averaging to converge. A comparison between the two edges of the $50 < t < 125$ period were made and it was found that the ratio fell from $\Lambda_z/2L_z \approx 49$ at $t = 50$ by about 35%. In other words, during the duration of that period the number of non-correlated sets of data was effectively reduced by about 35%. In addition, figure 3.6 shows that the higher moments (i.e. $k$ and $\epsilon$) are the ones which are affected the most, which is expected since the higher moments require more sets of non-correlated data for their average to converge. Finally, since for all the subsequent computations with external turbulence (which are presented in section 3.2.3) the external turbulence was imposed at the *start* of the closely self-similar region (at $t \approx 66$) and the distortions imposed on the subsequent self-similarity development of the wake by the external turbulence became very quickly significant, as illustrated in figure 3.15(b), this issue was not pursued further.

Turbulence quantities were also computed and the dimensionless Reynolds stress profiles are presented in figure 3.8(a). Note that the individual time-dependant profiles presented there were obtained at about equally separated time segments within the self-similar period,

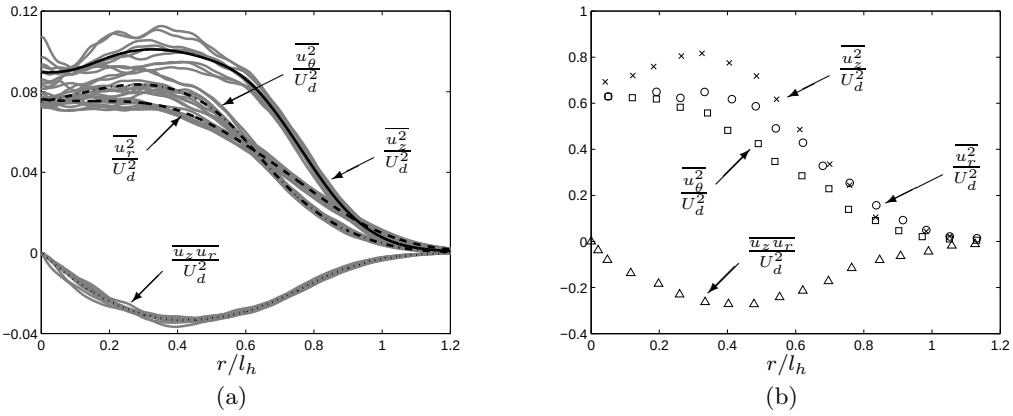


**Figure 3.8:** Profiles of the various dimensionless turbulent stresses in the self-similar wake (a) Present DNS. (b) Uberoi & Freymuth (1970). Note that the black lines in (a) are the self-similar profiles of the various turbulent stresses which were collapsed from their individual time-dependant profiles (grey lines).

$50 < t < 125$, by appropriate circumferential and axial averaging and that their corresponding self-similar profiles were obtained by collapsing those time-dependant dimensionless profiles within the self-similar period, so the self-similar profiles shown are those resulting from time-averaging over that period. Note that the larger scatter evident closer to the centre of the wake was unfortunately unavoidable and is associated with the ineffectiveness of the circumferential averaging in that region. Near $r = 0$ the individual grid points used for the circumferential averaging are physically closer one to the other and so the variables are more correlated. The only possible way to avoid that problem would be to use a longer domain with more grid points in that direction, which was unfortunately not feasible under the available resources. Nevertheless, the self-similar profile shapes agree qualitatively with previously reported data. For example, the Reynolds-stress profiles measured by Uberoi & Freymuth (1970) in the far wake of a prolate spheroid are presented in figure 3.8(b). It is clear that there is about an order of magnitude difference between the two. However, quantitative agreement is not expected since different initial conditions generally produce different profiles (i.e. Bevilaqua & Lykoudis, 1978; Redford *et al.*, in preparation). Nevertheless, note that it was found that the current stress values are very similar to the ones Cannon (1991) measured behind a porous disc (with 49% blockage), where in his measurements $\overline{u_z^2}/U_d^2 \approx 0.09$. In addition, in the current DNS the wake's spreading parameter, $S = (dl_h/dt)/U_d$, is about 0.18 which is quite similar to Cannon's (1991) $S \approx 0.13$. However, it should also be noted for the completion of the comparison that in Uberoi & Freymuth's (1970) measurements $S \approx 1$. Thus, the current wake might be a representative of a wake behind some kind of a porous disc (since the generating body was never modelled), and so the importance of initial conditions in shaping the far wake region is clearly emphasised.

Finally, once all the wake properties were extracted, the turbulence kinetic energy (TKE) balance was calculated using the following equation:

$$\begin{aligned}
\textbf{Rate of Change}: \quad & \frac{l_h}{U_d^3}\frac{\partial\left[\frac{1}{2}\left(\overline{u_z^2}+\overline{u_r^2}+\overline{u_\theta^2}\right)\right]}{\partial t} \\
\textbf{Transport}: \quad & +\frac{1}{r/l_h}\frac{\partial}{\partial\left(r/l_h\right)}\left\{\overline{\frac{r}{l_h}v\left[\frac{p}{\rho}+\frac{\frac{1}{2}\left(u_z^2+u_r^2+u_\theta^2\right)}{U_d^3}\right]}\right\} \\
\textbf{Production}: \quad & -\frac{\overline{u_z u_r}}{U_d^2}\frac{\partial}{\partial\left(r/l_h\right)}\left(\frac{U}{U_d}\right) \\
\textbf{Dissipation}: \quad & +15\nu\frac{l_h}{U_d^3}\overline{\left(\frac{\partial u}{\partial z}\right)^2}=0.
\end{aligned} \tag{3.10}$$

Note that the boundary-layer approximation has been used and, in computing the dissipation term ($\epsilon$), local isotropy of the smallest scales of motion has been assumed. The difference between the resulting value of $\epsilon$ and that obtained by using the exact expression was found to be negligible at a few test points along the wake's profile. Each term is normalised using the characteristic scales, $U_d$ and $l_h$. The data for the transport term were found not to collapse in a satisfactory manner; an example of the scatter noticed in the triple product over the self-similar period is illustrated in figure 3.9(b). Note that in order to reduce the scatter in the triple-velocity product terms an even longer domain would have been required (which was unfortunately not feasible). The transport term was therefore deduced as the balance from the other terms (as was also done by Uberoi & Freymuth, 1970, for example). Figure 3.9(a) shows the resulting TKE balance. Again, only qualitative agreement with previously reported balances is expected. Nevertheless, the absolute value of the ratios between the maximum production to all the maxima of the other terms are of order one, which is similar to what Redford *et al.* (in preparation) reported for one of their wakes – the one that was initiated by a series of ring vortices. On the other hand, in their other wake the ratio was much smaller, about 0.2, in Uberoi & Freymuth's (1970) wake it was about 0.1. Note that the dimensionless production term in the current DNS is of about the same magnitude as was found by Uberoi & Freymuth (1970). That, combined with the fact that the magnitude of the convection term is directly associated to the wake's spreading parameter (which, as discussed earlier, varies with the different initial conditions), explains the variations in the ratios between the different maxima in the different experiments. And so again the importance of the initial conditions in defining the far-wake flow field is clearly demonstrated.

In summary, the computed wake, at least during the $50 < t < 125$ period, is satisfactorily

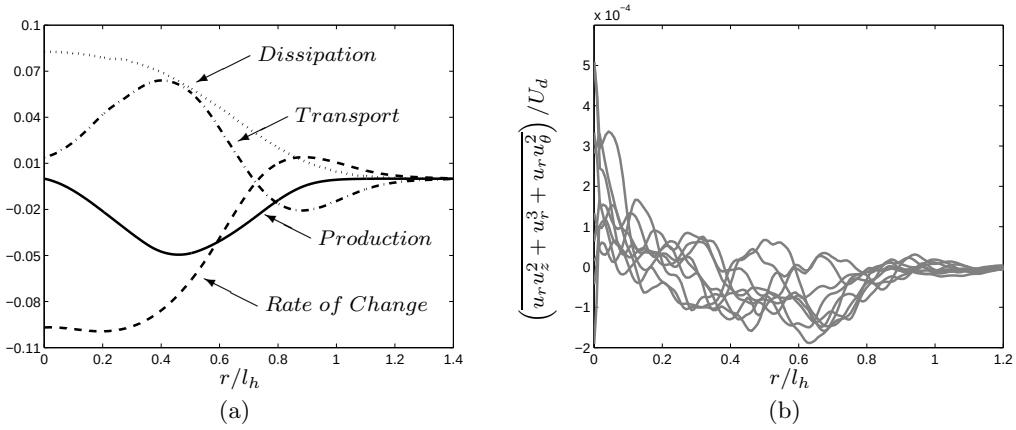


**Figure 3.9:** (a) Profiles of the various dimensionless components of the TKE balance in the self-similar wake. (b) An example of the scatter noticed in the triple product term .

self-similar with $n = 1/3$, yielding mean velocity, stress and TKE profiles qualitatively similar to those previously reported. The Reynolds number is sufficiently high to yield isotropy of the smallest scales and around a decade of inertial sub-range. At the end of this period $t = 125$, $Re = 2800$ and the Taylor microscale Reynolds number $Re_\lambda = u'_z\lambda/\nu = 120$, where $\lambda^2 = 2\overline{u_z^2}/\overline{(\partial u_z/\partial z)^2}$ (i.e. Pope, 2000).

### 3.2.2 Free-stream Turbulence

Three different turbulent flow fields were generated. Since there have been many examples of HIT generated within a box by DNS, as was presented in section 2.2.3, only a brief discussion along with the basic data for the three cases is presented here.

As was mentioned above, to achieve a certain value of $u'_{ze_1}/U_{d_1}$ Sullivan *et al.*'s (1994) forcing scheme was used and the computation proceeded until a fully quasi-stationary state was reached (as explained by Keneda *et al.*, 2003, for example). Figure 3.10(a) shows the time variation of $Re_{\lambda_e}$ and its running average for the $u'_{ze_1}/U_{d_1} = 0.36$ case. Recall that here $U_{d_1}$ is the base-line wake's deficit velocity at $t_1$, the time when it will have the external turbulence field combined with it. Note that the running average converges gradually to an approximately constant value such that additional simulations for $t/T > 30$, where $T = L_{ze}/u'_{ze}$ is one eddy turnover time, showed little further change. Table 3.1 provides a summary of the turbulent characteristics of the three different HIT flow fields at $t_1$.

As soon as the free-stream turbulence was artificially combined with the wake, the Sullivan *et al.* (1994) forcing was removed, so that it was allowed to decay in the usual way. The nature

| Symbol | $u'_{ze_1}/U_{d_1}$ | $L_{ze_1}/l_{h_1}$ | $\lambda_{ze_1}/\lambda_{l_h 1}$ | $\eta_{e_1}/\eta_{l_h 1}$ | $T_{ze_1}/T_{l_h 1}$ | $\lambda_{ze_1}/L_{ze_1}$ | $\eta_{e_1}/L_{ze_1}$ | $Re_{\lambda_e}$ |
|---|---|---|---|---|---|---|---|---|
| △ | 0.09 | 0.75 | 3.34 | 3.39 | 7.33 | 0.5 | 0.0187 | 133 |
| □ | 0.17 | 0.52 | 1.9 | 1.84 | 2.6 | 0.41 | 0.0147 | 146 |
| ○ | 0.36 | 0.60 | 2.06 | 1.3 | 1.5 | 0.35 | 0.0085 | 314 |

**Table 3.1:** Defining parameters of the different free-stream turbulence flow fields at $t_1$; Suffix '$e$' denotes values in the external stream and suffix '$l_h$' denotes wake values at the half-width location. $\lambda$ is the Taylor micro-length scale, $Re_{\lambda_e} = u'_{ze}\lambda_e/\nu$ is the microscale Reynolds number in the free-stream and $L_z$ is the axial integral scale.

of this decay was determined by interrogating the turbulence field well outside the wake, so that it would not be affected by the latter. As was noticed by Ishida *et al.* (2006), isotropic turbulence can decay either like Saffman's turbulence, $K_e \sim t^{-6/5}$, or Batchelor's turbulence, $K_e \sim t^{-10/7}$, depending on initial conditions. In the current simulations it was noticed that the respectively corresponding constraints $K_e L_e^3 = constant$ or $K_e L_e^5 = constant$ both had a temporal decay (recall that this was also noticed for grid turbulence by Krogstad & Davidson, 2010). But the former showed a slightly weaker decay than the latter, suggesting that the DNS turbulence is more Saffman-like, as illustrated in figure 3.10(b). Krogstad & Davidson argue that if the constant $A$ in the empirical decay law

$$\frac{\partial u_z^2}{\partial t} = -A\frac{u_z^3}{L_z} \tag{3.11}$$

falls with $t$ like $A \sim t^{-q}$ Saffman turbulence would yield a decay exponent for $u^2 \sim t^n$ of $n = 1.2(1-q)$ $(q \ll 1)$. The current data do indeed show a slow fall in $A$ with $t$ and fits to the turbulence energy history with $n = 1.15$ are reasonable, as shown in figure 3.11, and consistent with expectations. Note, however, that the strongest case requires a slightly smaller value of $n$ which is consistent with the slightly faster drop in $A$.

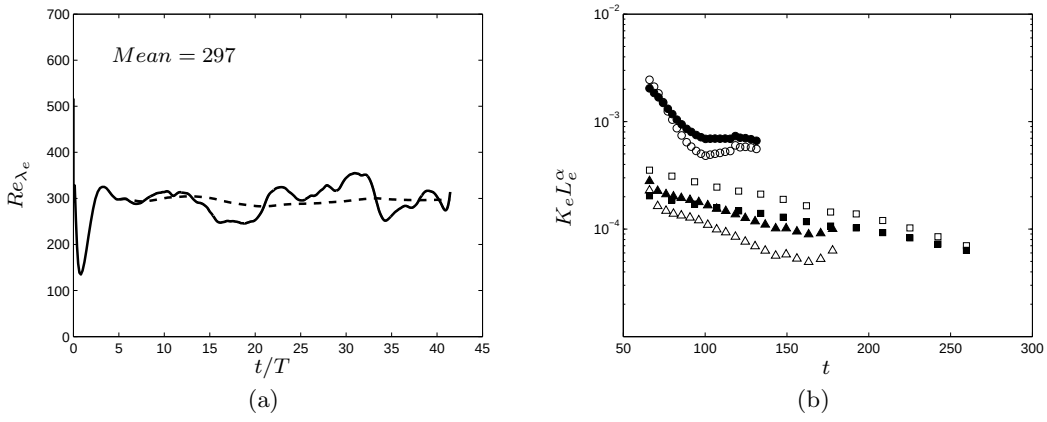


**Figure 3.10:** (a) Taylor microscale Reynolds number vs. $t/T$. Solid line: DNS result; dashed line: trace of $Re_{\lambda_e}$'s mean. (b) Saffman and Batchelor's turbulence constrains; Weak (△), medium (□) and strong (○) turbulence cases. Open symbols $\alpha = 3$ and close symbols $\alpha = 5$.

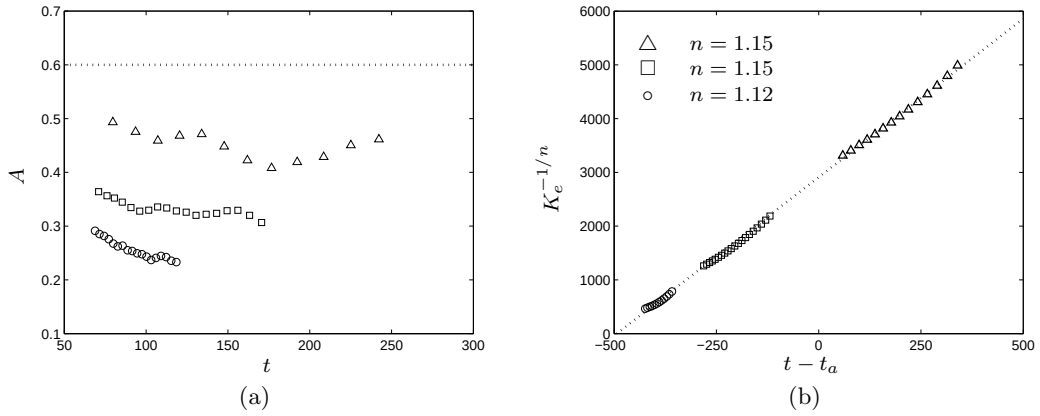


**Figure 3.11:** (a) Variations of $A$ with time. (b) Decay of TKE ($k_e \sim t^{-n}$) in the external turbulence; Weak (△), medium (□) and strong (○) turbulence cases, where $t_a$ is an arbitrary origin chosen so they would all fit on the same line.

Figure 3.12 shows axial velocity compensated spectra, averaged in space over the entire domain, for all three cases at various times throughout their decay, plotted in the usual way

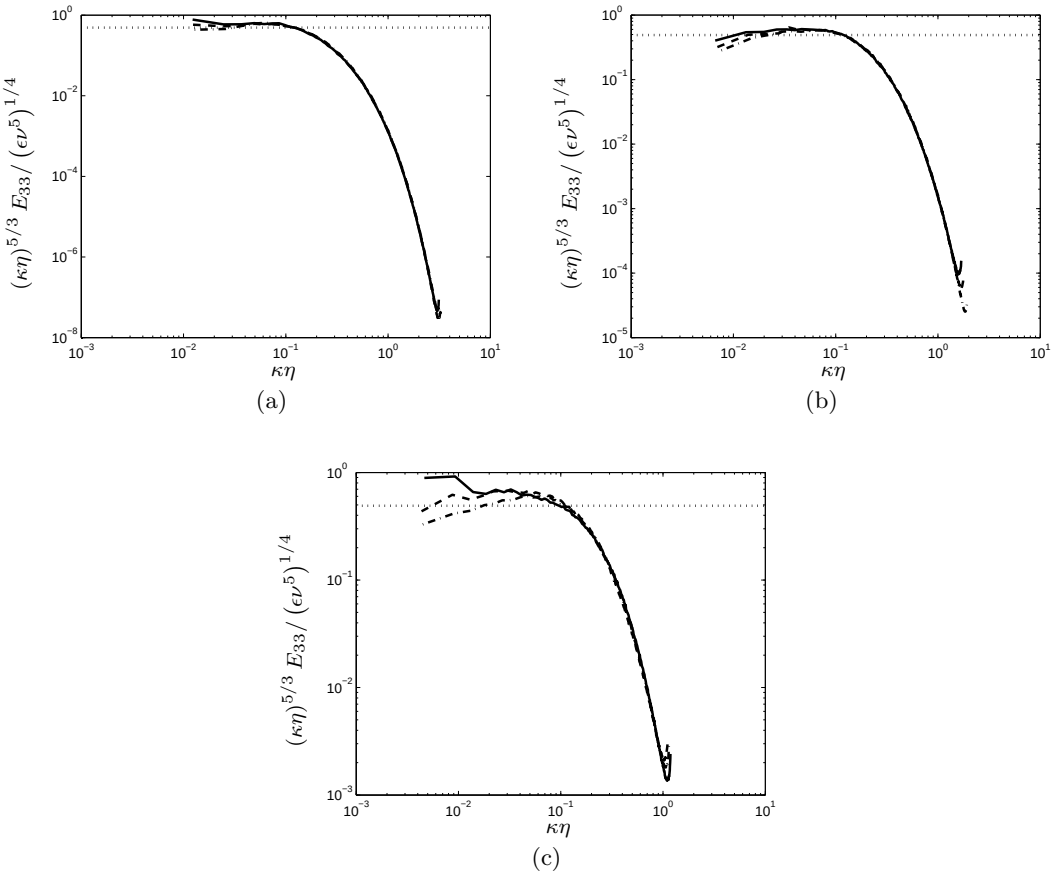


**Figure 3.12:** Axial velocity one-dimensional compensated energy spectrum of the (a) weak, (b) medium and (c) strong external turbulence cases at different times; Solid lines: $t = t_1$, dashed lines: $t \approx 148, 113$ and 97 in (a), (b) and (c) respectively, dashed-dot lines: $260, 178$ and 131 in (a), (b) and (c) respectively. Dotted horizontal lines: the universal value in the inertial sub-range.

to emphasise collapse in the inertial subrange and the extent of this range. In all three cases the latter is comparable with the extent of the inertial range in the pure wake spectrum (see figure 3.1(a)). Note that the range of the (normalised) scales captured by the simulation is rather smaller for the higher energy cases, since Kolmogorov scales are larger in those cases (see table 3.1). Note also that the low-wavenumber region in which one expects the regular spectral values to flatten out and the compensated spectral values to fall towards zero is not captured; this is a result of the finite length domain. Recall that the domain used for creating the external turbulence was only a quarter in length of that for the pure wake (see sections 3.1.2 and 3.1.4).

To conclude, the three HIT flows show reasonable consistency and agreement with previously reported ones, but it is emphasised again that the influence of initial conditions can undoubtedly lead to different behaviour.

### 3.2.3 Wake Embedded in External Turbulence

Once the pure wake and the turbulent flows were achieved separately they were artificially combined (as was explained in section 3.1) and the whole field – wake plus external turbulence, was then allowed to develop and decay with time.

In the light of the discussion in section 2.3, the first anticipated feature was that the presence of external turbulence will enhance the decay rate of the wake. Figure 3.13 shows the wake growth and the corresponding decay of the centreline velocity. The external turbulence was in each case imposed at $t \approx 66$. It is immediately obvious that increasing levels of external turbulence cause substantial changes, although these appear to be small for the weakest turbulence case. Since it is not known *á priori* whether similarity is possible nor, even if it is, what the virtual origin would be for that region of the wake, it is not sensible to use log-log plots like these to deduce decay rates. Figure 3.14(a) shows the deficit velocity plotted as $AU_d^{-1/2n}$, where is $A$ is a constant, *vs.* $t$ for the three cases, compared with the pure wake case. The value of $n$ has been chosen in each case to yield reasonable straight lines after an initial adjustment region; these values are 0.33, 0.4 and 0.5 in the order of increasing $u'_{ze_1}/U_{d_1}$ (which are presented in table 3.1), compared with 1/3 for the pure wake case. Clearly, as deduced from figure 3.13, although the decay rate for the weakest external turbulence case is not noticeably different from that of the pure wake, the rate of decay thereafter increases with the strength of the external turbulence. This is unlike the behaviour

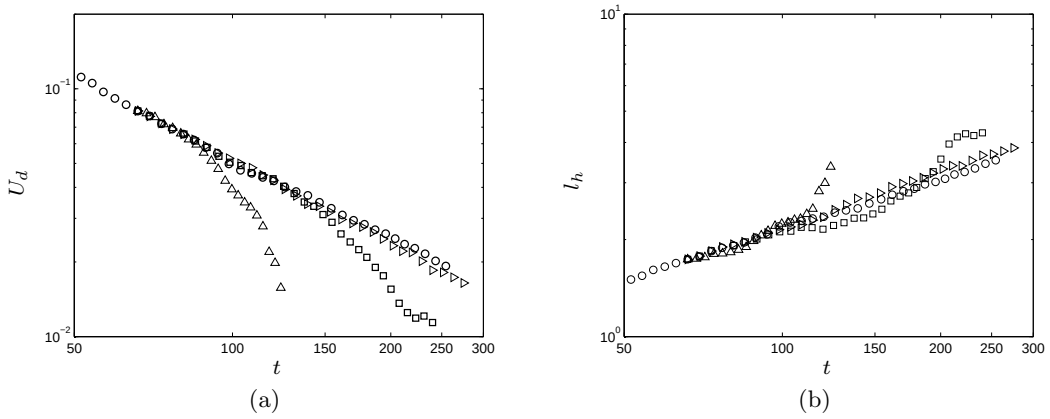


(a) (b)

**Figure 3.13:** Decay of the deficit velocity (a) and the growth of wake half-width (b); (○) $u'_{ze_1}/U_{d_1} \approx 0$, (▷) $u'_{ze_1}/U_{d_1} = 0.09$, (□) $u'_{ze_1}/U_{d_1} = 0.17$ and (△) $u'_{ze_1}/U_{d_1} = 0.36$ (for more turbulence parameters refer to table 3.1).

reported by Wu & Faeth (1994) and Legendre *et al.* (2006) who each noticed only one decay rate ($U_d \approx x^{-1}$ and $U_d \approx x^{-2}$, respectively). Yet, the present trend is in agreement with the initial work of Redford & Coleman (2007). It is also clear that the effect of the free-stream turbulence does not take place instantaneously but is delayed by a time that decreases with increasing $u'_{ze_1}/U_{d_1}$. By examining truncation errors and energy spectra it was found that the stronger the external turbulence, the longer the correction stage was but in all three cases it was shorter than 13.8 (non-dimensionalised) time units. Therefore, the correction stage presumably has little influence on the time taken to affect the decay rate.

Although a reasonable power law fit to $U_d \sim t^{-2n}$ seems possible in every case, figure 3.14(b) demonstrates that self-similarity does not hold, even approximately, at least for the two stronger turbulence cases, since $U_d l_h^2$ does not remain even approximately constant. Moreover, neither mean velocity nor turbulence profiles can be collapsed in self-similar form

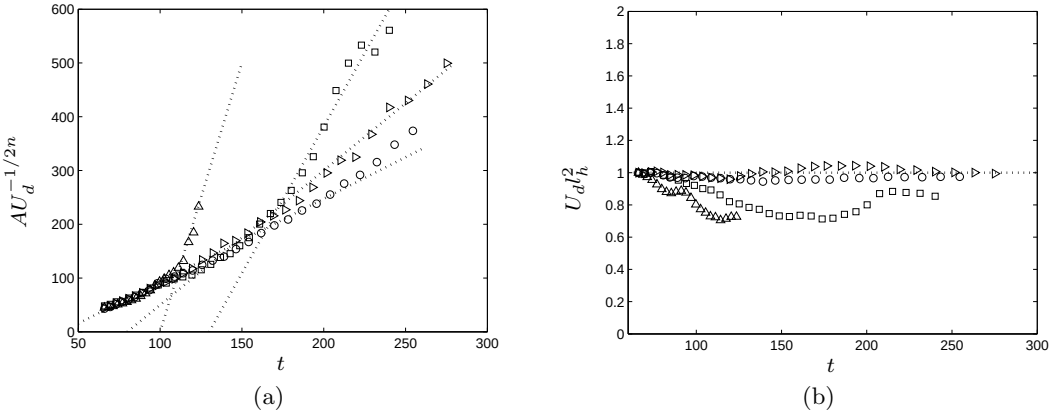


(a) (b)

**Figure 3.14:** Variations of $AU_d^{-1/2n}$ (a) and $U_d l_h^2$ (b); (○) $u'_{ze_1}/U_{d_1} \approx 0$, (▷) $u'_{ze_1}/U_{d_1} = 0.09$, (□) $u'_{ze_1}/U_{d_1} = 0.17$, (△) $u'_{ze_1}/U_{d_1} = 0.36$ and the dotted lines in (a) are linear fits.

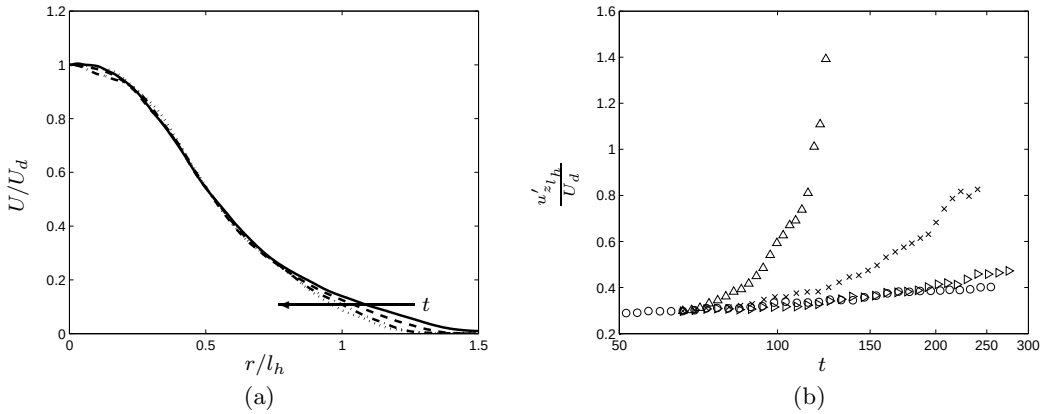


**Figure 3.15:** (a) Illustration of dimensionless deficit velocity profile with time in the case where $u'_{ze_1}/U_{d_1} = 0.09$; Solid line $t = 150$, dashed line $t = 169$, dash-dot line $t = 193$ and dotted line $t = 210$. (b) $u'_{z_{l_h}}/U_d$ vs. time; ($\circ$) $u'_{ze_1}/U_{d_1} \approx 0$, ($\triangleright$) $u'_{ze_1}/U_{d_1} = 0.09$, ($\square$) $u'_{ze_1}/U_{d_1} = 0.17$ and ($\triangle$) $u'_{ze_1}/U_{d_1} = 0.36$.

(as discussed below). Assuming such collapse, so that $U = U_d f(\eta)$ where $\eta = r/l_h$, is what leads to $U_d l_h^2 =$ constant (as was discussed in section 2.1.1). Figure 3.14(b) suggests, however, that in the weakest external turbulence case, the wake may in fact revert to the usual self-similar form since, after an initial variation, $U_d l_h^2$ becomes closely constant again – beyond about $t = 150$. However, careful examination of the non-dimensional mean velocity profiles at various times in the $t > 150$ regime revealed that they are only partly self-similar – only their inner regime collapses, in a roughly satisfactory manner, while their edge does not due to a gradual increase with time in the mean shear there, such that the non-dimensional profile gets slightly narrower, as illustrated in figure 3.15(a).

The time-variation of the ratio $u'_{z_{l_h}}/U_d$, where $u'_{z_{l_h}}$ is the rms axial velocity fluctuations at the wake's half-width location, is shown in figure 3.15(b). Notice again that the divergence from the pure wake data (for which the ratio is approximately constant) is increasingly more rapid and larger as $u'_{ze_1}/U_{d_1}$ increases. In addition, the fact that its value did not converge to a new constant value suggests that the wake does not reach a new self-similar state for the times considered.

The non-dimensional profiles of the different normal turbulence stresses were also examined. They change with time, each from its original self-similar profile into one which is more closely uniform and clearly determined by the external turbulence intensity – higher values of $u'_{ze_1}/U_{d_1}$ lead to more rapid and larger effects, as noted earlier; examples are presented in figure 3.16. On the other hand the non-dimensional turbulence shear stress was found to increase with $u'_{ze_1}/U_{d_1}$ and not become approximately zero as it is does the free-stream, as

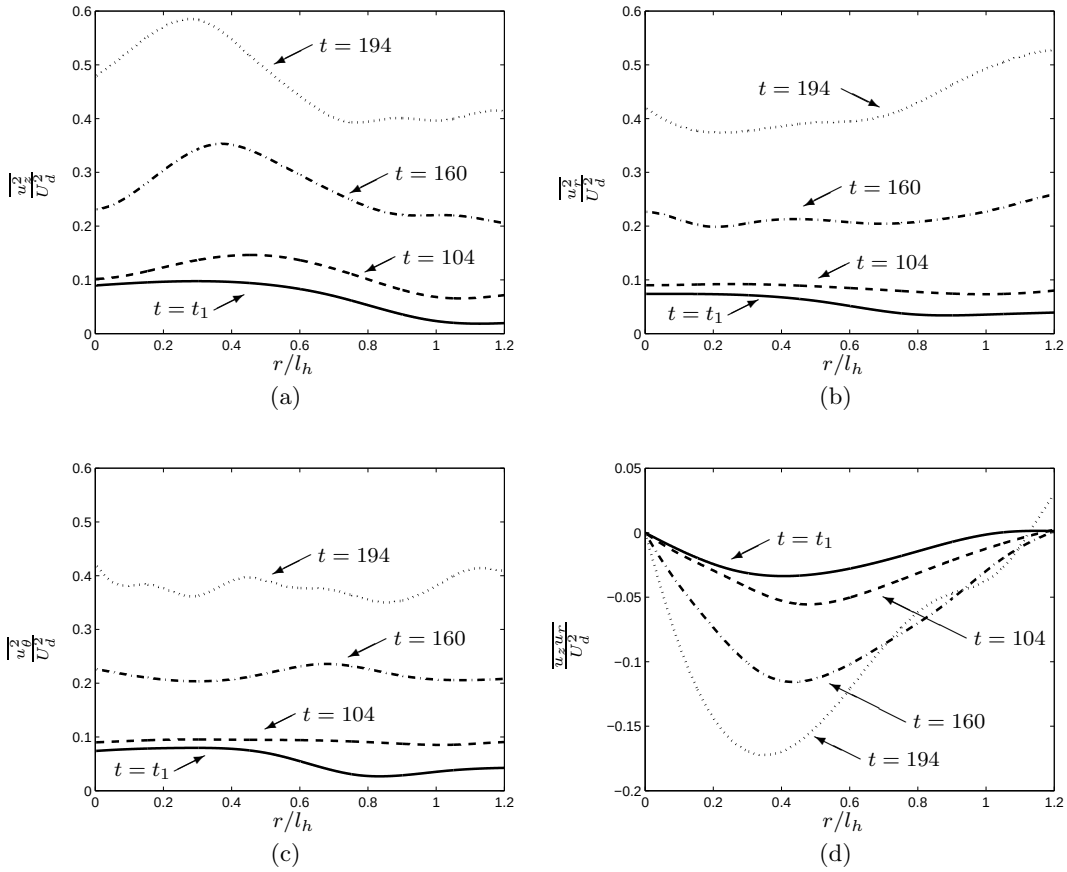


**Figure 3.16:** Profiles of (a) $\overline{u_z^2}/U_d^2$, (b) $\overline{u_r^2}/U_d^2$, (c) $\overline{u_\theta^2}/U_d^2$ and (d) $\overline{u_z u_r}/U_d^2$ at different times in the case where $u'_{ze_1}/U_{d_1} = 0.17$.

if the free-stream turbulence increased the turbulence shear stress production. In order to confirm that finding the shear-stress transport equation was evaluated, with

$$
\begin{aligned}
\textbf{Rate of Change}: \quad & \frac{l_h}{U_d^3}\frac{\partial \overline{u_z u_r}}{\partial t} \\
\textbf{Transport}: \quad & + \frac{1}{r/l_h}\frac{\partial}{\partial\,(r/l_h)}\left(\frac{r}{l_h}\frac{\overline{u_z u_r u_r}}{U_d^3}\right) - \frac{l_h}{r}\frac{\overline{u_z u_\theta u_\theta}}{U_d^3} \\
& - \frac{l_h}{U_d^3}\overline{\frac{p}{\rho}\left(\frac{\partial u_z}{\partial r} + \frac{\partial u_r}{\partial z}\right)} \\
& + \frac{l_h}{U_d^3}\frac{1}{\rho}\left(\frac{\partial \overline{p u_z}}{\partial r} + \frac{\partial \overline{p u_r}}{\partial z}\right) \\
& - \frac{\nu}{U_d l_h}\frac{\partial}{\partial\,(r/l_h)}\left[\frac{l_h}{r}\frac{\partial}{\partial\,(r/l_h)}\left(\frac{r}{2l_h}\frac{\overline{u_z u_r}}{U_d^2}\right)\right] \\
\textbf{Production}: \quad & + \frac{\overline{u_r u_r}}{U_d^2}\frac{\partial\,(U_z/U_d)}{\partial\,(r/l_h)} \\
\textbf{Dissipation}: \quad & + \epsilon_{uv} = 0.
\end{aligned}
\tag{3.12}
$$

Note that the production of shear stress is the product of normal Reynolds stress and mean shear. Thus, the fact the $\overline{u_r u_r}/U_d^2$ increases with time (as illustrated in figure 3.16(b)) com-

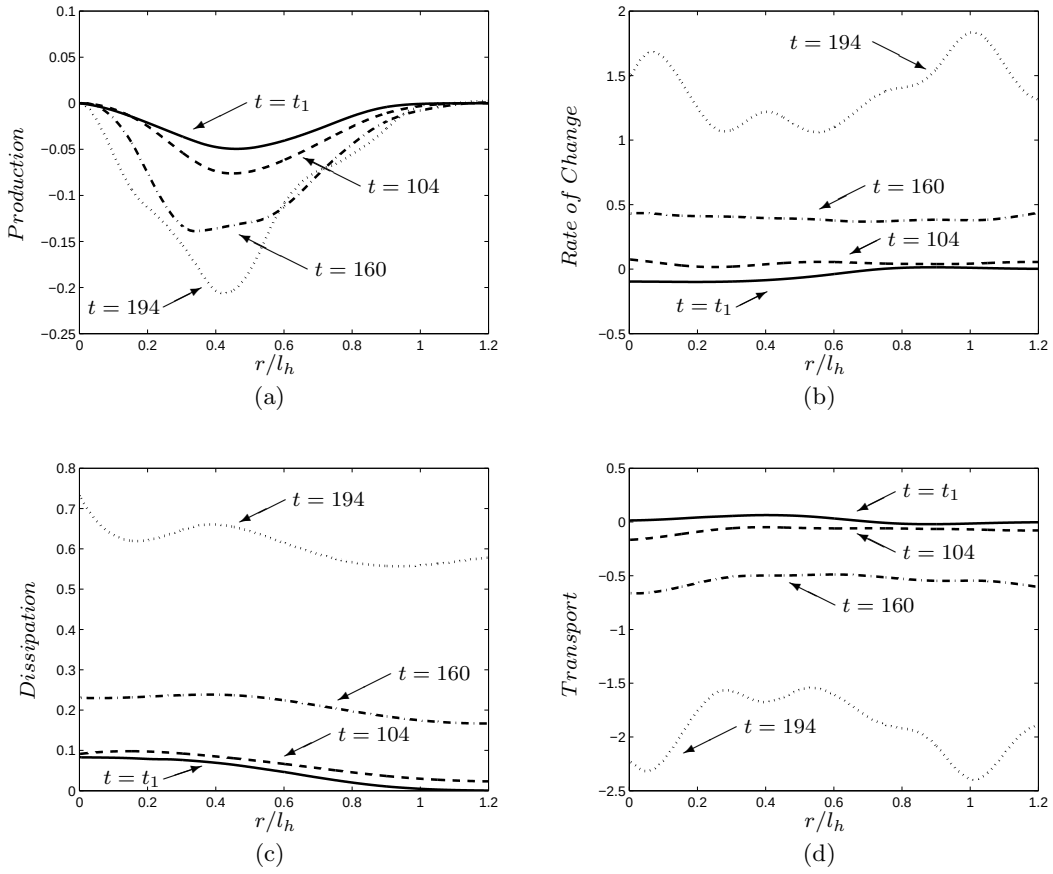


**Figure 3.17:** Dimensionless profiles of the different TKE balance components: (a) production, (b) rate of change, (c) dissipation and (d) transport, at different times for the case where $u'_{ze_1}/U_{d_1} = 0.17$.

bined with the presence of the mean shear (which hardly varies) increases the shear stress production and is the reason for the increase in the non-dimensional turbulence shear stress. Figure 3.17 shows the corresponding development of the dimensionless TKE balance (see equation 3.10). It was found (and can also be noticed in figure 3.17) that the dimensionless convection, dissipation and transport terms of the TKE balance increase in value and their profiles become more uniform, as was noticed for the normal turbulent stresses. The production term, on the other hand, keeps its form but increases in value, as would have been expected from the shear stress profile. Thus, the form of the turbulent production relates directly to the mean shear profile while the form of the other terms develop with time and becomes uniform. Note that in HIT the rate of change is determined solely by the dissipation while the other terms are zero (and was noticed in all the external turbulence cases to be true). Here, on the other hand, the presence of the mean shear with the enhanced transport of turbulence from the external turbulence into the wake did not allow this state to occur (at least within the scope of the current simulations).

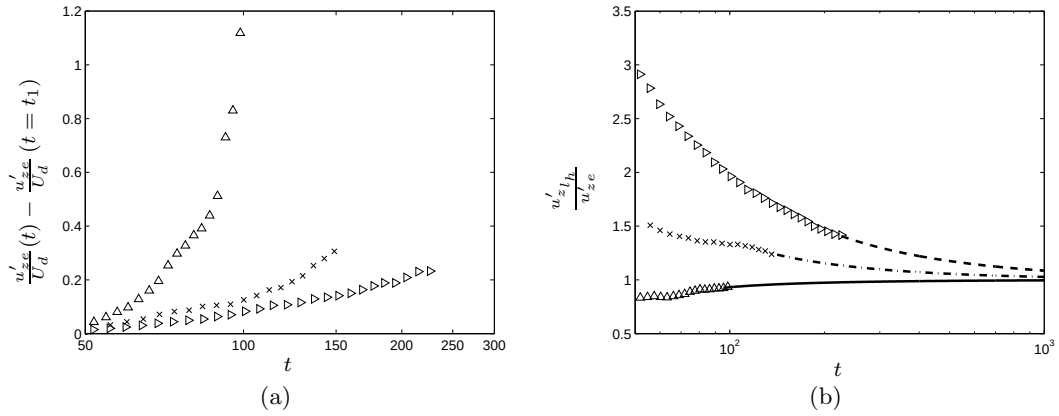


(a) (b)

**Figure 3.18:** (a) The change in $u'_{ze}/U_d$ vs. time for the different wake-background combinations; (▷) $u'_{ze_1}/U_{d_1} = 0.09$, (□) $u'_{ze_1}/U_{d_1} = 0.17$ and (△) $u'_{ze_1}/U_{d_1} = 0.36$. (b) Variation with time of the ratio of axial intensity at $l_h$ to free-stream intensity; (▷) $u'_{ze_1}/U_{d_1} = 0.09$, (□) $u'_{ze_1}/U_{d_1} = 0.17$ and (△) $u'_{ze_1}/U_{d_1} = 0.36$.

Figure 3.18(a) shows why self-similarity is not achieved: the natural decay in the free-stream turbulence intensity is significantly less rapid than the decay of the wake centre-line deficit velocity, so $u'_{ze}/U_d$ (the major controlling parameter) continually rises with time. This point is emphasised in figure 3.18(b), which shows that the ratio of the half-width intensity, $u'_{z_{l_h}}$, to the free-stream intensity, $u'_{ze}$, continually falls (or, in the case of $u'_{ze_1}/U_{d_1} = 0.37$, rises) towards what must be the eventual state in which $u'_{z_{l_h}} = u'_{ze}$. Thus, since the wake's rms velocity profiles must eventually be determined by the background, which is decaying relatively slower, no self-similar state can be achieved.

As mentioned earlier, the non-dimensional rms velocity fluctuations profiles develop with time to ones which are eventually determined by their values in the (isotropic) free-stream, so one might predict that at least for the two stronger backgrounds the turbulence normal stress profiles inside the wake will eventually become both isotropic and uniform. They do indeed tend to be more isotropic and uniform, as illustrated in figure 3.16. But careful examination of the turbulent shear stress profiles inside the wake reveals that $\overline{u_z u_r}$ does not decay to zero as rapidly as the fluctuating profiles change towards uniformity, as can be noticed in figure 3.16(d). That behaviour, as was discussed above, is associated with the continuing presence of shear in the mean flow and the increase in $\overline{u_r u_r}/U_d^2$, and it shows that the wake turbulence does not become strictly isotropic.

Nevertheless, by using Lumley's triangle (i.e. Pope, 2000; Simonsen & Krogstad, 2005) one can characterise the local anisotropy/isotropy of the turbulence inside and outside the wake and compare them. The method is based on the analysis of the normalised Reynolds

stress anisotropy tensor:

$$b_{ij} = \frac{\overline{u_i u_j}}{2K} - \frac{1}{3}\delta_{ij}, \tag{3.13}$$

where $\delta_{ij}$ is the Kronecker delta. This tensor has real eigenvalues ($\lambda_1$, $\lambda_2$, $\lambda_3$) and in incompressible flow (since the first invariant, $I_1$, is always zero) it can be characterised by only the second ($I_2$) and the third ($I_3$) invariants:

$$\begin{aligned} I_1 &= b_{kk} = 0, \\ I_2 &= -\frac{1}{2} b_{ij} b_{ji} = -3\eta^2, \\ I_3 &= \det(b_{ij}) = 2\xi^3. \end{aligned} \tag{3.14}$$

Lumley showed that each realisable state in a turbulent flow corresponds to a point that is located inside a "triangle" on the anisotropy invariant plane $(\xi, \eta)$. Figure 3.19(a) shows Lumley's triangle. The three bounding curves of the triangle correspond to special states: isotropic turbulence is found at the origin ($\xi = \eta = 0$). The two lines leaving from the origin correspond to axisymmetric turbulence, for which two components have the same energy content. Each of these lines have a limiting value. In the first case the two identical diagonal terms are smaller than the third element and tend to zero. This leads to a one-component state of turbulence (point $1C$ in figure 3.19(a)). The other possibility is that the two identical elements dominate so that the third component is negligible. This leads to the two-component axisymmetric limit (point $2C$ in figure 3.19(a)). The curve joining one- and two-component axisymmetric turbulence states represents all the other possible states where only two diagonal components exist. Figure 3.19(b) shows that the turbulence penetrates progressively with time such that the turbulence inside the wake is evolving (with time) from its self-similar far wake state, where one velocity component was more dominant than the other two, towards the one in the free-stream, a state which is close to isotropic turbulence.

In summary, the external turbulence clearly impacts the structure and development of the far axisymmetric wake, such that it increases the entrainment rate of fluid into the wake, which consequently increases the decay rate of the wake. It should be stressed that the wake's mean axial mass flux,

$$\dot{m}_f = \int_0^{2\pi} \int_0^{\infty} \rho U_z r \mathrm{d}r \mathrm{d}\theta, \tag{3.15}$$

is constant both at each streamwise station and in time in the simulation (as a result of

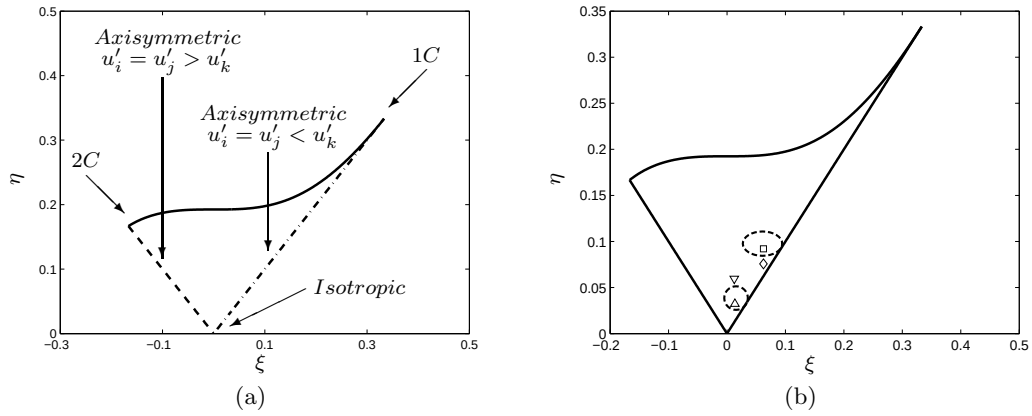


**Figure 3.19:** The Lumely triangle (black lines) on the plane of the invariants $\xi$ and $\eta$ of the Reynolds-stress anisotropy tensor; (a) The anisotropy invariant map. (b) Development of the turbulence at the wake half-width with time for the wake embedded in free-stream turbulence with initial $u'_{ze_1}/U_{d_1} = 0.36$, where ($\square$), $t = t_1$, ($\diamond$), $t = 94$, ($\bigtriangledown$), $t = 112$ and ($\bigtriangleup$), $t = 130$, black dashed circle – the free-stream turbulence regime and black dashed ellipse – the self-similar pure wake regime.

the fact that the time-dependent parallel axisymmetric wake is homogeneous in both the circumferential and axial directions which leads, using the continuity equation, to a zero mean radial velocity). Finally, the fact that the mean wake and the external turbulence decay at different rates leads to the unavoidable breakdown of the wake's self-similarity.

Chapter 4

# Wind Tunnel Experiments

## 4.1 Methodology

The University of Southampton's open circuit $3' \times 2'$ wind tunnel was used for the experimental part of the research. The wind tunnel's test section dimensions are 0.6m×0.9m×4.5m and its measured free-stream intensity is below about 0.2% which from now on will be referred to as a uniform free-stream. The wind tunnel has a two-dimensional traverse system which can be placed in different locations along the test section and is controlled by a computer. A few parts of the wind tunnel had to be redesigned such that they would better fit the current study. Among them are a new slots system for the wind tunnel's traverse system, mounting support and wire stretching mechanism for the disc (see below) and cross hot-wire angle calibration device. Moreover, a computer-controllable speed control system was added to the wind tunnel and was implemented in the wind tunnel's EnFlo software (from the University of Surrey, UK) to increase productivity.

The wake's generating body was a 90° conical disc with base diameter of $D = 10$mm. The disc was mounted in the centre of the test section using a set of Berkley Whiplash Braid Moss Green fishing lines with a diameter of 0.06mm and with its base facing upstream and perpendicular to the flow (note that the wire's Reynolds number is about 166 times smaller than the disc's). The disc's Reynolds number based on its diameter, $D$, and the free-stream velocity, $U_0$, was about $Re_D = 15000$ for far-wake measurements and about $Re_D = 5600$ for near wake measurements. Higher turbulence levels (than the wind tunnel's empty free-stream levels) were generated using two bi-planar grids. One was made from square aluminium bars with solidity $d/M \cong 0.27$, where $d = 6.35$mm is the square bar's diameter and $M$ is the mesh spacing, and one from stainless steel round bars with $d/M \cong 0.15$, where $d = 1.63$mm. For clarity, figure 4.1 shows an illustration of the experimental setup inside the wind tunnel.

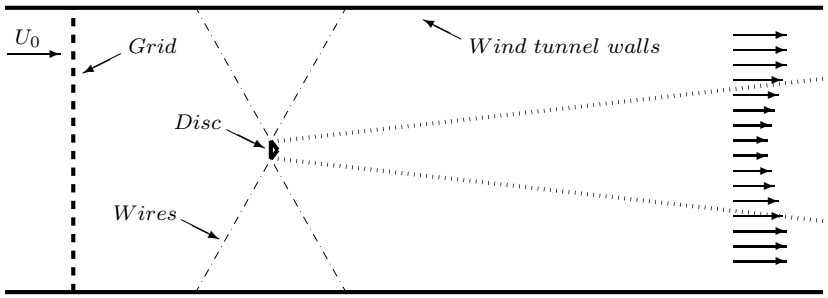


**Figure 4.1:** Illustration of the experimental setup.

### 4.1.1 Measurement Techniques and Uncertainty

Measurements in the far-wake region were done using a standard constant temperature Hot Wire Anemometry (HWA) system (both AALab AN-1005 and Newcastle NSW bridges were used with low-pass filters set at 2800Hz and 3200Hz, respectively). The hot-wire used in this work was a Dantec standard 45° cross wire with a 2.5 $\mu$m wire diameter mounted on a Dantec 6mm diameter 55H24 probe support. Each measurement consisted of 147 blocks each containing 16384 samples obtained at 10000Hz. In addition, two pitot-static tubes (connected to two Furness Controls FCO12 micromanometers) were used to measure the mean free-stream velocity, one far upstream (used as the wind-tunnel reference velocity) and one at the same cross-section as the hot-wire (used to measure the local free-stream velocity during measurements and for reference while calibrating the hot-wire). All analogue signals (both from the hot-wire and the pitot-static tubes) were digitised using a National Instruments USB-9162 Analog - Digital Converter and recorded by the EnFlo software. The software was used for simultaneously controlling, calibrating and recording all the wind tunnel's devices and instrumentation.

In addition to the far-wake measurements, near-wake measurements were obtained using LaVision's high-frequency 2D Particle Image Velocimetry (PIV) system. The system was controlled using LaVision's DaVis Imaging Software, with each measurement composed of 2700 double frame digital photos taken at $50Hz$, where the time between each pair was $15\mu s$. The camera was a $1024 \times 1024$ pixel device showing an area of about $3.8D \times 3.8D$ at the cross-section running through the middle of the disc.

The repeatability errors in any of the hot-wire and pitot-tube measurements were less

than 0.2%. Maximum error estimations for the PIV measurements were done using the finite sample size errors technique described by Castro (1989). For the mean values the technique states that the standard error of the mean is the standard deviation of the error in the sample mean,

$$\widehat{\overline{x}} = \frac{1}{N}\sum_{i=1}^{N} x_i, \tag{4.1}$$

where $N$ is the number of uncorrelated samples, relative to the true mean, $\overline{x}$, since the sample mean is an unbiased estimator. Now using $\widehat{\overline{x}}$ and recognising that the resulting $z$, defined by:

$$z = \frac{\left(\widehat{\overline{x}} - \overline{x}\right)}{\sigma/\sqrt{N}}, \tag{4.2}$$

where $\sigma^2$ is the variance of the signal, is normally distributed (for large $N$), it can be stated with a probability of $(1-\alpha)$ that

$$-z_{\alpha/2} < \frac{\left(\widehat{\overline{x}} - \overline{x}\right)}{\sigma/\sqrt{N}} < z_{\alpha/2}, \tag{4.3}$$

where $z_{\alpha/2}$ is the value of $z$ which gives

$$\frac{1}{\sqrt{2\pi}}\int_z^\infty e^{-t^2/2}\mathrm{d}t = \frac{\alpha}{2}. \tag{4.4}$$

In other words, an estimate of the mean value from an uncorrelated sample of size $N$ will have an error $\varepsilon_x$ less than $z_{\alpha/2}\sigma/\sqrt{N}$ with a probability of $(1-\alpha)$. This means that with a probability (or confidence) of $(1-\alpha)$ the interval from $\widehat{\overline{x}} - z_{\alpha/2}\sigma/\sqrt{N}$ to $\widehat{\overline{x}} + z_{\alpha/2}\sigma/\sqrt{N}$ contains the true mean value $\overline{x}$. Confidence statements regarding the likely error in $\sigma$ estimates can (for the case where $N$ is large enough) be made in a similar way to those for $\overline{x}$ estimates, such that with a probability of $(1-\alpha)$ the interval from $\sigma^2\left(1 - z_{\alpha/2}\sqrt{2/N}\right)$ to $\sigma^2\left(1 + z_{\alpha/2}\sqrt{2/N}\right)$ contains the true variance $\overline{\sigma^2}$. Error estimations for the PIV measurements (with $N = 2700$) based on the method described above showed that the maximum error in the mean velocity was 1.3% and in the mean-square velocity fluctuations was 5.3% with a probability of 95%. Note that all the samples were assumed to be uncorrelated since they were taken at $50Hz$, which is more than five times smaller than the vortex shedding frequency.

Last, Reynolds number variations throughout any set of measurements (using any of the measurement techniques) was less than 0.1%.

### Pitot-Static Tube Calibration

As indicated above, the mean free-stream velocity was measured far upstream and in the same cross section as the HWA measurements were taken using two pitot-static tubes. They were each connected to a different FCO12 micromanometer. Each micromanometer needed its own analogue/voltage output calibration (which varies linearly with the pressure). Such calibration was carried out once every few weeks (during which they showed insignificant variation in their voltage output).

### Hot-Wire Calibration Process

The hot-wire calibrations were carried out against a Pitot-static probe (while both were located in the free-stream at the same cross-section) before each set of measurements (taking approximately an hour each, such that the drift throughout each set was less than 1%. Note that the largest source of error was due to variations in the ambient temperature in the laboratory. And so for each set of measurement it was verified that the ambient temperature in the laboratory did not vary by more than one degree Kelvin). Nevertheless, drift evaluation and correction were carried out, assuming a linear drift during the measurement period. The velocity calibration process involved sampling several values at different air speeds and then a curve fitting was made according to a slightly modified version of King's law,

$$V_{HWA}^2 = A + B \times U^n, \tag{4.5}$$

where $V_{HWA}$ is the voltage applied to the wire and $A$ and $B$ are calibration coefficients. The velocity exponent was allowed to vary to improve the curve-fit (unlike in King's law where $n = 0.5$).

Since cross hot wires were used, yaw calibration was also needed. That was carried out once every few weeks (since the cross hot wires showed insignificant variation in yaw over this time). The process utilised a cosine law fit for the variation in the measured velocity with onset flow angle. A single value for the effective angle is used for each wire together with the constants from Equation 4.5. Throughout the yaw calibration the wind tunnel's velocity, $U$, was held constant and the probe was rotated to different angles, $-20^\circ \leq \Delta\Gamma \leq 20^\circ$ with increments of $5^\circ$. The voltage, maintaining constant temperature in each yawing wire, was

assumed to follow,

$$V_{HWA}^2 = A + B \times [U \cos(\Gamma_{ref})]^n , \tag{4.6}$$

where $\Gamma_{ref}$ is the wire's effective angle. Note that an initial velocity calibration was needed before conducting the yaw calibration (since $A$,$B$ and $n$ are needed). It follows that for a wire rotated through $\Delta\Gamma$,

$$V_{HWA_{\Delta\Gamma}}^2 = A + B \times [U \cos(\Gamma_{ref} + \Delta\Gamma)]^n , \tag{4.7}$$

thus the following could be written and used to find $\Gamma_{ref}$,

$$\left\{ \frac{V_{HWA_{\Delta\Gamma}}^2 - A}{V_{HWA_0}^2 - A} \right\}^{1/n} - \cos(\Delta\Gamma) = -\tan(\Gamma_{ref}) \sin(\Delta\Gamma) . \tag{4.8}$$

This was all programmed within the EnFlo software calibration routines.

### PIV Vector Field Computation

Before extracting the vector field from each frame pair, some work was done on each of the images in order to increase the accuracy of the vector calculation process. First, the large-scale background reflections were removed in order to achieve images with constant background level (without affecting the particles' signal). The large-scale background reflection length was chosen to be at least eight pixels, which is more than twice the particles' diameter of less than three pixels (as was recommended in the system's manual). Second, due to the fact that the particles were not precisely mono-disperse their intensity varies as well. Thus, smaller particles would potentially contribute less in the correlation process. For that reason, the Davis' MINMAX-filter was applied in order to achieve homogeneous particle intensities such that all particles will contribute the same in the correlation process. Third, the area of the disc and the supporting wires were masked out and were not taken into account in the correlation process.

Once the pair of images were 'improved' it was possible to start the vector calculation process. Since two single-exposed images were taken, the cross-correlation method was used. That technique was used in three passes with a decreasing interrogation window size ($64 \times 64$ pixels, $32 \times 32$ pixels and $16 \times 16$ pixels, which in physical length units are $0.24D \times 0.24D$,

$0.12D \times 0.12D$ and $0.06D \times 0.06D$), where the smallest interrogation window captured about five particles on average. The two larger ones were calculated in one iteration with no overlapping while the smallest one was calculated in two iterations with 50% overlapping. The correlation function used was the normalised correlation function where the first two passes were calculated in second-order correlation mode and the last pass was calculated using Whittaker reconstruction mode. Note that even though those high-order schemes increased the vector calculation time by more than 200%, they have proven to be more accurate in a test case made in order to find the best correlation scheme for a shear layer. (In the test experiment PIV measurements were compared to a pitot tube measurement inside a flat-plate boundary layer). Each calculated vector was validated against its eight neighbouring vectors before being used, using a four-pass regional median filter. Once the spurious vectors were removed, empty spaces were filled using iterative interpolation of the neighbouring vectors. And finally, a $3 \times 3$ smoothing function was used to reduce noise.

Further details about the software and the vector calculation process can be found in LaVision's FlowMaster manual.

## 4.2 Results and Discussion

### 4.2.1 The Pure Axisymmetric Wake

As was mentioned above, in the present experiments the disc's Reynolds number was 15000. Based on previously reported measurements of far axisymmetric wakes (section 2.1) the wake was expected to be fully developed and to have the high Reynolds number similarity solution in the $z/D > 50$ regime. As a consequence, the current far-wake hot-wire measurements were taken at six different downstream positions ($z/D = 65, 75, 85, 95, 105, 115$) along the wake's axis. In that regime, the wake's local Reynolds number ($Re = U_d l_h/\nu$) remains above 1600, the turbulence Reynolds number ($Re_t = k^2/\epsilon\nu$) stays higher than 480 (at the centre of the wake) and a clear inertial subrange in the energy spectrum exists, as illustrated in figure 4.2. (Note that the clear peaks in those spectra are due to the vortex shedding; further discussion about the vortex shedding can be found in section 4.2.3). Thus, the high Reynolds number solution having $n = 1/3$ would be expected. This would have turbulence stress values at fixed $r/l_h$ varying like $z^{-4/3}$. The maximum values of the three fluctuating (rms) velocities (which were achieved using extrapolation of the point measurements profiles) are plotted in

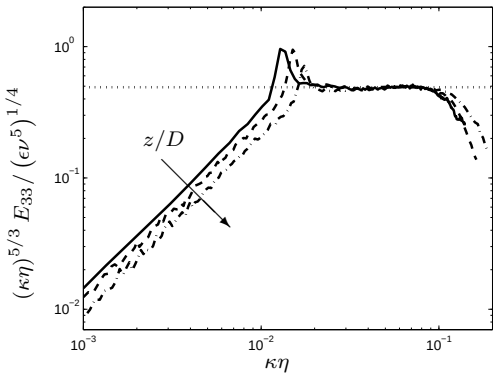


**Figure 4.2:** Example of comparison between the hot-wire one-dimensional energy spectrum, $E_{11}$, measured at about the wake half width and its universal form in the inertial subrange, dotted line. Solid, dashed and dashed-dot lines are the profiles at $z/D = 65, 85$ and 115, respectively.

figure 4.3(a) and it is clear that they demonstrate quite a good fit to the expected behaviour, suggesting a virtual origin of about $z_0/D = -2.7$.

The $n = 1/3$ solution predicts that both $Re$ and $Re_t$ will fall like $z^{-1/3}$. Taking the virtual origin to be $z_0/D = -2.7$ and choosing appropriate amplitudes yields the solid and dashed lines shown in figure 4.3(b). (Note that $Re_t$ was calculated along the axis of the wake). It is clear from that figure that both $Re$ and $Re_t$ behave as expected in the measured region ($65 < z/D < 115$). Moreover, the growth of the wake's half-width, $l_h$, and the decay of its centerline deficit velocity, $U_d$, follow the expected power law as well. Consequently, the self-similar momentum conservation constrain, $U_d l_h^2 =$ constant, is satisfied as well.

Since the combination of the relative size of the deficit velocity in the far wake regime (which was measured to be less than 4.5%) with the hot-wire repeatability error (which was less than 0.2%) gives about 5% scatter in the middle of the wake and even more at its edge a different scaling parameter was needed. Uberoi & Freymuth (1970) suggested dimensional scalings which vary like $z^{-2/3}$ and $z^{1/3}$ for the velocity and length, respectively. However, since the decay rate of the wake in a turbulent stream was not known *á priori*, different scaling parameters were needed in order to be able to evaluate the wake's self-similarity. Because much smaller scatter was noticed in the normal stress profiles and since self-similarity requires $u'_{z_{max}}$ to vary like the deficit velocity and always be found at the same $r/l_h$ location, $u'_{z_{max}}$ and its $r/l_h$ location, $r_{ref}$, were found to be more appropriate choices for the velocity and length scaling parameters. An example of the difference in the scatter between the mean deficit velocity measurements and the axial fluctuating velocity measurements is presented in figure 4.4.

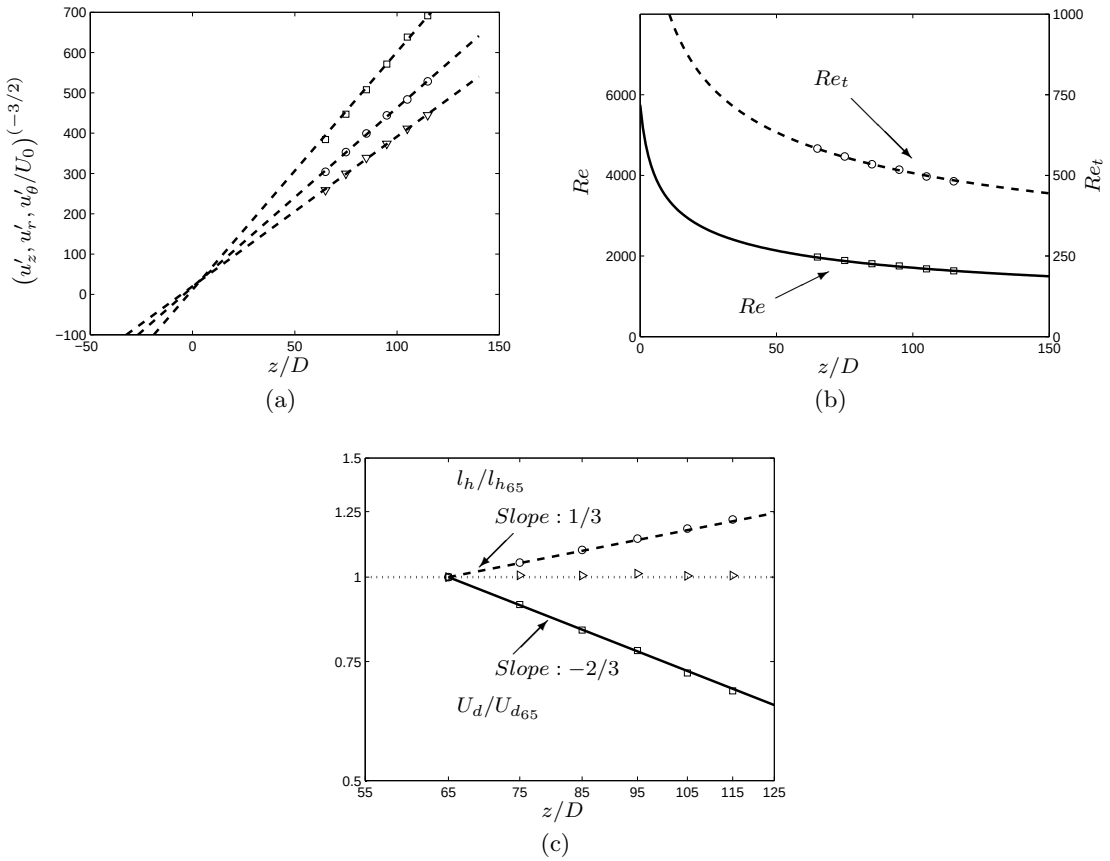


**Figure 4.3:** (a) Variations of the maximum rms velocities with $z/D$; ($\triangledown$) $u_z'$, ($\square$) $u_r'$, ($\circ$) $u_\theta'$ and the dashed lines are linear fits to $u_z'$,$u_r'$ and $u_\theta'$ (b) Variations of $Re$ and $Re_t$ with $z/D$. (c) Variation of wake half-width ($\circ$), maximum deficit velocity ($\triangle$) and $U_d l_h^2/(U_d l_h^2)_{65}$ ($\triangleright$) with time, where subscript 65 means at $z/D = 65$.

The solid line shown in figure 4.4(a) was obtained by assuming similarity – by collapsing/averaging the normalised deficit velocity point measurements at the different $z/D$ locations into one profile – and it fits quite reasonably to the cosinusoidal variation suggested by Ostowari & Page (1989) (which is the dashed line in that figure). Nevertheless, and as was mentioned earlier, there is no fundamental reason for a cosinusoidal or any other unique velocity variation. The self-similar turbulence profiles were also calculated using the same scaling and are shown in figure 4.4(b). They agree qualitatively with previously reported data (for example Uberoi & Freymuth, 1970) but, quantitative agreement is not expected since different initial conditions generally produce different profiles (see Bevilaqua & Lykoudis, 1978 and Redford *et al.*, in preparation, for example). However it should be mentioned that the current results are quantitatively much more similar to the ones reported by Uberoi & Freymuth (1970) (which are presented in figure 3.8(b)) than the DNS results. Nevertheless, the reader should remember that the DNS results were found to be quite comparable to a wake behind a porous disc which explains why the dimensionless turbulence levels there were

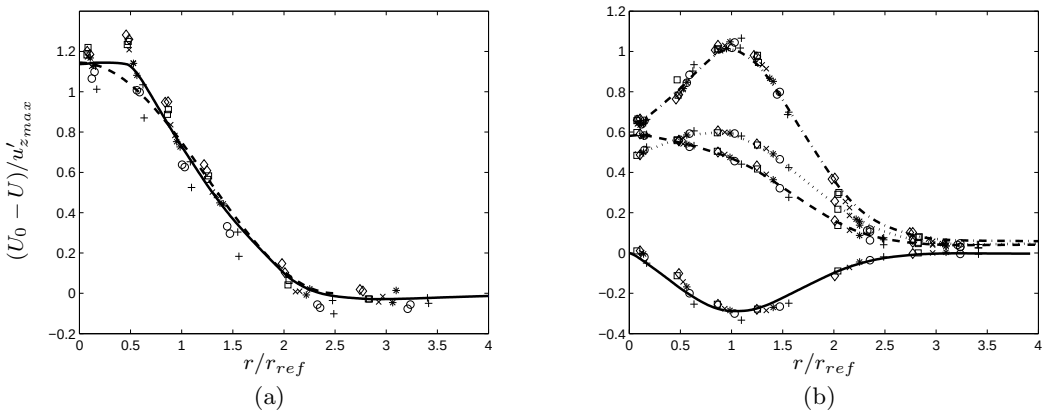


**Figure 4.4:** (a) Dependence of the normalised velocity deficit profiles, $(U_0 - U)/u'_{z_{max}}$, on $z/D$; Solid line Curve fitting interpolation, dashed line Ostowari & Page's (1989) cosinusoidal variation and (+),(∘),(∗),(×),(□) and (◊) are measured data at $z/D = 65, 75, 85, 95, 105, 115$ respectively. (b) Profiles of the dimensionless turbulent velocity fluctuations in the self-similar wake; Solid line $\overline{u_z u_r}/u'^2_{z_{max}}$, dashed line $\overline{u_\theta u_\theta}/u'^2_{z_{max}}$, dotted line $\overline{u_r u_r}/u'^2_{z_{max}}$, dashed-dot line $\overline{u_z u_z}/u'^2_{z_{max}}$ and (+), (∘), (∗), (×), (□) and (◊) are measured $\overline{u_z u_z}/u'^2_{z_{max}}$ data at $z/D = 65, 75, 85, 95, 105, 115$ respectively.

about an order of magnitude lower than in the current measurements behind a solid disc.

One way to evaluate the accuracy of the above self-similar profiles (or the validity of the theoretical study; see Section 2.1.1) is to look at the relationship between the mean velocity deficit and the turbulent shear stress non-dimensional self-similar profiles which can be easily derived using Equation 2.25 and the fact that the product $U_d \times l^2$ is constant (shown in detail in Appendix A). As can be seen in figure 4.5(a) the measured turbulent shear stress and the one deduced from the mean velocity profile only satisfactorily agree in trend but with values deviating by less than about 15%. However, since the derived expression (see Appendix A) makes some simplifications to the governing equations (for example the neglectable pressure gradient; see section 2.1.1) and the self-similar mean velocity profile contains errors due to scatter (which was noticed to affect the calculated profile, excessively, when differentiated), the calculated profile is not expected to agree precisely with the measured one so that the current agreement does actually give confidence in the results.

Once all the wake's properties were extracted, the TKE balance was calculated using Equation 4.9. Note that in this equation the boundary-layer approximation has been used and that the convection term is expressed in terms of $r/r_{ref}$ using self-similarity (see Appendix B). While the production and the convection terms were calculated directly from the measured self-similar profiles, the dissipation was extracted from the local energy spectrum using the energy spectrum's universal form and Taylor's hypothesis. Note that since the turbulence levels in the far wake are relatively small (only a few percent) Taylor's hypothesis can be

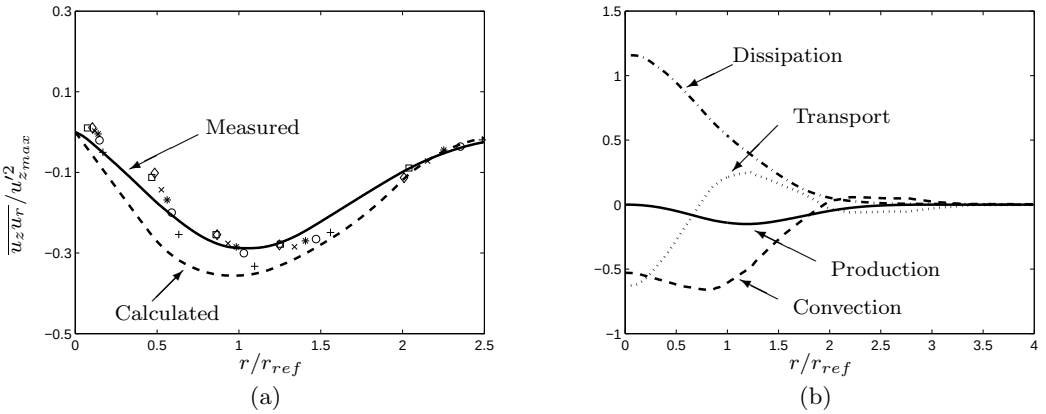


**Figure 4.5:** (a) Comparison between the measured turbulent shear stress profile and the one extrapolated from the mean velocity profile. (+), (∘), (∗), (×), (□) and (◊) are measured $\overline{u_z u_z}/u'^2_{z_{max}}$ data at $z/D = 65, 75, 85, 95, 105, 115$ respectively.(b) The non-dimensional turbulent kinetic energy budget of the self similar wake.

used (Pope, 2000). The transport term was calculated from the balance since the fluctuating pressure and some of the triple product terms were not measured. (This was also done by Uberoi & Freymuth, 1970, for example). Since the balancing transport term should integrate to zero across the wake, the dissipation rate (which is assumed to contain the largest source of error) was factored by about 1.04 (e.g. $\epsilon = 1.04\epsilon_{in}$, where $\epsilon_{in}$ is the dissipation rate deduced from the spectrum) to ensure that. Figure 4.5(b) shows the resulting TKE balance, which qualitatively agrees with previously reported TKE balances of such wakes (e.g. Uberoi & Freymuth, 1970).

$$
\begin{aligned}
\textbf{Convection}: \quad & -\frac{r}{6r_{ref}}\frac{\partial}{\partial\left(r/r_{ref}\right)}\left(\frac{\overline{u_r^2}+\overline{u_\theta^2}+\overline{u_z^2}}{u'^2_{z_{max}}}\right)-\frac{2}{3}\left(\frac{\overline{u_r^2}+\overline{u_\theta^2}+\overline{u_z^2}}{u'^2_{z_{max}}}\right) \\
\textbf{Transport}: \quad & +\frac{1}{r/r_{ref}}\frac{\partial}{\partial\left(r/r_{ref}\right)}\left\{\frac{r}{r_{ref}}\overline{u_r\left[\frac{p}{\rho}+\frac{\frac{1}{2}\left(u_r^2+u_\theta^2+u_z^2\right)}{u'^3_{z_{max}}}\right]}\right\} \\
\textbf{Production}: \quad & -\frac{\overline{u_z u_r}}{u'^2_{z_{max}}}\frac{\partial}{\partial\left(r/r_{ref}\right)}\left(\frac{U_0-U_z}{u'_{z_{max}}}\right) \\
\textbf{Dissipation}: \quad & +\epsilon = 0
\end{aligned}
\tag{4.9}
$$

In summary, based on the wake's measured properties, the wake's local Reynolds number (in the measured regime, $65 < z/D < 115$) varies between 2000 to 1600 and its turbulent Reynolds number varies between 600 to 480. In addition, as expected, the wake in that regime is self-similar with $n = 1/3$ and its mean velocity, turbulent stresses and TKE profiles agree with those previously reported.

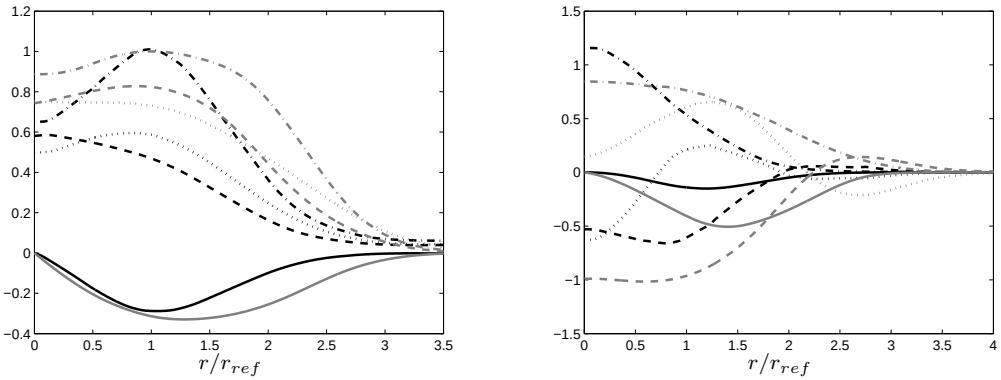


**Figure 4.6:** (a) Comparison between the various dimensionless Reynolds stress profiles of the self-similar wakes measured in the wind tunnel (black) and in the DNS (grey); Solid line $\overline{u_z u_r}/u'^2_{z_{max}}$, dashed line $\overline{u_\theta u_\theta}/u'^2_{z_{max}}$, dotted line $\overline{u_r u_r}/u'^2_{z_{max}}$ and dashed-dot line $\overline{u_z u_z}/u'^2_{z_{max}}$. (b) Comparison between the various non-dimensional (using $u'_{z_{max}}$ and $r_{ref}$) TKE balance profiles of the self-similar wakes measured in the wind tunnel (black) and in the DNS (grey); Solid, dashed, dashed-dot and dotted lines are production, convection for the experiments and rate of change for the DNS, dissipation and transport respectively.

### Self-Similar Wake – Wind tunnel vs. DNS

Before presenting the rest of the wind tunnel measurements, it would be wise to discuss first some of the similarities and differences between the self-similar wakes created in the wind tunnel and by the DNS, especially since different initial conditions generally produce different profiles (e.g. Bevilaqua & Lykoudis, 1978; Redford *et al.*, in preparation).

The two wakes were found to be fully self-similar with centre deficit velocity and wake half-width developing with the same power laws, with $n = 1/3$ as theory predicts. Yet, when the various non-dimensional turbulent stress profiles are compared it was found that they are not identical but only qualitatively similar, as illustrated in figure 4.6(a). The wake generated by the DNS has higher (dimensionless) turbulence levels at its edge region and the ratios $u'_z/u'_r$ and $u'_z/u'_\theta$ across that wake are closer to one but with a minimum (dimensionless) turbulent shear stress similar to the wake generated in the wind tunnel. When the TKE balances were compared between the two wakes they were found to be different as well (as was expected from the previous finding) as is illustrated in figure 4.6(b). It was found that while the two wakes have the same minimum (dimensionless) turbulent shear stress the turbulent production rate in the DNS is much higher. Moreover, the wake generated by the DNS has lower dissipation rate and higher rate of change. Last, the ratios between the maximum production to the maximums of the other terms were found to be different as well. While for the DNS wake they are of $O(1)$ (which is of the same order one of the cases Redford *et al.*, in preparation,

| Grid | Case | Rod shape | $M[mm]$ | $d/M$ | $u'_{ze}/U_0[\%]$ | $L_{11}/D$ | $\lambda/D$ | $Re_\lambda$ |
|---|---|---|---|---|---|---|---|---|
| A | 1 | Square | 23.5 | 0.27 | 4.3 | 11 | 0.21 | 138 |
| A | 2 | Square | 23.5 | 0.27 | 3.7 | 12.9 | 0.23 | 137 |
| A | 3 | Square | 23.5 | 0.27 | 3.3 | 13.7 | 0.25 | 134 |
| B | 4 | Round | 11.07 | 0.15 | 2.1 | 3.1 | 0.15 | 50 |
| B | 5 | Round | 11.07 | 0.15 | 1.2 | 4.8 | 0.24 | 44 |
| B | 6 | Round | 11.07 | 0.15 | 0.8 | 4.8 | 0.32 | 43 |

**Table 4.1:** The defining parameters of the different turbulent streams at $z/D = 0$.

reported), for the wake generated in the wind tunnel they are of $O(0.1 - 0.25)$ (which is of the same order Uberoi & Freymuth, 1970, had reported for their wake), suggesting that the TKE inside the DNS wake is approximately dissipated (around the wake half-width) at the same rate it is produced, while for the wind tunnel wake it is dissipated much quicker than it is produced.

To conclude, the two wakes are self-similar with similar mean-flow power law decay rates. However, while the two share the same decay rate, the structure and development of the turbulence inside them is different (as was expected). Nevertheless, the fact that both wakes show similarities to previously reported far axisymmetric wakes gives confidence in generating such wakes using both techniques.

### 4.2.2 The Turbulent Streams

For this study two different bi-planar grids were used to generate the turbulent streams. Each grid was located at three different positions upstream of the disc's location, $z/D = 0$. Thus, the wake was influenced by six different turbulent streams, such that each had different turbulence parameters at $z/D = 0$, all presented in table 4.1. Note that the length scales in table 4.1 were evaluated from the energy spectrum, presented in figure 4.7(a), using Taylor's hypothesis. The integral length scale and Taylor's microscale were evaluated using: $L_{11} = \pi E_{11}(\kappa = 0)/2\overline{u^2}$ and $\lambda = \sqrt{15\nu\overline{u^2}/\epsilon}$ respectively, where $\epsilon$ was estimated using the spectrum's universal shape in the inertial subrange, $E_{11} = 27/55\epsilon^{2/3}\kappa^{-5/3}$ (Pope, 2000).

The decay rate exponent of each of the grids was found by fitting the measured velocity fluctuations into the following expression: $\overline{u^2}/U_0^2 = B\,(z/M - z_0/M)^{-n}$, where $B$ is a constant and $z_0$ is the grid's false origin. Figure 4.7(b) shows that the two flows decay slightly differently (as was previously reported by many researchers, see section 2.2.2). Krogstad & Davidson's (2010) study on grid turbulence suggests that grid turbulence is more Saffman-like

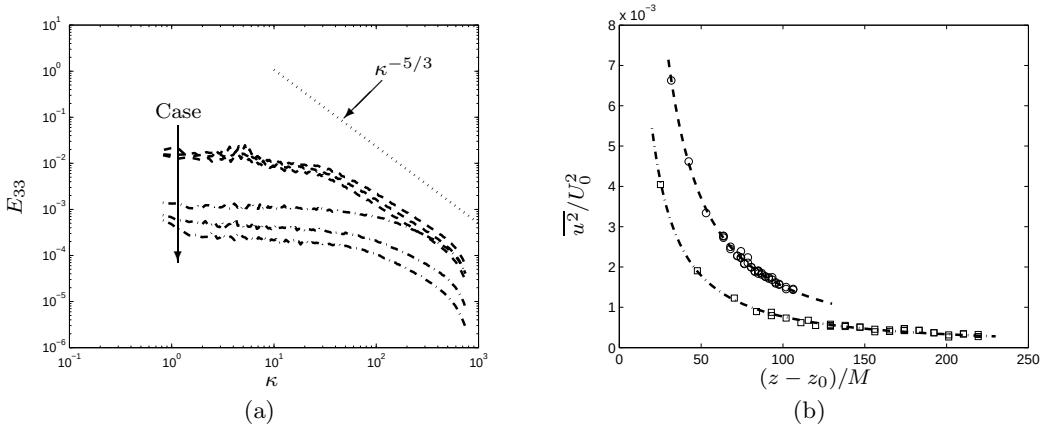


**Figure 4.7:** (a) Energy spectrum of each of the grid turbulence cases at $z/D = 0$. (b) Grid turbulence decay; (○) grid A's data factored by 3, (□) grid B's data factored by 10 and the lines are the corresponding best fits with $n = 1.28, 1.22$.

with $n = 1.2\,(1 - q)$, where $q \ll 1$ and rises from a slow fall in $A$, in equation (3.11), with $z$. The current fits to the measurements do not seem to be consistent with their power exponent. However, Saffman's turbulence requires that $\overline{u^2}L_{11}^3 = const$ which in the current measurements is better satisfied than Batchelor's requirement that $\overline{u^2}L_{11}^5 = const$, as illustrated in figure 4.8(a). In addition, the fact that $A$ falls slightly with $z/D$, as illustrated in figure 4.8(b), suggests that $n$ should be lower than 1.2, as Krogstad & Davidson (2010) suggested. Thus, it is believed that a greater $z/D$ range is required, especially more data points in the $z/M > 50$ regime (as was also suggested by Krogstad & Davidson, 2010), before $n$ can be determined precisely and that the current grids produce turbulence which is, nevertheless, Saffman-like. (Notice that $n$ is about 5% closer to 1.2 for grid B, where a much larger $z/M$ regime was used, in comparison to grid A).

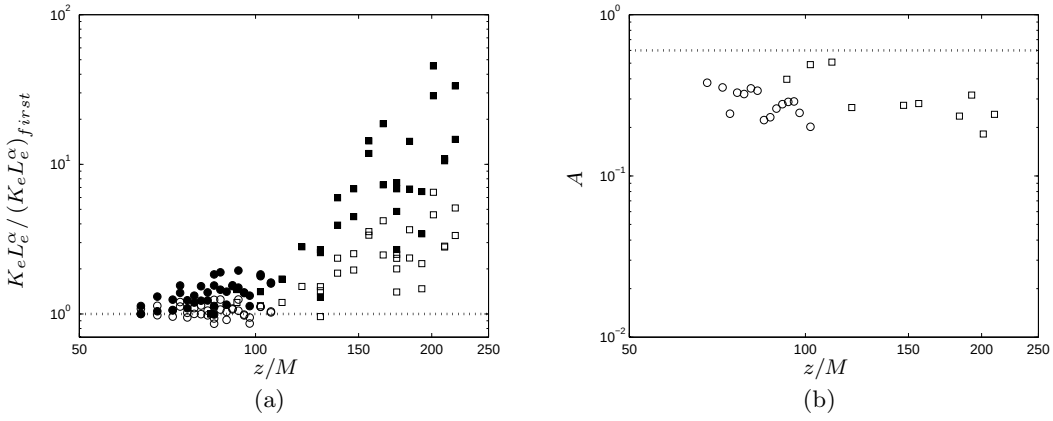


**Figure 4.8:** (a) Saffman and Batchelor's turbulence constrains; Free-stream turbulence generated by grid A (○) and grid B (□). Open symbols $\alpha = 3$, Closed symbols $\alpha = 5$ and $(K_e L_e^\alpha)_{first}$ refers to the least downstream point measured. (b) Variations of $A$ with $z/M$; Free-stream turbulence generated by grid A (○) and grid B (□)

In summary, the two bi-planner grids generate turbulent streams. Those streams show consistency and agreement with previously reported grid turbulence studies by being Saffman-like and in their decay rate exponent.

**Free-Stream Turbulence – Wind tunnel vs. DNS**

Before presenting further results, the author would like to highlight some of the differences and similarities between the external turbulent fields generated in the wind tunnel and in the DNS.

Both in the wind tunnel and in the DNS the turbulence that was created is Saffman-like quasi-HIT, where all fields share about the same power law decay rate with $n \approx 1.2$. As for the turbulence levels, in the wind tunnel relatively lower turbulence levels were achieved (with $43 < Re_\lambda < 138$), where the strongest free-stream turbulence generated in the wind tunnel is of the same order as the weakest one generated in the DNS. (Recall that in the DNS $133 < Re_\lambda < 314$). On the other hand, while higher turbulence levels would be expected to contain a larger range of length scales (for example it would be expected that the ratio $L_{ze}/\lambda_{ze}$ would be higher), it was found that that ratio is much larger for the weaker turbulence generated in the wind tunnel than for the stronger turbulence generated in the DNS. That unexpected result was found to be associated with the limited size of the computational domain (due to limited computational resources) which limited the size the largest length scales could reach. Nevertheless, since such a problem was noticed in the the energy spectra of many previous publications of forced HIT using DNS (see Jimenez *et al.*, 1993, for example) and was not reported to affect the turbulent structure dramatically it was ignored here.

To conclude, all the turbulent fields generated both in the wind tunnel and in the DNS are quasi HIT Saffman-like and they all agree with previous reports on HIT turbulence. Note that a full comparison between the external turbulence to the wind tunnel pure wake at a certain $z/D$ was not done since it is not appropriate, as will be revealed below.

### 4.2.3 Wakes in Turbulent Streams

Once both the wake and turbulent streams were created and showed consistency with previous work they were combined such that the wake was created in the different turbulent streams

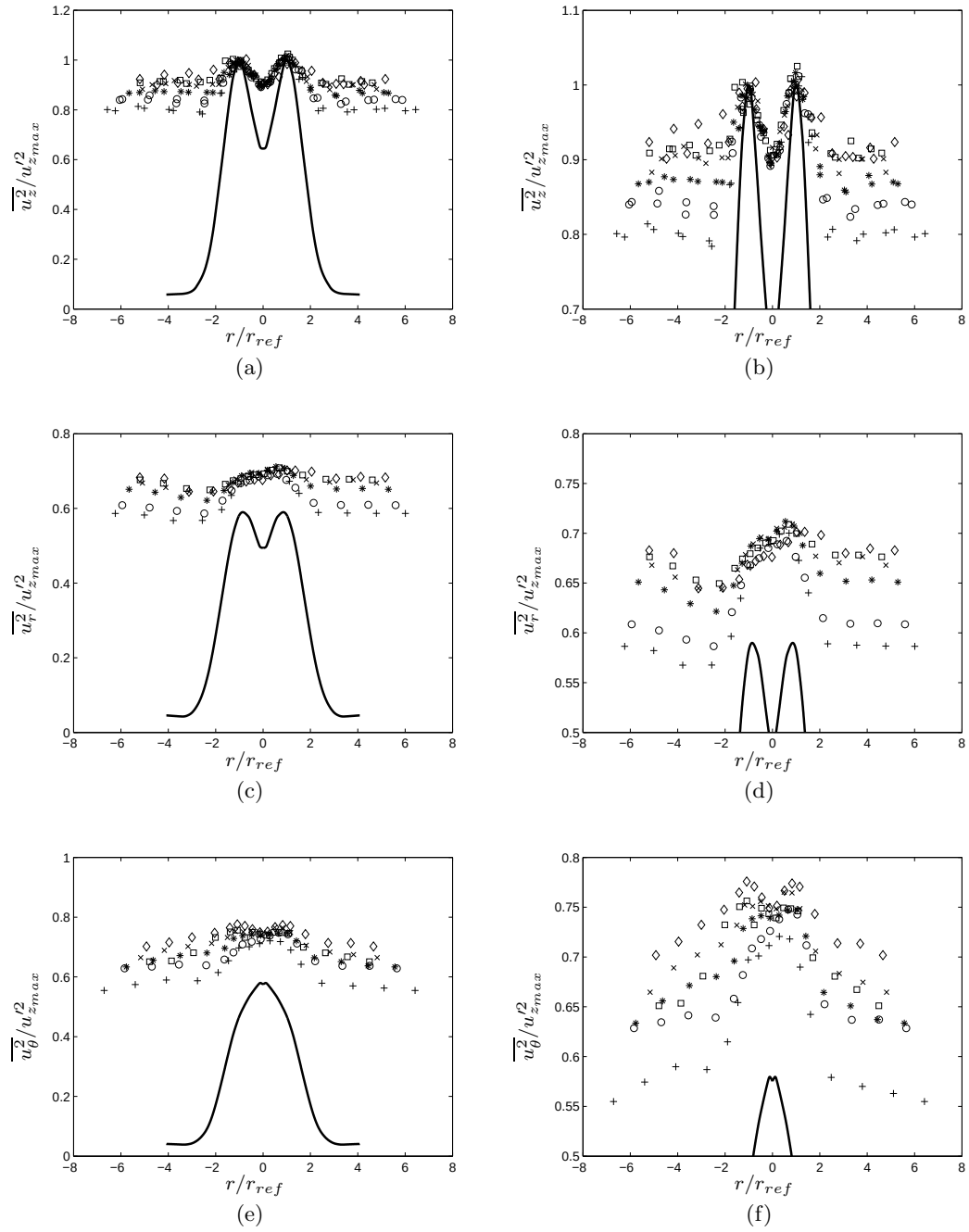


**Figure 4.9:** Profiles of the dimensionless normal turbulent velocity fluctuations across the wake for case one, where profiles on the right are expended versions of the profiles on the left. Solid line is the self-similar profile for the pure wake case and (+), (∘), (∗), (×), (□) and (◊) are case one measurements at $z/D = 65, 75, 85, 95, 105, 115$ respectively.

by placing the disc, the wake generating body, in the wake of the grids. Recall that two different grids were used and that each grid was placed at three different locations upstream of the disc (section 4.2.2). Profile measurements were taken at $z/D = 65, 75, 85, 95, 105, 115$ as for the pure wake case and are compared to the pure wake case below.

First to be examined was the axial turbulent stress, $u_z'$. Recall that for the pure wake

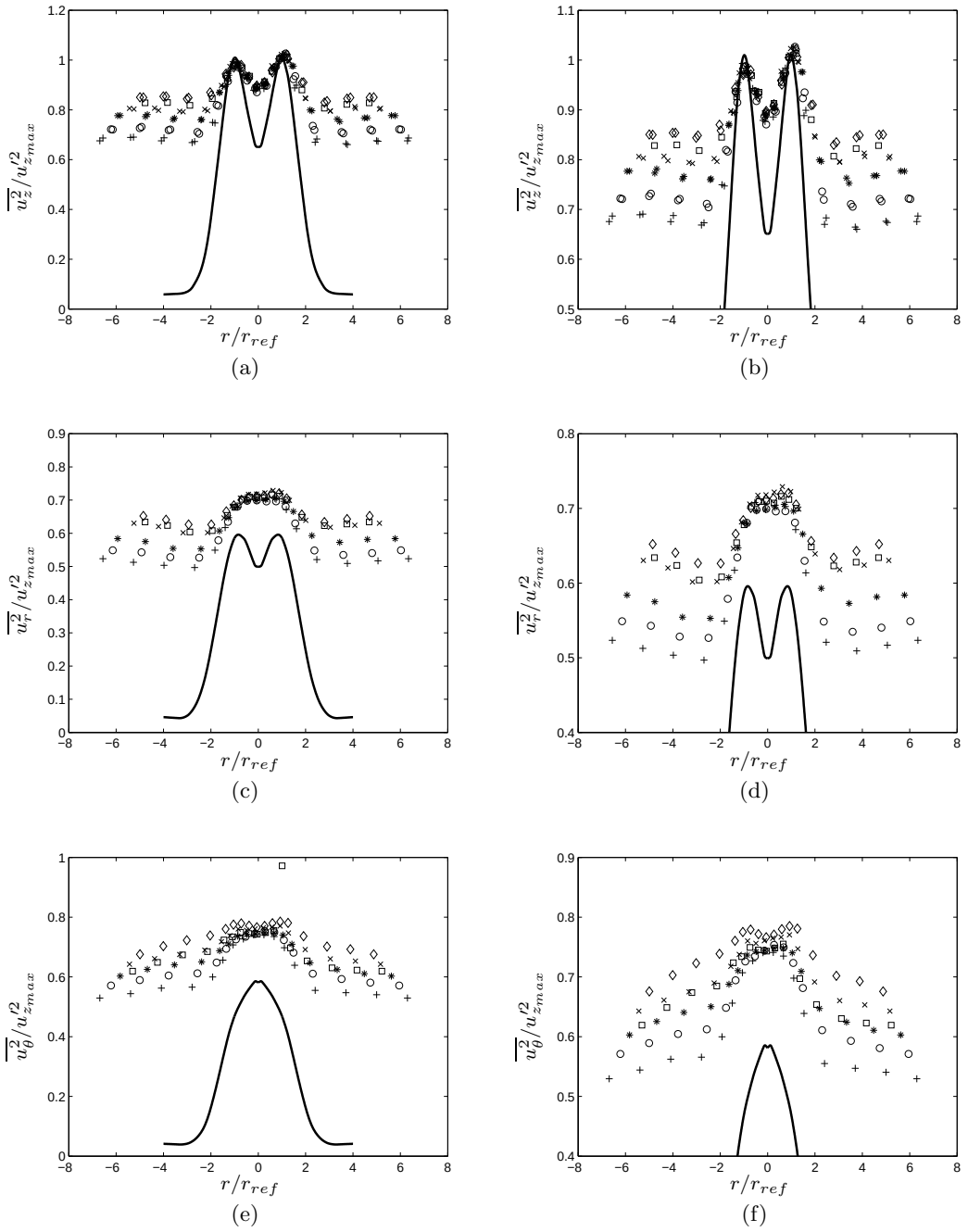


**Figure 4.10:** Profiles of the dimensionless normal turbulent velocity fluctuations across the wake for case three, where profiles on the right are expended versions of the profiles on the left. Solid line is the self-similar profile for the pure wake case and (+), (∘), (∗), (×), (□) and (◇) are case three measurements at $z/D = 65, 75, 85, 95, 105, 115$ respectively.

study $u'_{z_{max}}$ and $r_{ref} = r\left(u' = u'_{z_{max}}\right)$ were used as the wake characteristic velocity and length scales respectively (section 4.2.1) and so we examine these first. The results show that the classical self-similar behaviour (where the mean velocity and all the turbulent stresses decay at the same rate across the whole wake) no longer exists. Now, on the other hand, the axial turbulent stress, $u'_z$, decays differently in two distinct regimes across the wake. In the middle part of the wake, $u'_z$ decays at one rate while at the edge of the wake it decays

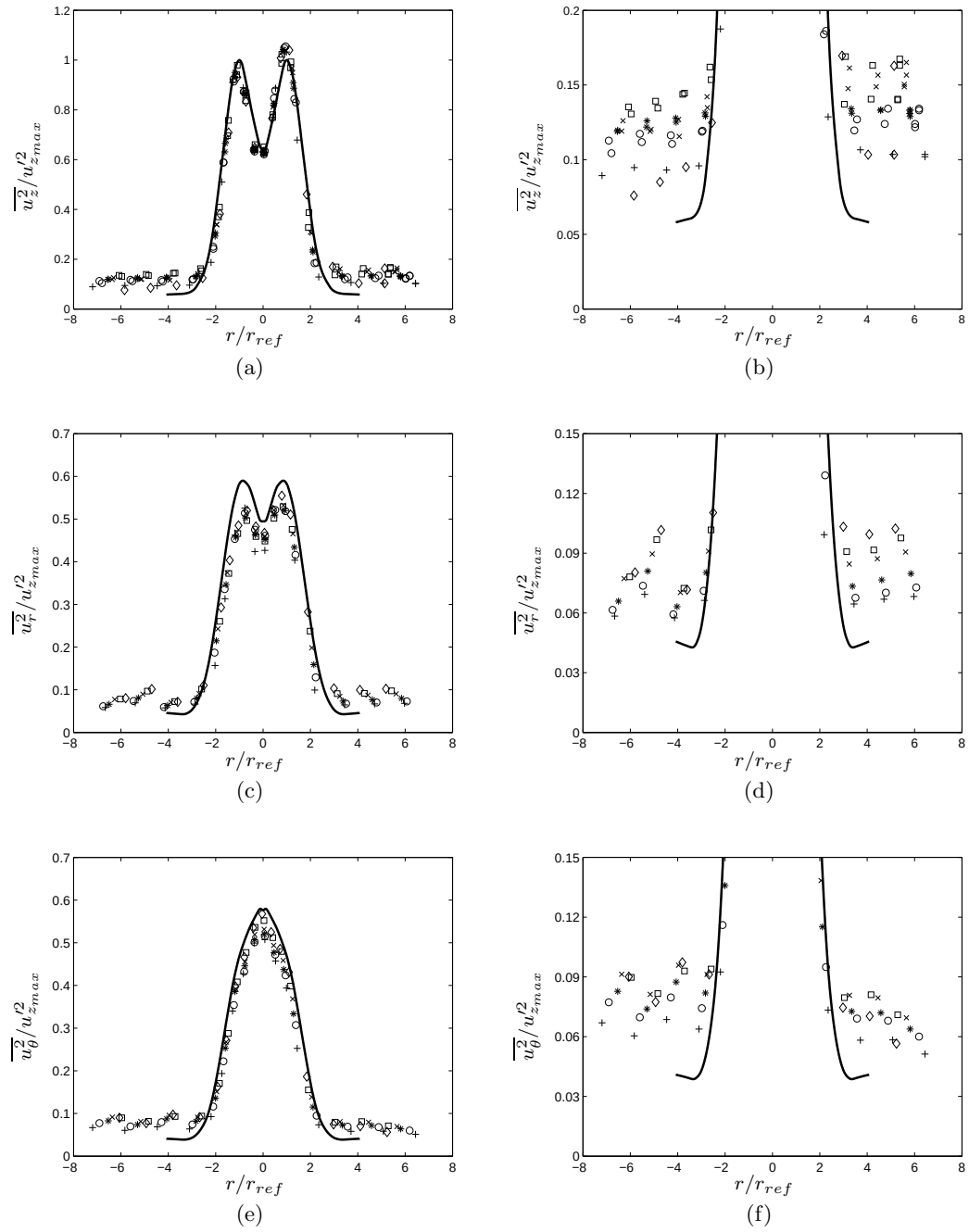


**Figure 4.11:** Profiles of the dimensionless normal turbulent velocity fluctuations across the wake for case five, where profiles on the right are expended versions of the profiles on the left. Solid line is the self-similar profile for the pure wake case and (+), (∘), (∗), (×), (□) and (◊) are case five measurements at $z/D = 65, 75, 85, 95, 105, 115$ respectively.

at a rate similar to the one for the turbulent stream. Those two regimes are separated by a narrow transition regime which moves inwards with distance downstream. In addition, the two decaying regimes were also noticed for the radial and the angular turbulent stresses, $u'_r$ and $u'_\theta$, respectively. Moreover, for these two turbulent stresses, the inner regime decays at the same rate as $u'_{z_{max}}$ and the narrow transition regime moves inwards with distance downstream, as was also noticed in the axial turbulent stress profiles. Figures 4.9, 4.10 and

4.11 show examples of that behaviour for cases one, three and five respectively. Notice in these figures that the turbulence in the wake inner part decays quicker than the free-stream turbulence does, behaviour that was also noticed in the other three cases. Thus, further downstream $u'_{ze}$ would reach the point where it is equal to $u'_{z_{max}}$, $u'_{r_{max}}$ and $u'_{\theta_{max}}$. That point was unfortunately never reached, since in all cases the free-stream's turbulence levels were not high enough (in comparison with $u'_{z_{max}}$) over the measured regime, $65 \leq z/D \leq 115$. Note that further downstream measurements were not pursued due to the large size of the wake relatively to the test section's width.

In addition, figures 4.9, 4.10 and 4.11 also suggest that the turbulence inside the wake becomes more isotropic (based on the simple measure $u'_1/u'_2$) with an increase in the ratio $u'_{ze}/U_0$. Thus, the turbulence inside the wake becomes more similar to that in the free-stream. Remember that grid turbulence is very similar to HIT (as was discussed in section 2.2.2) and note as well that measurements for the current grids showed that $u'_1/u'_2 \approx 1.1 - 1.2$. In addition, it was noticed that the turbulence shear stress peak values are reduced with an increase in the ratio $u'_{ze}/U_0$, which further strengthens the statement that the turbulence inside the wake develops to become more like that in the free-stream (HIT in the current experiments) when the ratio $u'_{ze}/U_0$ increases. Figure 4.12(a) illustrates a summary of all those findings for all cases. Note however that the shape of the turbulence shear stress profile (where examples for cases one, three and five are illustrated in figures 4.12(b), (c) and (d), respectively) suggests that it is still driven by the mean shear and so would only fully cease to exist when the mean shear (or in other words the wake) does. Thus, the turbulence inside the wake could never fully be similar to that in the free-stream (for example HIT, like the grid turbulence in the current experiments), even at the limit $u'_{ze}/U_0 \to \infty$, but could only approach to it to within a certain limit.

Since in the central part of the wake the various turbulent stresses seem to decay at the same rate, it is of interest to know what that rate is. In all previous studies of axisymmetric wakes in turbulent streams it was noticed that the wake's decay rate is changed. Yet, it is not clear to what rate, since different researchers have reported on different decay rates. In the current measurements $u'_{z_{max}}$ varies as in the pure wake case (as $z^{-2/3}$); Figure 4.13 illustrates that behaviour, where for comparison the free-stream turbulence decay in all turbulent cases are presented in figures 4.13(c) and 4.13(d). Notice that the main distinguishing differences between the various cases are the wakes' false origins, $z_0$, and the constant, $A$, in the following

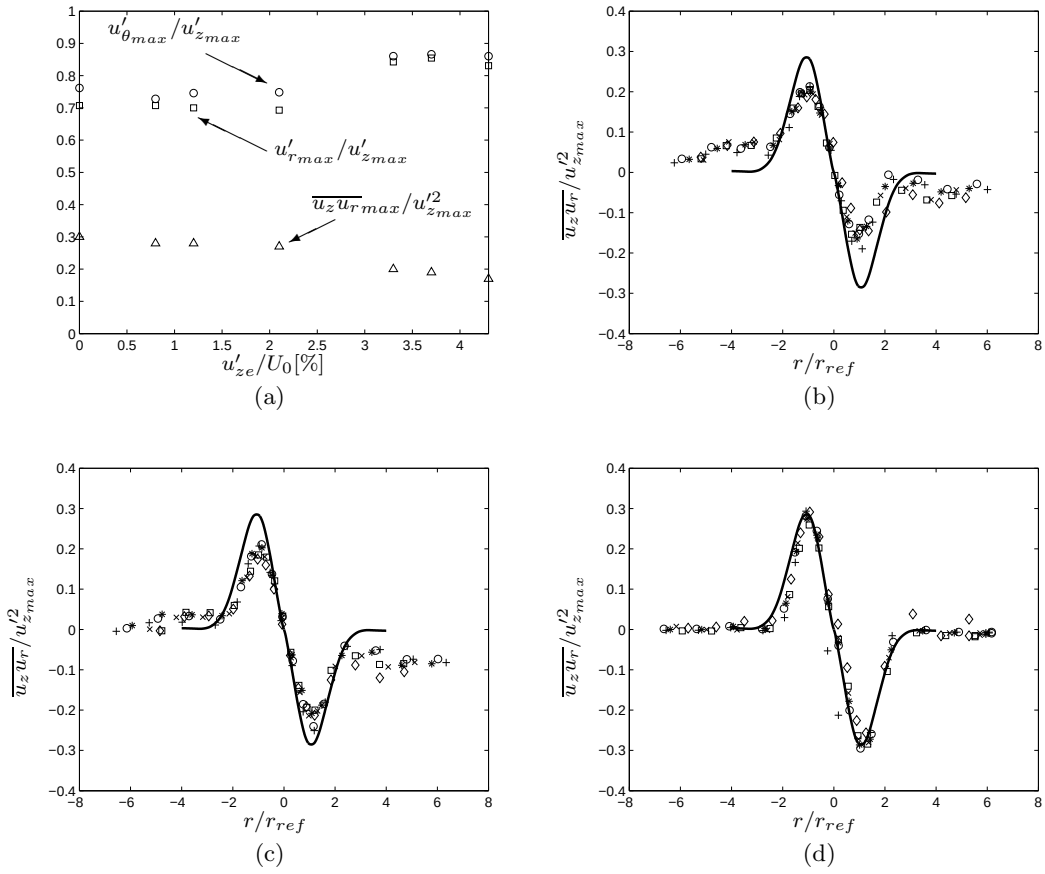


**Figure 4.12:** (a) The ratio between the various turbulence stresses at $z/D = 65$. (b), (c) and (d) are profiles of the dimensionless normal turbulent velocity fluctuations across the wake for cases one, three and five, respectively; Solid line is the profile for the pure wake case and (+), (○), (∗), (×), (□) and (◊) are measurements at $z/D = 65, 75, 85, 95, 105, 115$ respectively.

equation,

$$\frac{u'_{z_{max}}}{U_0} = A\,(z - z_0)^{-n}\,. \tag{4.10}$$

Those variations are not a surprise since both the false origin and the coefficient are functions of the initial conditions. However, the current measurements suggest that the false origin varies with the different cases while the constant only varies with the different grids. As clearly evident in table 4.13(e), grid A generates integral length scales which are about three to four times larger at $z/D = 0$ than the integral length scales created by grid B there. And so, one might assume that the coefficient $A$ in equation (4.10) is mainly influenced by the ratio $L_{11}/D$ at $z/D = 0$. However, since (1) the constant does not seem to be affected very significantly by the variations in the integral length scale between the three cases of each grid at $z/D = 0$, (2) at $z/D = 85$ $L_{11}/2r_{ref}$ is of order one in all six cases (see table 4.13(e)) and (3) the turbulence levels inside the wake does not seem to be affected significantly by

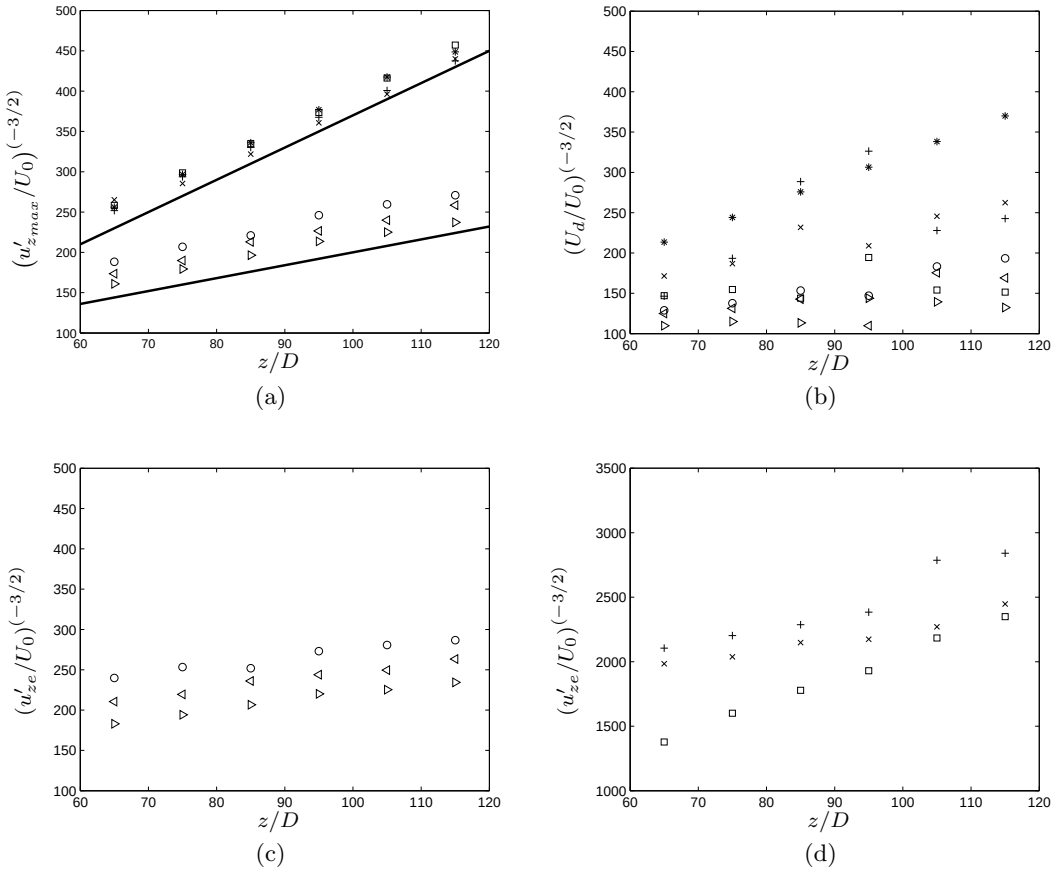


| Grid | Case | Symbol | $u'_{ze}/U_0\|_{z/D=0}$ | $L_{11}/D\|_{z/D=0}$ | $u'_{ze}/U_d\|_{z/D=85}$ | $L_{11}/2r_{ref}\|_{z/d=85}$ |
|---|---|---|---|---|---|---|
| A | 1 | $\triangleright$ | 0.043 | 11 | 0.277 | 0.91 |
| A | 2 | $\triangleleft$ | 0.037 | 12.9 | 0.283 | 0.9 |
| A | 3 | $\circ$ | 0.033 | 13.7 | 0.245 | 0.84 |
| B | 4 | $\square$ | 0.021 | 3.1 | 0.408 | 0.91 |
| B | 5 | $\times$ | 0.012 | 4.8 | 0.413 | 0.97 |
| B | 6 | $+$ | 0.008 | 4.8 | 0.427 | 0.94 |

(e)

**Figure 4.13:** (a) and (b) Variations of $u'_{z_{max}}$ and $U_d$ with $z/D$, respectively; ($\triangleright$) case one, ($\triangleleft$) case two, ($\circ$) case three, ($\square$) case four, ($\times$) case five, ($+$) case six, ($*$) pure wake and the solid lines are linear slope examples. (c) and (d) are variations of $u'_{ze}$ with $z/D$ in grid A and B, respectively, where the symbols are similar to (a). (e) The defining parameters of the different turbulent streams at $z/D = 0$ and 85. (Note that $2r_{ref}$ was used instead of $l_h$ due high scatter in $l_h$, as was explained above).

the presence of the free-stream turbulence in cases four, five and six, the author believes that that coefficient is actually only influenced by the free-stream turbulence dimensional decay (i.e. not only its decay rate but its actual decay) which is the only parameter of the free-stream turbulence that was kept the same between the two groups of three turbulent streams generated by the two grids. On the other hand, while the coefficient did only vary with the different grids, the false origin varied with the different cases suggesting that it was influenced in addition to the free-stream turbulence decay, by the other various turbulence parameters,

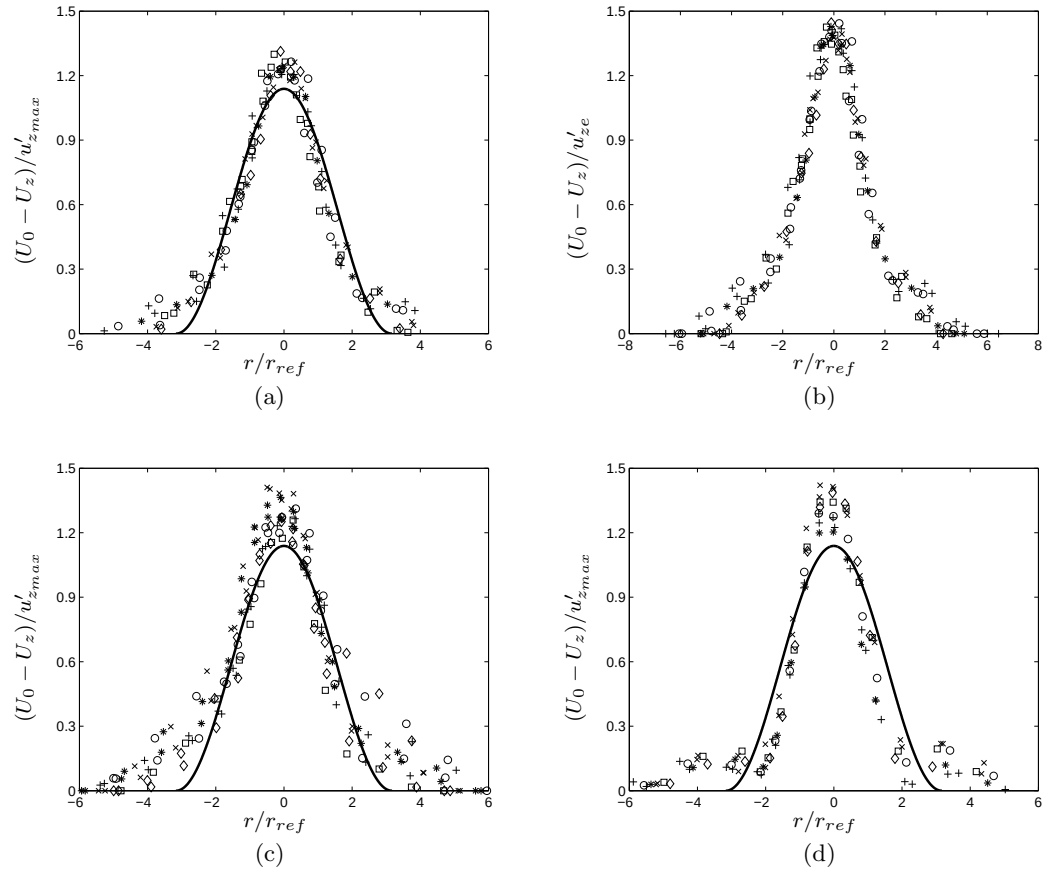


**Figure 4.14:** (a), (c) and (d) are examples of the scaling of the mean deficit velocity profile with $u'_{z_{max}}$ for cases one, three and five respectively and all compared with the pure wake case (solid line) and (b) is an example of the scaling of the mean deficit velocity profile with $u'_{ze}$ for case one; (+), (∘), (∗), (×), (□) and (◊) are the appropriate measurements at $z/D = 65, 75, 85, 95, 105, 115$ respectively.

like the free-stream turbulence intensity level and length scales, for example. In addition, unlike the pure wake case where the mean and fluctuating velocity parameters decay at the same rate, the mean deficit velocity decayed at about the same rate as $u'_{z_{max}}$ only in cases five and six. In the other four cases, the mean wake was noticed to be decaying slightly slower than $u'_{z_{max}}$. That is clearly noticed when figures 4.13 and 4.13(b) and compared. (Recall that there is about 5% scatter in $U_d$ arising from the repeatability error; see above). In addtion, figures 4.14(a), (c) and (d) illustrate how the mean deficit profile scales with $u'_{z_{max}}$ for cases one, three and five respectively. Note that it was observed that the mean deficit velocity decay rate reduces when $u'_{ze}/U_0$ increases (as can be noticed in figure 4.13(b)) until the point where it seems to have reached the rate at which the turbulence in the free-stream decays in cases one and two. Thus, in those two cases the mean wake decays at about the same rate as the free-stream turbulence does, such that it scales with the local free-stream's rms velocity, as illustrated in figure 4.14(b) for case one. Notice there that when the scatter in the dimensionless centre deficit velocity profiles in figures 4.14(a) and (b) is compared, a

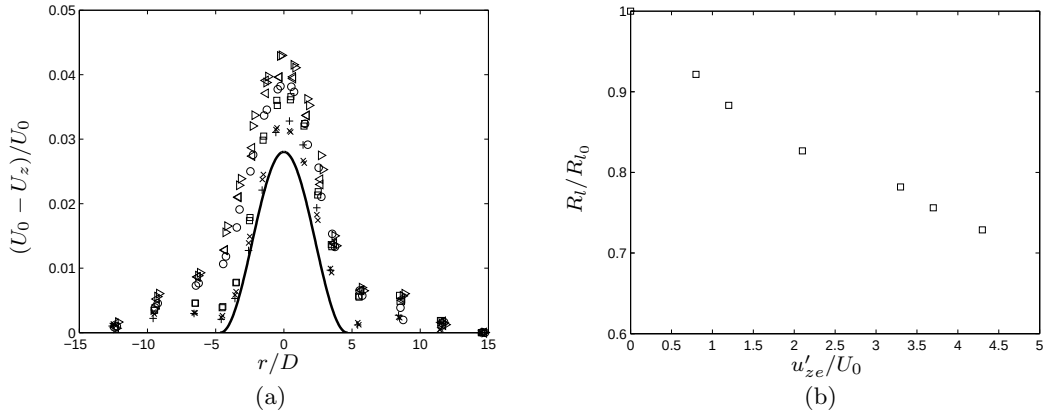


**Figure 4.15:** (a) Comparison of the deficit velocity profiles at $z/D = 65$ for the various cases; Solid line is the pure wake deficit velocity profile and (▷), (◁), (○), (□), (×), (+) are the deficit velocity measurements for cases one, two, three, four, five and six respectively. (b) Variations of the recirculation length, $R_l$, with $u'_{ze}/U_0$, where $R_{l_0}$ is the pure wake recirculation length.

reduction of about 50% is noticed when $u'_{ze}$ is used as the velocity scaling parameter.

Along with the decrease in the decay rate of the centre velocity (since $-n$ becomes less negative), another clear trend is noticed when mean deficit velocity profiles are compared between the various cases at a certain $z/D$. The wake's centre deficit velocity and its width increase as $u'_{ze}/U_0$ increases, as illustrated in figure 4.15(a) for $z/D = 65$. Thus it seems that the disc's drag coefficient is increased due to the presence of the free-stream turbulence. Since the disc's drag coefficient was not measured directly an attempt was made to estimate it using the integral momentum equation. However, it was found that due to the large scatter (arising mainly from the hot-wire measurements) in those estimates it was impossible to notice any clear trend between them. (For example, for the pure wake case the estimate of the drag coefficient varied by about 40% between the different locations downstream and similarly for the various turbulent free-stream cases). Nevertheless, support for the increase in the disc's drag coefficient was found in the near-wake PIV measurements, where it was noticed that the recirculation length decreased (as illustrated in figure 4.15) due to the increased entrainment in the separated shear layer (see section 4.2.4). Recall that it has been found by both Bearman (1965) and Bearman & Trueman (1972) that the nearer to the body the vortices form the lower the base pressure is (and the higher the drag). Note although that while it is reported here that the turbulence in the free-stream appears to increase the drag of the disc, Tyagi (2005) found that the opposite occurs for a sphere. However, there is a fundamental difference between the two experiments. Unlike the fixed separation point at the edge of the disc the separation point around a sphere is not fixed and so in Tyagi's (2005) case the free-stream turbulence acts to delay separation and thus reduces the wake size and

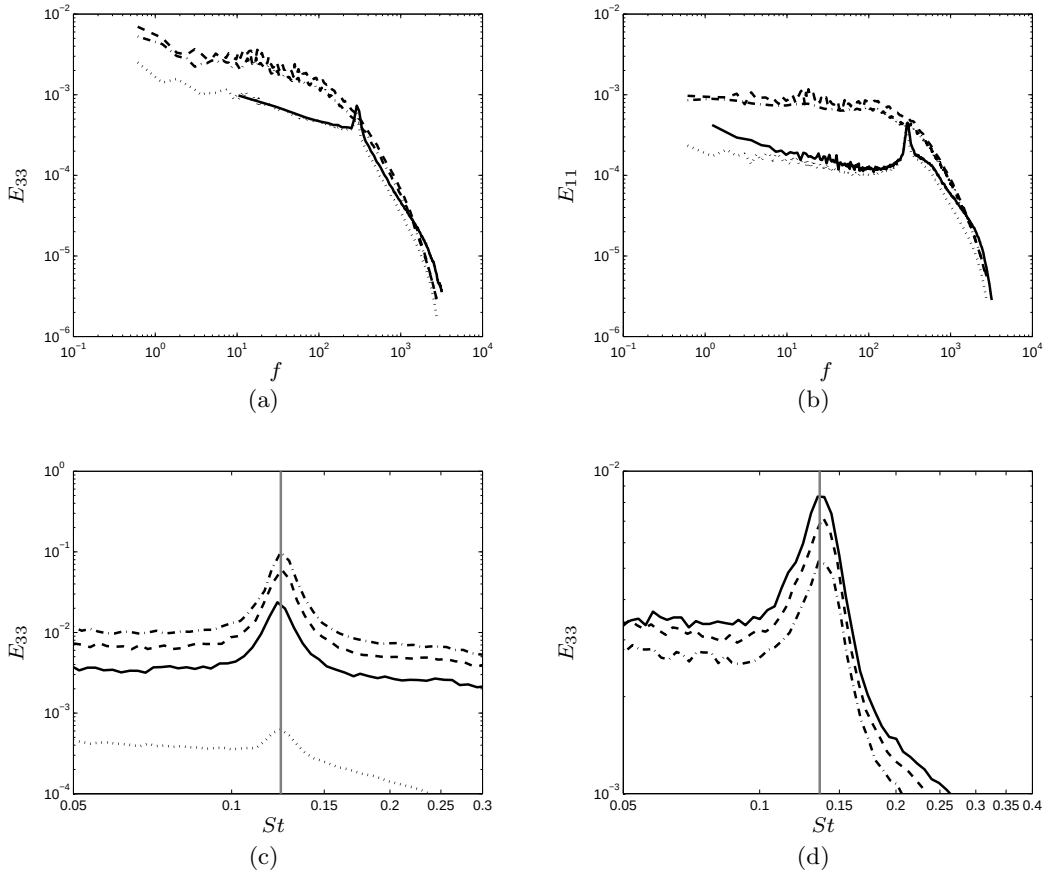


**Figure 4.16:** (a) and (b) are examples of $E_{11}$ and $E_{33}$ vs. $f$, respectively, at $z/D = 65$ for the pure wake and cases one three and five; solid, dashed, dash-dot and dotted lines are spectral measurements for the pure wake and cases one, three and five respectively. (c) and (d) are examples of the independency of dimensionless vortex shedding frequency (grey solid line) with the Reynolds number for cases five and one respectively; in (c) the black solid, dashed and dashed-dot lines are energy spectrum measurements at $z/D \approx 4-5$ at $Re \approx 5400, 7200$ and 8900, respectively, and the black dotted line is energy spectral measurement at $z/D = 65$ at $Re \approx 15000$. In (d) the black solid, dashed and dashed-dot lines are energy spectral measurements at $z/D \approx 4-5$ at $Re \approx 5500, 10100$ and 13500, respectively

as a consequence the sphere's drag is reduced.

Last to be examined was the energy spectrum (measured in the far-wake regime). One of the clear differences that was noticed (when compared to the pure-wake case) was that the vortex shedding frequency was no longer noticeable in the spectrum of the axial and radial velocity when the disc was surrounded by the turbulent streams generated by grid A. Note that in the pure-wake case the vortex shedding frequency was easily noticeable in both the axial and radial energy spectra. Figures 4.16(a) and (b) show examples of the axial and radial spectrum ($E_{33}$ and $E_{11}$ respectively) around the wake half width at $z/D = 65$ for the pure wake and cases one, three and five. Before continuing the discussion about the disappearance of the vortex shedding frequency from the spectrum, the other clear difference between the various cases will be discussed – the rms value of the normal fluctuating velocities is increased

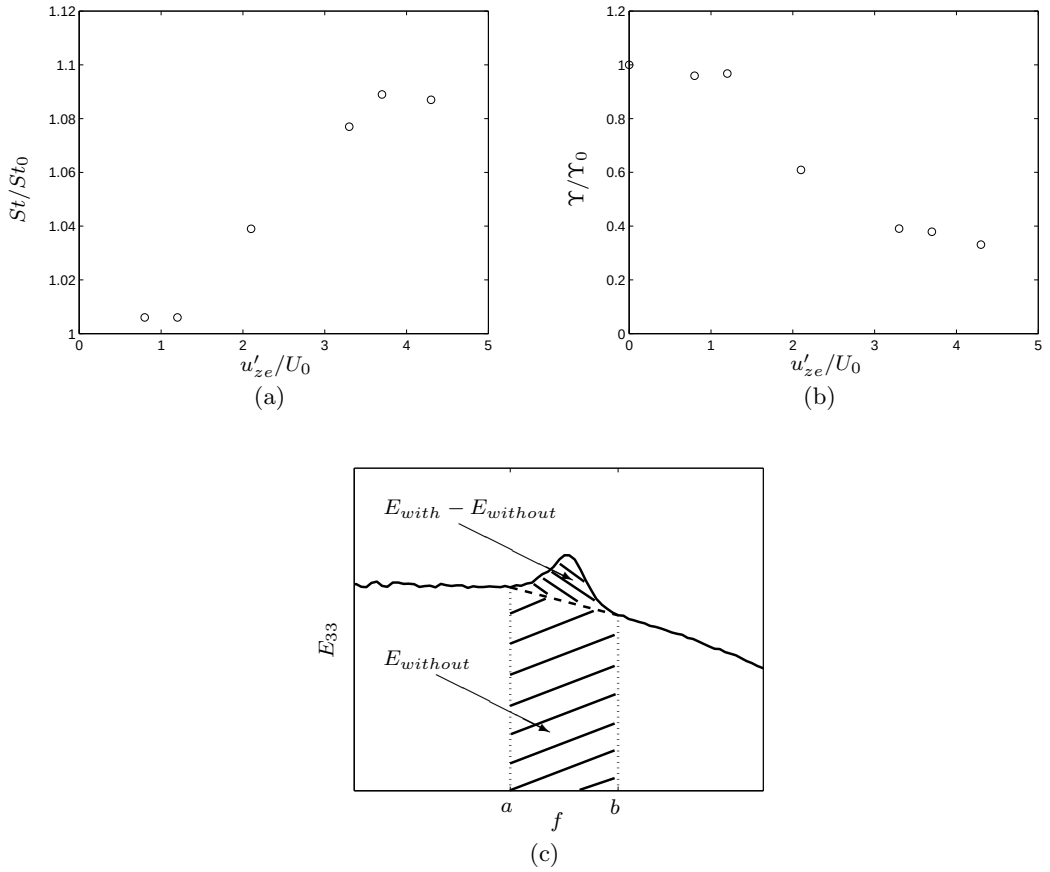


**Figure 4.17:** (a) Variations of the dimensionless vortex shedding frequency with $u'_{ze}/U_0$ compared with the pure wake case, $St_0$. (b) Variations of the relative energy the shedding process contributes to the spectrum with $u'_{ze}/U_0$ compared with the pure wake case, $\Upsilon_0$. (c) is an example clarifying the definitions of $E_{with}$ and $E_{without}$.

by about a factor of three when the disc was surrounded by the turbulence streams created by grid A, in comparison to ones created by grid B, as also illustrated in figures 4.16(a) and (b). Recall that the relationship between the Reynolds stresses and the spectrum is,

$$\overline{u_i u_i} = \int E_{ii} \mathrm{d}f, \tag{4.11}$$

where there is no sum on repeated indices. Thus, since the free-stream turbulence levels at $z/D = 0$ varied about monotonically with the different cases at $z/D = 0$ (see table 4.1), one might think that it is the ratio $L_{11}/D$ at $z/D = 0$ which imposes that great difference. However, since in the far-wake region the ratio $u'_{ze}/u'_{z_{max}}$ is much larger for the cases where the free-stream turbulence was created by grid A compared to grid B (as illustrated in figures 4.9, 4.10 and 4.11) the author believes it is the actual value of the ratio $u'_{ze}/u'_{z_{max}}$ in the far wake region which cause this difference. In other words, it is the free-stream turbulence intensity level in the far-wake region which imposed that great difference.

In order to understand better the disappearance of the vortex shedding signal, near-wake flow field measurements (using PIV) and spectral measurements (at a fixed location, about $4-5D$ downstream of the disc) were made. Before discussing the results, it should be clarified that the near-wake flow field and spectral measurements were made at $Re = 6500$, due to hot-wire mounting limitations at high speeds in the near-wake region and PIV experimental limitations at high speeds. Note also that the dimensionless vortex shedding frequency ($St = fD/U_0$, where $f$ is the dimensional vortex shedding frequency) was found to be Reynolds number independent in the $5000 < Re < 15000$ regime in the pure-wake case and in the turbulent cases four, five and six, as illustrated in figure 4.16(c) for case five. For the other three cases it was only possible to verify the independency of dimensionless vortex shedding frequency in the $5000 < Re < 13500$ range, as illustrated in figure 4.16(d) for case one, since it was only traceable in the near-wake spectral measurements.

Figure 4.17(a) shows that the vortex-shedding frequency only slightly rises when the free-stream's turbulence intensity is increased, as was also noticed by Castro (1995) when studying wakes downstream of a ring. Castro (1995) suggested that the increase in the rate vortices are shed is associated with the reduction in length of the recirculating region (which, as was reported above, becomes shorter with increasing $u'_{ze}/U_0$), and reduces the distance to formation of those vortices. On the other hand, figure 4.17(b) shows that while the addition of turbulence increases the vortex shedding frequency, it weakens the relative energy the shedding process contributes to the spectrum. This strength is defined using $\Upsilon$, where $\Upsilon = (E_{with} - E_{without})/E_{without}$, $E = \int_a^b E_{33}\mathrm{d}f$, $[a, b]$ is the range of frequencies bounding the vortex shedding peak and the subscripts *with* and *without* specify, respectively, whether the peak was included or removed before the integral was calculated. Figure 4.17(c) shows an example clarifying this. Note that the weakening of the vortex-shedding process has also been noticed by several other researchers in the context of several different objects in turbulent streams, e.g. Gerrard (1966) and Tyagi *et al.* (2005). Thus, the fact that the vortex-shedding energy is reduced (already at the creation process) combined with the fact that it is being continuously reduced with distance downstream (as illustrated in figure 4.2) explains why it is harder to trace, or even in some cases is completely untraceable, in the far-wake spectral measurements.

In addition, since in the near wake regime the turbulence levels inside the wake gradually increase with $u'_{ze}/U_0$ (i.e. section 4.2.4) whilst the vortex-shedding strength is reduced due to the increased entrainment in the separated shear layer (see section 4.2.4 and Gerrard, 1966),

the relative contribution to the spectrum would necessarily be reduced. Thus, there would be a point (at high enough $u'_{ze}/U_0$) where the spectral peak would not be easily traceable even in the near-wake regime, as Mujumdar & Douglas (1970) noticed two diameters downstream of a sphere in turbulent streams. Yet, while they suggested that in their experiment the vortex shedding is suppressed, based on auto-correlation measurements, it is suggested here that other techniques should be used in order to be able to identify whether or not the vortex shedding is actually suppressed, since it may just not have sufficient energy to be visible in the spectrum. Nevertheless, in that case, whether the vortex shedding is present or not, its contribution to the wake's turbulence structure would be insignificant.

In summary, the turbulence in the free-stream clearly impacts the far axisymmetric wake structure and development. Moreover, those effects are not only associated with the interaction the wake has with the free-stream turbulence in the far-wake region but also at its creation in the near field. Thus, the initiation of the wake clearly defines some of its specifying properties in the far-wake region.

### 4.2.4 The Near-Wake Flow Field

Even though the main purpose of this research was to examine the effects free-stream turbulence have on the far axisymmetric wake, near-wake flow field measurements were made as well. The original motivation was to understand better the weakening mechanism of the vortex shedding process (as discussed above). However, since it was found (and shown above) that the interaction of the turbulent stream with the wake-generating body defines some of its far wake properties, the differences between the different wakes at their formation region are presented here also.

As was presented above, the recirculation region was reduced in length due to the presence of the turbulence in the free-stream. However, the form of the mean velocity profiles in that region (when compared at different stations of $z/R_l$) remains the same. Figure 4.18 shows the streamlines in the recirculation region deduced from the two extreme cases – the pure wake and the wake in case one. Notice that the minimum value of the stream function, which in cylindrical coordinates is defined by

$$\psi = \int_0^\infty \frac{U}{U_0} r \mathrm{d}r, \tag{4.12}$$

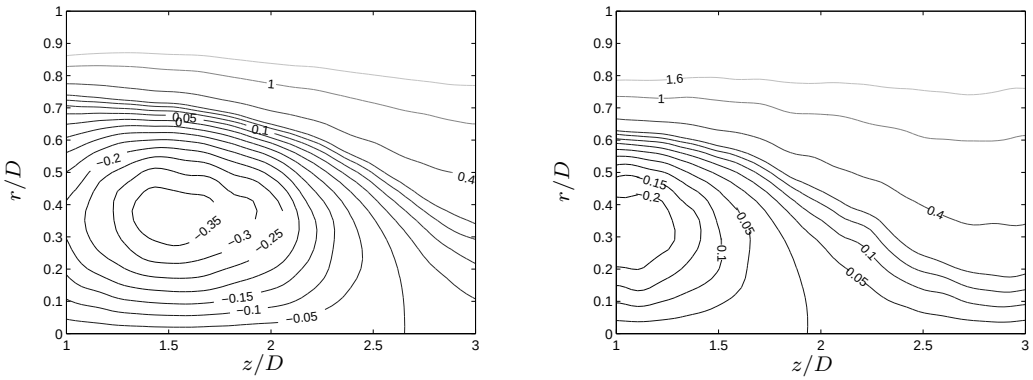


(a) (b)

**Figure 4.18:** Mean streamlines; (a) pure wake (b) case one.

increases, i.e. becomes more positive, when $u'_{ze}/U_0$ is introduced. It should be clarified that in the other turbulent cases the minimum value decreased gradually with $u'_{ze}/U_0$, suggesting that the amount of fluid recirculated is reduced when the intensity level in the free-stream is increased (recall that the definitions of the stream function and the mass flux are similar). Figure 4.19(a) shows the growth of the vorticity thickness, $\Lambda$, defined by:

$$\Lambda = \left[\frac{\partial\left(U/\Delta U\right)}{\partial r}\right]^{-1}_{max}, \tag{4.13}$$

where $\Delta U$ is the total velocity difference across the shear layer. The vorticity thickness is clearly higher when $u'_{ze}/U_0$ is increased. Moreover, its growth rate is slightly increased as well, which is especially noticeable in figure 4.19(a) before the end of the formation region, where $0.7 < R_l < 1$, because of the increased entrainment rate into the separated shear layer from the free-stream. Further evidence of the increase in the entrainment rate from the free-stream to the separated shear layer is noticeable in the mean streamlines (e.g. figure 4.18), where a slight increase in the absolute value of the separated shear layer bounding streamline's gradient is noticeable as well. Note that since the shear layer is entraining more fluid bearing zero vorticity from the free-stream, the forming vortices would have to be weaker, which accounts for the gradual reduction in the peak vorticity levels in the separated shear layer by up to about 30% between the two extreme cases – the pure wake case and case one, and the gradual reduction in length of the formation region (i.e. Gerrard, 1966), which was presented in section 4.2.3, and the reduction in the amount of fluid recirculated.

Similarly to the mean velocity, the form of the various Reynolds stress profiles was not effected by the presence of the turbulence in the free-stream. Examples of the various Reynolds stress profiles of the pure wake and case one at $z/R_l = 1$ are presented in figure 4.19(b). Al-

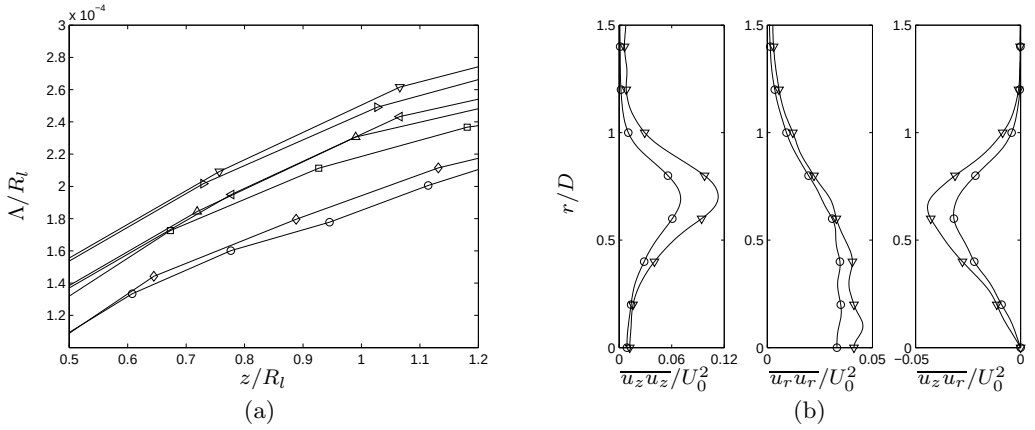


**Figure 4.19:** (a) Growth of the vorticity thickness; (—○—), (—▽—), (—▷—), (—◁—), (—△—), (—□—) and (—◇—) are measurements of the pure wake and cases one, two, three, four, five and six, respectively. (b) Reynolds stress profiles at $z/R_l = 1$; (—○—) and (—▽—) are measurements of the pure wake and case one, respectively.

though their form did not change, their values were increased with an increase $u'_{ze}/U_0$, as can be noticed figure 4.19(b). In addition, it was noticed that the axial development of the various stresses' maximum values is slightly different as well, as illustrated in figure 4.20. The maximum values of $\overline{u_z^2}$ and $|\overline{u_z u_r}|$ were found to increase gradually with $u'_{ze}/U_0$ with their peak values being reached at about the same relative location, $z/R_l = 0.72$ and $z/R_l = 0.8$, respectively. However, the maximum value of $\overline{u_r^2}$ was found to vary with $u'_{ze}/U_0$ in no particular direction while its peak value is gradually reached further downstream from about $z/R_l = 1.1$, in the pure wake, to about $z/R_l = 1.3$, in case one. Hence, these results suggest that the transition to turbulence of the separated shear layer probably occurred earlier. Moreover, since the turbulent shear stress was found to be increased in the separated shear layer while the mean shear is about kept the same, the production of turbulent kinetic energy must increase as well there. (Note that similar findings were also reported on boundary layers in turbulent streams, in section 2.4).

Even though the different turbulent stresses change in value due to the presence of the turbulence in the free-stream, the profile of the efficiency with which the eddies produce turbulent shear stress for a given amount of turbulent kinetic energy was found to be hardly altered, neither in form nor in value, when compared at different $z/R_l$ stations inside the formation region as illustrated in figure 4.21(a). (Note that efficiency is reflected in the structure parameter which is the ratio of the shear stress to the turbulent kinetic energy – $\overline{u_z u_r}/q^2$ (see Townsend (1976)), where $0.5q^2$ is the turbulent kinetic energy per unit mass, which was estimated, since a two-dimensional PIV system was used, by $(3/4)\left(u_z^2 + u_r^2\right)$). In addition, the profile of the isotropy measure, $\overline{u_r^2}/\overline{u_z^2}$, was found to be barely modified,

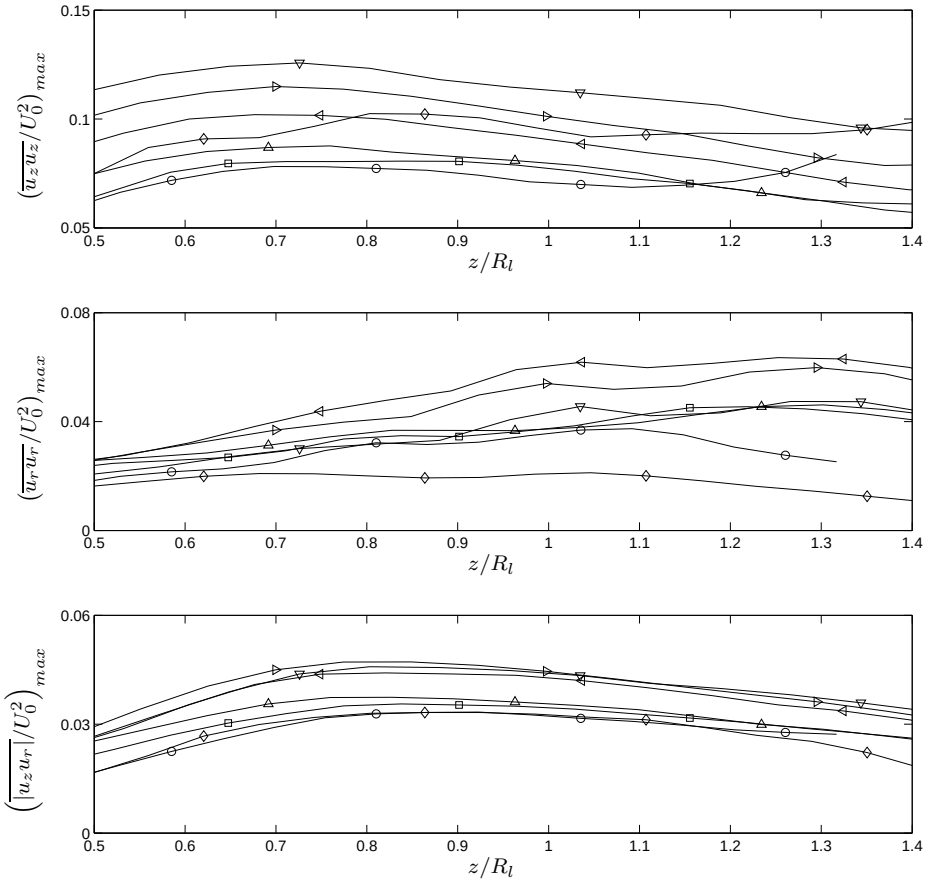


**Figure 4.20:** Axial development of the maximum Reynolds stresses; (—○—), (—▽—), (—▷—), (—◁—), (—△—), (—□—) and (—◇—) are measurements of the pure wake and cases one, two, three, four, five and six, respectively. Note that the maximum values of the Reynolds stresses in case six, which are presented in the figure, show inconsistency in compare to the other experiments which is associated to a measurement error of the turbulent stresses in that specific experiment.

especially inside the separated shear layer, either in form or in value, by the presence of the turbulence in the free-stream, when compared at different $z/R_l$ stations inside the formation region, as illustrated in figure 4.21(b). Note that even though Castro & Haque (1988) have shown the opposite – that the form of those two structure functions in a two-dimensional reversed flow region changes due to the presence of the turbulence in the free-stream – the author believes that the presence of a splitter in their measurements (which they used in order to prevent the vortex shedding and thus achieve a longer recirculation region) is the reason for the difference between the two findings. The presence of the splitter affects the structure of the eddies close to it. Note that support for this statement is clearly evident in Castro & Haque's (1988) turbulence structure function profiles (presented in figure 13 in their paper), where it is evident that the largest (and so the source) of deviation from their

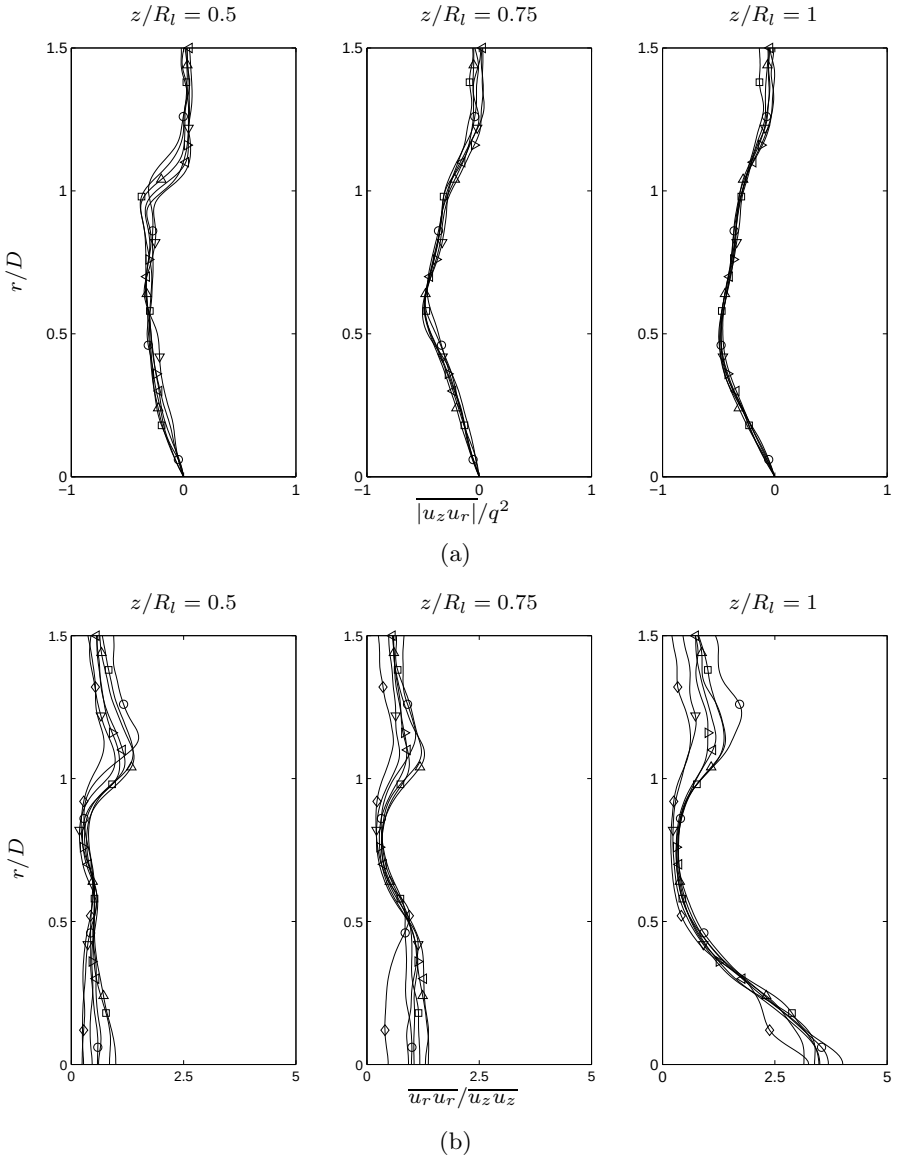


**Figure 4.21:** Development of the turbulence structure functions – $\overline{u_z u_v}/q^2$, (a), and $\overline{u_v u_v}/\overline{u_z u_z}$, (b); (—○—), (—▽—), (—▷—), (—◁—), (—△—), (—□—) and (—◇—) are measurements of the pure wake and cases one, two, three, four, five and six, respectively. Note that the turbulence structure measurements in case six, which are presented in the figure, show inconsistency in compare to the other experiments which is associated to a measurement error of the turbulent stresses in that specific experiment.

form in uniform free-stream is located in the near splitter/wall regime.

In summary, the turbulent streams clearly impact the values of the various mean and turbulence parameters inside the vortex formation region. However, while those change in value they do not change in form. Last, once more the importance of the role of initial conditions on the far wake regime is demonstrated.

Chapter 5

# Final Discussion

In chapters 3 and 4 the computational and experimental approaches that were used to explore the effects free-stream turbulence have on an axisymmetric wake were discussed separately. Before concluding this study it is important to examine the fundamental difference between the two approaches and to discuss some of the differences and similarities in the findings.

In the experimental part, the wake was introduced to the free-stream turbulence already in its creation stage. On the other hand, in the computational part, in order to make the simulation feasible using DNS, the wake generating body was never modelled and the wake was artificially combined with the external turbulence only after it was created in quiescent surroundings. Thus, if one would have wanted to conduct an experiment which is similar to the simulation one would have had to make sure the free-stream is only turbulent away from the generating body such that the wake would be created inside a uniform stream. That way, the wake would only reach, after developing for some downstream distance, the turbulent part of the free-stream and only then it would start to be affected by it. That fundamental difference would be mainly noticeable when the drag coefficient would be examined. In the current wind-tunnel experiments the disc's drag coefficient was increased by the presence of the free-stream turbulence as a direct result of the impact of the free-stream turbulence on the near-wake region, while in an experiment similar to the simulation the disc's drag coefficient would not be affected since the flow surrounding the disc would always be (quiescent, and so) similar. In addition, other differences would be noticeable in the near wake region as well. For example the vortex shedding frequency and strength and the entire near wake flow field would not be affected either, for the same reason. Thus, it is clear the near-wake flow field has a great role in shaping the far-wake region and that the difference between the two experiments is critical.

Nevertheless, despite that significant effect of the wake's initial conditions, in both the

DNS and in the wind-tunnel experiments, the impact of the free-stream turbulence intensity levels were obvious in both cases and in many cases similar. For example, both in the wind tunnel experiments and in the DNS the external turbulence gradually penetrated and took over the turbulence structure inside the wake. Moreover, both in the wind tunnel experiments and in the DNS the rate of that penetration process was found to be higher as the turbulence levels in the free-stream were increased. Note however that while in the DNS the leading parameter was the ratio $u'_{ze}/U_d$ at the moment the wake and the external turbulence were combined, in the wind tunnel the initial leading parameter was ratio $u'_{ze}/U_0$ at $z/D = 0$, introducing the free-stream turbulence on the near wake region (and nevertheless affecting some of the far wake features like the wake strength, and the vortex shedding strength and frequency) but further downstream $u'_{ze}/u'_{z_{max}}$ becomes more important and defined how much the external turbulence influenced the far-wake region, as can be noticed when figures 4.9, 4.10 and 4.11 (pages 73, 74 and 75, respectively) are compared. It is obvious there that when $u'_{ze}/u'_{z_{max}} \ll 1$ the level at which the free-stream turbulence penetrates the wake in the far-wake region is much smaller than when $u'_{ze}/u'_{z_{max}} > 0.5$, even though the mean wake is much larger and stronger there (due to the increased drag). Recall that Wu & Feath (1995) had noticed in their measurements that when $u'_{ze}/u'_{z_{cl}} \approx 1$, where $u'_{cl}$ is the rms value of the axial fluctuating velocity at the wake centreline, the mean wake decay rate increased significantly for their low-Reynolds-number wake downstream of a sphere in turbulent streams. Unfortunately, that point was never reached in the wind-tunnel experiments. However, that point was reached and crossed in the DNS, where the decay rate of the wake was noticed to be increasing significantly.

In addition, the process, by which the external turbulence penetrates into the wake in the far-wake region and gradually takes over the turbulence structure there was found to be the main reason for ending the wake's self-similarity state in the DNS – the turbulence in the free-stream was moving inwards changing the values of the turbulent stresses inside the wake until the point where they were identical to the ones in the free-stream (except the turbulent shear stress), as illustrated in figure 3.16 (in page 54). Also, in the DNS the free-stream turbulence completely took over the turbulence structure inside the wake, as illustrated for case three in figure 3.19(b) (in page 58). Then, since the external turbulence decayed slower than the wake, the commonly used definition of self-similarity (where all the velocity parameters scale the same) broke down and ceased to exist. On the other hand, in the wind-tunnel experiments, although a similar process was clearly evident, the point where the turbulence inside the wake is similar to the turbulence in the free-stream was never fully

reached. Nevertheless, the fact that the profiles of the normal turbulence stresses evolved towards uniformity suggests that a similar take over was in process, and that the point at which it would have finished was located further downstream (at $z/D > 115$). It should be mentioned here that different approaches were tried in order to take measurements beyond that point but they all failed, mainly due to the limited size of the wind-tunnel cross section. (Further downstream measurements were not perused mainly due to the ratio between the wake and test section widths. Also, a different approach that was tried in order to witness the end of the take over was to increase the turbulence levels already upstream using a different grid and thus to move the take over point upstream. Unfortunately that method was found to be not suitable either since the wake that was created was too big for the wind tunnel even by $z/D = 65$ as a direct result of the increase in the disc's drag coefficient).

While the importance of the free-stream turbulence intensity in shaping the near- and far-wake turbulence and mean structures were clearly captured by both techniques, the impact of the ratio between the external turbulence integral scale and the wake width, in the far wake region for example, was unfortunately never fully captured, as presented in table 3.1 and figure 4.13(e) (pages 49 and 78, respectively). In the DNS this ratio was more or less the same $(0.6 - 0.7)$, while in the wind-tunnel experiments two groups of ratios were available in the near-wake region $(3 - 4)$ and $(11 - 14)$ and only one in the far-wake region $(0.85 - 1)$. However, since the intensity levels were different between all the wind tunnel experiments it is hard to fully determine in what way that ratio influences the mean and turbulence structure of the wake in the far-wake region. Nevertheless, in the near-wake region it does seem that the integral scale did not influence the recirculation region by much, since the recirculation length varied quite linearly with $u'_{ze}/U_0$ without any noticeable impact of the free-stream turbulence integral length scale, even though the integral scale was about four times larger (at $z/D = 0$) in cases one two and three compared to cases four, five and six. Note that this is quite a surprise since Hancock (1980), Hancock & Bradshaw (1989) and Castro (1995) reported that the integral length scale does influence the level of impact free-stream turbulence has on shear layers, where integral length scale of the same order of the boundary-layer thickness was suggested to lead to the strongest impact.

In summary, even though the wind tunnel experiments and the DNS modelled two different scenarios, both sets of results lead to the same conclusion that a far-wake in turbulent surroundings is not self-similar due to the take over of the turbulence structure inside the wake by the one in the free-stream.

Chapter 6

# Conclusions

Wind-tunnel and numerical experiments were undertaken in order to study the influence free-stream turbulence has on axisymmetric wakes. As expected, it was found that the free-stream turbulence affects the wake's mean and turbulent structure and their development. It was also found that the level at which the free-stream turbulence affects the wake is related to the ratio between the turbulence levels inside and outside the wake. However, no empirical relationship was derived since it is believed that there are more parameters which might have influenced the wake's mean and turbulence structure as well, like the length scales. In addition, for the first time it has been shown that the classical self-similar solution is no longer valid under those conditions, due to the gradual take over of the turbulence structure inside the wake (which starts at the wake's edge and moves inwards towards its centre) by the one in the free-stream. While in the DNS the mean wake always decayed faster than the external turbulence does, in the wind-tunnel experiments the mean wake decayed in some cases at the same rate the free-stream turbulence does, which suggests that far enough downstream self-similarity might be expected (where the turbulence levels inside and outside the far wake would be similar) since then the mean velocity and turbulence all across the wake would be decaying at the same rate. Finally, the importance of the boundary/initial conditions in shaping the far wake region were clearly emphasised by the different findings revealed by the two approaches.

## 6.1 Future Work Proposal

Even though the work that has been done answers some very important questions about the free-stream turbulence impact on the far axisymmetric wake self-similarity, it opens the door to many more questions: what happens beyond the point where $u'_{ze} = u_{z_{max}}$, how

do the length scales in the free-stream turbulence influence that whole process and now that it is known that the free-stream turbulence is penetrating the wake and taking over its structure, it would also be interesting to know at what rate it does this and what is influencing this rate. Each of those questions would require a different type of experiments to be conducted. For example, in order to reach beyond the point where $u'_{ze} = u_{z_{max}}$ a much larger wind tunnel would be required in order to avoid blockage effects. Or for the length-scales impact, experiments with a much larger variety of length scale variations in the free-stream would be needed. And last, in order to determine the rate at which the free-stream turbulence penetrates the wake and takes over its structure, two-point correlation maps could be measured at different downstream positions and compared.

While the questions above are very fundamental one might want to look at some of this study's applications. For example, one might want to look at the effect free-stream turbulence has on porous discs which are a very simplified version of a wind turbine, or even take it further and examine what is the influence of one porous disc's wake on another. Another interesting question is whether the free-stream turbulence reduces the aero-acoustic sound generated by the disc, which could be useful for detecting or avoiding detection of submarines.

Appendix A

# Relationship Between the Mean Velocity and the Turbulent Shear Stress Profiles

Since the product $U_d \times l_h^2$ is constant the following can be written:

$$\begin{aligned} 0 &= \frac{\mathrm{d}\left(l_h^2\, U_d\right)}{\mathrm{d}z} \\ &= 2 l_h U_d \frac{\mathrm{d}l_h}{\mathrm{d}z} + l_h^2 \frac{\mathrm{d}U_d}{\mathrm{d}z}. \end{aligned} \tag{A.1}$$

Equation A.1 leads to the following relationship

$$\frac{\mathrm{d}U_d}{\mathrm{d}z} = -\frac{2\, U_d}{l_h} \frac{\mathrm{d}l_h}{\mathrm{d}z}. \tag{A.2}$$

Using this relationship, Equation 2.25 is simplified in the following way:

$$\begin{aligned} \frac{1}{\xi}\, g + g' &= \frac{U_0}{U_d} \frac{\mathrm{d}l_h}{\mathrm{d}z}\, f + \frac{U_0}{U_d} \frac{\mathrm{d}l_h}{\mathrm{d}z}\, \xi\, f', \\ \frac{1}{\xi}\, g + g' &= \frac{U_0}{U_d} \frac{\mathrm{d}l_h}{\mathrm{d}z} \left(\xi\, f' + 2 f\right), \\ (\xi\, g)' &= \frac{U_0}{U_d} \frac{\mathrm{d}l_h}{\mathrm{d}z} \left(\xi^2\, f\right)', \\ g &= \frac{U_0}{U_d} \frac{\mathrm{d}l_h}{\mathrm{d}z}\, \xi\, f. \end{aligned} \tag{A.3}$$

Given the self-similar mean velocity profile and its parameters ($f(\eta), U_d$ and $l_h$) the shear stress ($g(\eta)$) can thus be computed.

Appendix B

# Convection Term in Equation 4.9

The aim here is to prove that

$$\frac{l_h}{U_d^3}U_0\frac{\mathrm{d}K}{\mathrm{d}z} = -\frac{1}{3}\frac{r}{l_h}\frac{\mathrm{d}\left(K/U_d^2\right)}{\mathrm{d}\left(r/l_h\right)} - \frac{4}{3}\frac{K}{U_d}, \tag{B.1}$$

where $K = \frac{1}{2}\left(\overline{u^2} + \overline{v^2} + \overline{w^2}\right)$ and the wake is self-preserving with $l_h \sim z^{1/3}$ and $U_d \sim z^{-2/3}$.

Since $l_h = l_h(z)$ the following can be written

$$\frac{\mathrm{d}}{\mathrm{d}\left(r/l_h\right)} = \frac{\frac{\mathrm{d}}{\mathrm{d}z}}{\frac{\mathrm{d}(r/l_h)}{\mathrm{d}z}}, \tag{B.2}$$

so that

$$\frac{\mathrm{d}}{\mathrm{d}z} = \frac{\mathrm{d}}{\mathrm{d}\left(r/l_h\right)}\frac{\mathrm{d}\left(r/l_h\right)}{\mathrm{d}z}. \tag{B.3}$$

But

$$\frac{\mathrm{d}\left(r/l_h\right)}{\mathrm{d}z} = -\frac{r}{l_h^2}\frac{\mathrm{d}l_h}{\mathrm{d}z} = -\frac{r}{l_h^2}\frac{1}{3}D^{2/3}z^{-2/3} = -\frac{1}{3}rD^{-2/3}z^{-4/3}. \tag{B.4}$$

Hence

$$\frac{\mathrm{d}}{\mathrm{d}z} = -\frac{1}{3}rD^{-2/3}z^{-4/3}\frac{\mathrm{d}}{\mathrm{d}\left(r/l_h\right)}. \tag{B.5}$$

Thus $\frac{\mathrm{d}K}{\mathrm{d}z}$ can be written in terms of $\frac{\mathrm{d}\left(K/U_d^2\right)}{\mathrm{d}(r/l_h)}$.

Using Equation B.5 and that

$$\frac{\mathrm{d}}{\mathrm{d}z}\left(\frac{K}{U_d^2}\right) = \frac{1}{U_d^2}\frac{\mathrm{d}K}{\mathrm{d}z} - \frac{2K}{U_d^3}\frac{dU_d}{dz} \tag{B.6}$$

so that

$$\frac{\mathrm{d}K}{\mathrm{d}z} = U_d^2\frac{\mathrm{d}}{\mathrm{d}z}\left(\frac{K}{U_d^2}\right) + \frac{2K}{U_d}\frac{dU_d}{dz} \tag{B.7}$$

the following can be written

$$\begin{aligned}\frac{l_h}{U_d^3}U_0\frac{\mathrm{d}K}{\mathrm{d}z} &= \frac{l_h}{U_d}U_0\frac{\mathrm{d}}{\mathrm{d}z}\left(\frac{K}{U_d^2}\right) + \frac{2KU_0l_h}{U_d^4}\frac{dU_d}{dz} \\ &= -\frac{l_hU_0}{U_d}\frac{1}{3}rD^{-2/3}z^{-4/3}\frac{\mathrm{d}\left(K/U_d^2\right)}{\mathrm{d}\left(r/l_h\right)} - \frac{2KU_0l_h}{U_c^4}\frac{2}{3}U_0D^{2/3}z^{-5/3} \\ &= -\frac{1}{3}\frac{r}{l_h}\frac{\mathrm{d}\left(K/U_d^2\right)}{\mathrm{d}\left(r/l_h\right)} - \frac{4}{3}\frac{K}{U_d^2}\end{aligned} \tag{B.8}$$

which was to be proven.

# References


Bagchi, P. & Balachander, S. 2004 Response of the wake of an isolated particle to an isotropic turbulence flow. *J. Fluid Mech.* **518**, 95–123.

Bandyopadhyay, P. R. 1992 Reynolds number dependence of the freestream turbulence effect on turbulent boundary layers. *AIAA Journal* **30** (7), 1910–1912.

Basu, A. J., Narasimha, R. & Sinha, U. N. 1992 Direct numerical simulation of the initial evolution of a turbulent axisymmetric wake. *Current Science* **63** (12), 734–740.

Batchelor, G. K. 1953 *The Theory of Homogeneous Turbulence*. Cambridge University Press.

Batchelor, G. K. 1967 *An Introduction to Fluid Dynamics*. Cambridge University Press.

Batchelor, G. K. & Stewart, R. W. 1950 Anisotropy of the spectrum of turbulence at small wave numbers. *Quart. J. of Mech. and Appl. Math.* **3**.

Batchelor, G. K. & Townsend, A. A. 1948*a* Decay of isotropic turbulence in the initial period. *Proceedings of the Royal Society of London. Series A, Mathematical and Physical Sciences* **193**, 539–558.

Batchelor, G. K. & Townsend, A. A. 1948*b* Decay of turbulence in the final period. *Proceedings of the Royal Society of London, Series A, Mathematical and Physical Sciences* **194** (1039), 527–543.

Bearman, P. W. 1965 Investigation of the flow behind a two-dimentional model with a blunt trailing edge and fitted with splitter plates. *J. Fluid Mech.* **21**, 241–255.

Bearman, P. W. & Trueman, D. M. 1972 An investigation of the flow around rectangular cylinders. *Aeronautical Quarterly* **23**, 229–237.

Bennett, J. C. & Corrsin, S. 1978 Small Reynolds number nearly isotropic turbulence in a straight duct and a contraction. *Phys. Fluids* **21** (12), 2129–2140.

Bevilaqua, P. M. & Lykoudis, P. S. 1978 Turbulence memory in self preserving wakes. *J. Fluid Mech.* **89**, 589–606.

Birch, S. F. 1996 The axisymmetric turbulent wake. $34^{th}$ *Aerospace Sciences Meeting and Exhibit, Reno NV* pp. 15–18.

Cannon, S. C. 1991 Large scale structures and the spatial evolution of wakes behind axisymmetric bluff bodies. PhD thesis, University of Arizona, USA.

Canuto, C. G., Hussaini, M. Y., Quarteroni, A. & Zang, T. A. 1988 *Spectral Methods in Fluid Dynamics*. Springer-Verlag.

Carmody, T. 1964 Establishment of the wake behind a disc. *J. of Basic Engineering* **86**, 869–882.

Castro, I. P. 1984 Effect of free stream turbulence on low Reynolds number boundary layers. *J. of Fluids Engineering* **106**, 298–306.

Castro, I. P. 1989 *An Introduction to the Digital Analysis of Stationary Signals: A Computer Illustrated Text*. IOP Publishing Ltd.

Castro, I. P. 1995 Vortex shedding from a ring in turbulent flow. *European Journal of Mechanics. B, Fluids* **14** (3), 245–262.

Castro, I. P. & Haque, A. 1988 The structure of a shear layer bounding a separation regin. Part 2. Effects of free-stream turbulence. *J. Fluid Mech.* **192**, 577–595.

Charnay, G., Comte-Bellot, G. & Mathieu, J. 1971 Development of a turbulent boundary layer of a flat plate in an external turbulent flow. *AGARD* **CP 93** (27).

Charnay, G., Mathieu, J. & Comte-Bellot, G. 1976 Response of a turbulence bounday layer to random fluctuations in the external stream. *Phys. Fluids* **19** (9), 1261–1272.

Chevray, R. 1968 The turbulent wake of a body or revolution. *J. of Basic Engineering* pp. 275–284.

Coles, D. 1956 The law of the wake in the turbulent boundary layer. *J. Fluid Mech.* **1**, 191–226.

Comte-Bellot, G. & Corrsin, S. 1966 The use of a contraction to improve the isotropy of grid generated turbulence. *J. Fluid Mech.* **25**, 657–682.

Corrsin, S. 1963 Turbulence: Experimental methods. *Encyclopaedia of Physics* **8**, 568–590.

Evans, R. L. 1985 Freestream turbulence effects on turbulent boundary layers in an adverse pressure gradient. *AIAA Journal* **23** (11), 1814–1816.

George, W. K. 1992 The decay of homogeneous isotropic turbulence. *Phys. Fluids* **4** (7), 1492–1509.

Gerrard, J. H. 1966 The mechanics of the formation region of vortices behind bluff bodies. *J. Fluid Mech.* **25**, 401–413.

Gibson, C. H., Chen, C. C. & Lin, S. C. 1968 Measurments of turbulent velocity and temperature fluctuations in the wake of a sphere. *AIAA* **6** (4), 642–649.

Gourlay, M. J., Arendt, S. C., Fritts, D. C. & Werne, J. 2001 Numerical modeling of initially turbulent wakes with net momentum. *Phys. Fluids* **13** (12), 3783–3802.

Grant, H. L. & Nisbet, I. C. T. 1957 The inhomogeneity of grid turbulence. *J. Fluid Mech.* **2**, 263–272.

Hancock, P. E. 1980 The effect of freestream turbulence on turbulent boundary layers. PhD thesis, Imperial College of Science and Technology, London University, UK.

Hancock, P. E. & Bradshaw, P. 1989 Turbulence structure of a boundary layer beneath a turbulent free stream. *J. Fluid Mech.* **205**, 45–76.

Huang, M.-J. & Leonard, A. 1994 Power law decay of homogeneous turbulence at low Reynolds numbers. *Phys. Fluids* **6** (11), 3765–3775.

Huffman, G. D., Zimmerman, D. R. & Bennett, W. A. 1972 The effect of free-stream turbulence level on turbulent boundary layer behavior. *AGARD DOGRAPH* **164** (I-5), 89–117.

Hwang, N. H. C. & Baldwin, L. V. 1966 Decay of turbulence in axisymmetric wakes. *J. of Basic Engineering* **88**, 261–268.

Ishida, T., Davidson, P. A. & Kaneda, Y. 2006 On the decay of isotropic turbulence. *J. Fluid Mech.* **564**, 455–474.

Jimenez, J., Wray, A. A., Saffman, P. G. & Rogallo, R. S. 1993 The structure of intense vorticity in isotropic turbulence. *J. Fluid Mech.* **255**, 65–90.

Johansson, P. B. V. & George, W. K. 2006*a* The far downstream evolution of the high Reynolds number axisymmetric wake behind a disc. Part 1. Single point statistics. *J. Fluid Mech.* **555**, 363–385.

Johansson, P. B. V. & George, W. K. 2006*b* The far downstream evolution of the high Reynolds number axisymmetric wake behind a disc. Part 2. Slice proper orthogonal decomposition. *J. Fluid Mech.* **555**, 387–408.

Johansson, P. B. V., George, W. K. & Gourlay, M. J. 2003 Equalibrium similarity, effects of initial conditions and local Reynolds number on the axisymmetric wake. *Phys. Fluids* **15** (3), 603–617.

Johansson, P. B. V., George, W. K. & Woodward, S. H. 2002 Proper orthogonal decomposition of an axisymmetric turbulence wake behind a disc. *Phys. Fluids* **14** (7), 2508–2514.

Karman, T. & Howarth, L. 1938 On the statistical theory of isotropic turbulence. *Proceedings of the Royal Society of London. Series A, Mathematical and Phsical Sciences* **164** (917), 192–215.

Keneda, Y., Ishihara, T., Yokokawa, M., Itakura, K. & Uno, A. 2003 Energy dissipation rate and energy spectrum in high resolution direct numerical simulations of turbulence in a periodic box. *Phys. Fluids* **15** (2), L21–L24.

Kim, J., Moin, P. & Moser, R. 1987 Turbulence statistics in fully developed channel flow at low Reynolds number. *J. Fluid Mech.* **177**, 133–166.

Kline, S. J., Lisin, A. V. & Waitman, B. A. 1960 Preliminary experimental investigation of effect of free-stream turbulence on turbulent boundary-layer growth. *NASA Technical Note* **D-368** (N89-71189).

Kolmogorov, A. N. 1941c On degeneration of isotropic turbulence in an incompresible fluid. *Doklady Akademii Nauk SSSR* **31**, 538–540.

KREYSZIG, E. 1988 *Advanced Engineering Mathematics*, sixth edn. John Wiley and Sons Inc.

KROGSTAD, P.-A. & DAVIDSON, P. A. 2010 Is grid turbulence Saffman turbulence? *J. Fluid Mech.* **642**, 373–394.

LAVOIE, P., DJENIDI, L. & ANTONIA, R. A. 2007 Effects of initial conditions in decaying turbulence generated by passive grids. *J. Fluid Mech* **585**, 395–420.

LEGENDRE, D., MERLE, A. & MAGNAUDET, J. 2006 Wake of a spherical bubble or a solid sphere set fixed in a turbulent environment. *Phys. Fluids* **18** (048102), 1–4.

MAXEY, M. R. 1987 The velocity skewness measured in grid turbulence. *Phys. Fluids* **30** (4), 935–938.

MCDONALD, H. & KRESKOVSKY, J. P. 1974 Effect of free stream turbulence on the turbulent boundary layer. *Int. J. Heat Mass Transfer* **17**, 705–716.

MITTAL, R. 2000 Response of the sphere wake to freestream fluctuations. *Theoretical and Computational Fluid Dynamics* **13**, 397–419.

MOHAMED, M. S. & LARUE, J. C. 1990 The decay power law in grid generated turbulence. *J. Fluid Mech.* **219**, 195–214.

MUJUMDAR, A. S. & DOUGLAS, W. J. W. 1970 Eddy shedding from a sphere in turbulent free-streams. *Int. J. Heat Mass Transfer* **13**, 1627–1629.

ORSZAG, S. A. 1980 Spectral methods for problems in complex geometries. *J. of Computational Physics* **37**, 70–92.

OSTOWARI, C. & PAGE, R. H. 1989 Velocity defect of axisymmetric wakes. *Experiments in Fluids* **7**, 284–285.

PAL, S. 1981 Wake boundary layer interaction in turbomachinery. PhD thesis, City University of New York, USA.

POPE, S. B. 2000 *Turbulent Flows*. Cambridge University Press.

PORTFORS, E. A. & KEFFER, J. F. 1969 Isotropy in initial period grid turbulence. *Phys. Fluids* **12** (7), 1519–1521.

Raithby, G. D. & Echert, E. R. G. 1968 The effect of turbulence parameters and support position on the heat transfer from sphers. *Int. J. Heat Mass Transfer* **11**, 1133–1252.

Redford, J.A., Castro, I.P. & Coleman, G.N. in preparation On the non-universality of turbulent axisymmetric wakes.

Redford, J. A. & Coleman, G. N. 2007 Numerical study of turbulent wakes in background turbulence. *Fifth international Symposium on Turbulence and Shear Flow Phenomena (TSFP-5 Conference), Munich Germany* pp. 561–566.

Riddhagni, P. R., Bevilaqua, P. M. & Lykoudis, P. S. 1971 Measurments in the turbulent wake of a sphere. *AIAA* **9** (7), 1433–1434.

Rogallo, R. S. 1981 Numerical experiments in homogeneous turbulence. *NASA Technical Memorandum 81315* .

Saffman, P. J. 1967 The large-scale structure of homogeneous turbulence. *J. Fluid Mech.* **27**, 581–593.

Simonsen, A. J. & Krogstad, P.-. 2005 Turbulent stress invariant analysis: Clarification of existing terminology. *Phys. Fluids* **17** (088103).

Spalart, P. R., Moser, R. D. & Rogers, M. M. 1991 Spectral methods for the Navier-Stokes equations with one infinite and two periodic directions. *Journal of Computational Physics* **92**, 297–324.

Stewart, R. W. & Townsend, A. A. 1951 Similarity and self preservation in isotropic turbulence. *Phil. Trans. Roy. Soc.* **243**, 359–386.

Sullivan, N. P., Mahalingam, S. & Kerr, R. 1994 Deterministic forcing of homogeneous isotropic turbulence. *Phys. Fluids* **6**, 1612–1614.

Taylor, G. I. 1935 Statistical theory of turbulence parts i-iv. *Proceedings of the Royal Society of London. Series A, Mathematical and Physical Sciences* **151** (873), 421–478.

Tennekes, H. & Lumley, J. L. 1972 *A First Course in Turbulence*. The MIT Press.

Thole, K. A. & Bogard, D. G. 1996 High freestream turbulence effects on turbulent boundary layers. *Transactions of the ASME* **118**, 276–284.

Townsend, A. A. 1970 Entrainment and the structure of turbulent flow. *J. Fluid Mech.* **41**, 13–46.

Townsend, A. A. 1976 *Structure of Turbulent Shear Flow*. Cambridge University Press.

Tsuji, Y. & Iida, S. 1972 Influences of free stream turbulence on mean velocity of turbulent boundary layer without pressure gradient. *Transactions - Japan Society for Aeronautical and Space Sciences* **15** (29), 105–116.

Tutkun, M., Johansson, P. B. V. & George, W. K. 2008 Three-component vectorial proper orthogonal decomposition of axisymmetric wake behind a disc. *AIAA Journal* **46** (5), 1118–1134.

Tyagi, H. 2005 The effects of near-isotropic turbulence on the wake of a sphere. Master's thesis, University of Windsor, Canada.

Tyagi, H., Liu, R., Ting, D. S.-K. & Johnston, C. R. 2005 Experimental study of vortex shedding from a solid sphere in turbulent freestream. *Proceedings of 2005 ASME Fluids Engineering Division Summer Meeting, FEDSM2005* **V2005**, 561–569.

Tyagi, H., Liu, R., Ting, D. S.-K. & Johnston, C. R. 2006 Measurement of wake properties of a sphere in freestream turbulence. *Experimental Thermal and Fluid Science* **30**, 587–604.

Uberoi, M. S. 1963 Energy transfer in isotropic turbulence. *Phys. Fluids* **6** (8), 1048–1056.

Uberoi, M. S. & Freymuth, P. 1970 Turbulent energy balance and spectra of the axisymmetric wake. *Phys. Fluids* **13** (9), 2205–2210.

Uberoi, M. S. & Wallis, S. 1967 Effect of grid geometry on turbulence decay. *Phys. Fluids* **10** (6), 1216–1224.

Uberoi, M. S. & Wallis, S. 1969 Spectra of grid turbulence. *Phys. Fluids* **12** (12), 1355–1358.

Ustinov, M. V. 2006 Numerical modeling of laminar-turbulent transition in a boundary layer at a high freestream turbulence level. *Fluid Dynamics* **41**, 77–93.

Wang, L.-P., Chen, S., Brasseur, J. G. & Wyngaard, J. C. 1996 Examination of hypotheses in the kolmogorov refined turbulence theory through high-resolution simulations. Part 1. Velocity field. *J. Fluid Mech.* **309**, 113–156.

Wu, J.-S. & Faeth, G. M. 1994 Sphere wakes at moderate Reynolds numbers in a turbulent environment. *AIAA* **32** (3), 535–541.

Wu, J.-S. & Feath, G. M. 1995 Effect of ambient turbulence intensity on sphere wakes at intermediate Reynolds numbers. *AIAA Journal* **33** (1), 171–173.

Xie, Z.-T. & Castro, I. P. 2008 Efficient generation of inflow conditions for large eddy simulation of street-scale flows. *Flow, Turbulence and Combustion* **81** (3), 449–470.

Yeung, P. K. & Brasseur, J. G. 1991 The response of isotropic turbulence to isotropic and anisotropic forcing at the large scales. *Phys. Fluids A* **3** (5), 884–897.